Ambient Backscatter Communication Systems: Design, Signal Detection and Bit Error Rate Analysis

by

Jaya Kartheek Devineni

Dissertation submitted to the Faculty of the
Virginia Polytechnic Institute and State University
in partial fulfillment of the requirements for the degree of

Doctor of Philosophy
in
Electrical Engineering

Harpreet S. Dhillon, Chair
R. Michael Buehrer
Jeffrey H. Reed
Yaling Yang
Lei Zou

August 09, 2021
Blacksburg, Virginia

Keywords: Ambient backscatter, Bit error rate, Hypothesis testing, Coherent and non-coherent detection, Auto-regressive model, Time-selective fading, Vehicular networks, Internet of Things, Manchester encoding, Stochastic geometry, Poisson point process (PPP).

Ambient Backscatter Communication Systems: Design, Signal Detection and Bit Error Rate Analysis

Jaya Kartheek Devineni

ABSTRACT

The success of the Internet-of-Things (IoT) paradigm relies on, among other things, developing energy-efficient communication techniques that can enable information exchange among billions of battery-operated IoT devices. With its technological capability of simultaneous information and energy transfer, ambient backscatter is quickly emerging as an appealing solution for this communication paradigm, especially for the links with low data rate requirements. However, many challenges and limitations of ambient backscatter have to be overcome for widespread adoption of the technology in future wireless networks. Motivated by this, we study the design and implementation of ambient backscatter systems, including non-coherent detection and encoding schemes, and investigate techniques such as multiple antenna interference cancellation and frequency-shift backscatter to improve the bit error rate performance of the designed ambient backscatter systems.

First, the problem of coherent and semi-coherent ambient backscatter is investigated by evaluating the exact bit error rate (BER) of the system. The test statistic used for the signal detection is based on the averaging of energy of the received signal samples. It is important to highlight that the conditional distributions of this test statistic are derived using the central limit theorem (CLT) approximation in the literature. The characterization of the exact conditional distributions of the test statistic as non-central chi-squared random variable for the binary hypothesis testing problem is first handled in our study, which is a key contribution of this particular work. The evaluation of the maximum likelihood (ML) detection threshold is also explored which is found to be intractable. To overcome this, alternate strategies to approximate the ML threshold are proposed. In addition, several insights for system design and implementation are provided both from analytical and numerical standpoints.

Second, the highly appealing non-coherent signal detection is explored in the context of ambient backscatter for a time-selective channel. Modeling the time-selective fading as a first-order autoregressive (AR) process, we implement a new detection architecture at the receiver based on the direct averaging of the received signal samples, which departs significantly from the energy averaging-based receivers considered in the literature. For the proposed setup, we characterize the exact asymptotic BER for both single-antenna (SA) and multi-antenna (MA) receivers, and demonstrate the robustness of the new architecture to timing errors. Our results demonstrate that the direct-link (DL) interference from the ambient power source leads to a BER floor in the SA receiver, which the MA receiver can avoid by estimating the angle of arrival (AoA) of the DL. The analysis further quantifies the effect of improved angular resolution on the BER as a function of the number of receive antennas.

Third, the advantages of utilizing Manchester encoding for the data transmission in the context of non-coherent ambient backscatter have been explored. Specifically, encoding is shown to simplify the detection procedure at the receiver since the optimal decision rule is found to be independent of the system parameters. Through extensive numerical results, it is further shown that a backscatter system with Manchester encoding can achieve a signal-to-noise ratio (SNR) gain compared to the commonly used uncoded direct on-off keying (OOK) modulation, when used in conjunction with a multi-antenna receiver employing the direct-link cancellation.

Fourth, the BER performance of frequency-shift ambient backscatter, which achieves the self-interference mitigation by spatially separating the reflected backscatter signal from the impending source signal, is investigated. The performance of the system is evaluated for a non-coherent receiver under slow fading in two different network setups: 1) a single interfering link coming from the ambient transmission occurring in the shifted frequency region, and 2) a large-scale network with multiple interfering signals coming from the backscatter nodes and ambient source devices transmitting in the band of interest. Modeling the interfering devices as a two dimensional Poisson point process (PPP), tools from stochastic geometry are utilized to evaluate the bit error rate for the large-scale network setup.

Ambient Backscatter Communication Systems: Design, Signal Detection and Bit Error Rate Analysis

Jaya Kartheek Devineni

GENERAL AUDIENCE ABSTRACT

The emerging paradigm of Internet-of-Things (IoT) has the capability of radically transforming the human experience. At the heart of this technology are the smart edge devices that will monitor everyday physical processes, communicate regularly with the other nodes in the network chain, and automatically take appropriate actions when necessary. Naturally, many challenges need to be tackled in order to realize the true potential of this technology. Most relevant to this dissertation are the problems of powering potentially billions of such devices and enabling low-power communication among them.

Ambient backscatter has emerged as a useful technology to handle the aforementioned challenges of the IoT networks due to its capability to support the simultaneous transfer of information and energy. This technology allows devices to harvest energy from the ambient signals in the environment thereby making them *self-sustainable*, and in addition provide carrier signals for information exchange. Using these attributes of ambient backscatter, the devices can operate at very low power which is an important feature when considering the reliability requirements of the IoT networks. That said, the ambient backscatter technology needs to overcome many challenges before its widespread adoption in IoT networks. For example, the range of backscatter is limited in comparison to the conventional communication systems due to self-interference from the power source at a receiver. In addition, the probability of detecting the data in error at the receiver, characterized by the bit error rate (BER) metric, in the presence of wireless multipath is generally poor in ambient backscatter due to double path loss and fading effects observed for the backscatter link. Inspired by this, the aim of this dissertation is to come up with new architecture designs for the transmitter and receiver devices that can improve the BER performance. The key contributions of the dissertation include the analytical derivations of BER which provide insights on the system design and the main parameters impacting the system performance.

The exact design of the optimal detection technique for a communication system is dependent on the channel behavior, mainly the time-varying nature in the case of a flat fading channel. Depending on the mobility of devices and scatterers present in the wireless channel, it can either be described as time-selective or time-nonselective. In the time-nonselective channels, coherent detection that requires channel state information (CSI) estimation using pilot signals can be implemented for ambient backscatter. On the other hand, non-coherent detection is preferred when the channel is time-selective since the CSI estimation is not feasible in such scenarios. In the first part of this dissertation, we analyze the performance of ambient backscatter in a point-to-point single-link system for both time-nonselective and time-selective channels. In particular, we determine the BER performance of coherent and non-coherent detection techniques for ambient backscatter systems in this line of work. In

addition, we investigate the possibility of improving the BER performance using multi-antenna and coding techniques. Our analyses demonstrate that the use of multi-antenna and coding can result in tremendous improvement of the performance and simplification of the detection procedure, respectively. In the second part of the dissertation, we study the performance of ambient backscatter in a large-scale network and compare it to that of the point-to-point single-link system. By leveraging tools from *stochastic geometry*, we analytically characterize the BER performance of ambient backscatter in a field of interfering devices modeled as a Poisson point process.

To my wonderful family, friends and teachers.

Acknowledgments

The Ph.D. journey has truly been an arduous one although a joyful and rewarding experience at the end, and I would like to thank several people for their support throughout my time in graduate school. First and foremost, I would like to sincerely thank my advisor Dr. Harpreet S. Dhillon for his unwavering support and confidence in me, without whom it would have been very hard to persevere through the program. He has instilled confidence and rigorous thinking in me, and the high expectations set by him has enabled me to grow as a researcher. I have also grown as a person during our general interactions and can take many life lessons with me to follow for the future. I am also grateful to him for giving me the teaching assistance responsibility for the course on Stochastic signals and systems during my pre-final year. I thoroughly enjoyed assisting him in the preparation of homework problems and exam questions. I am also fortunate to experience his teaching first hand when I took the Machine learning course towards the end of my graduate studies. I have learned a thing or two about the background preparation and effort needed to be an effective communicator even when you are teaching a course for the first time.

I would like to express gratitude to my committee members Dr. Buehrer[1], Dr. Reed[2], Dr. Zuo[3], and Dr. Yang[4] for their valuable inputs and constructive feedback on the dissertation work. I took it as a challenge to improve my presentation skills after their sharp criticism during my preliminary exam presentation. I am very proud with how my final defense had gone and I am thankful to them for their critical feedback. I am also grateful to have so many good faculty members at Virginia Tech, particularly Dr. Mackenzie[5] and Dr. Buehrer from Wireless@VT for their courses on Stochastic signals and systems, Information theory, Error coding theory, Digital communication and Multi-channel communication.

I am very lucky to have worked alongside so many intelligent and hardworking colleagues at Durham 470 during my time here. Thank you Mehrnaz[6] for being the best mentor while working on the uplink LTE project alongside Draper laboratories. Your constant guidance during the bi-weekly meetings has been of immense help especially for a budding researcher. I particularly enjoyed the random conversations on science, politics and movies with Priyabrata[7] who has been a dear friend and colleague during my stay here. I am very happy with my recent collaboration with Anish[8] over the past year which has resulted in two conference papers. I believe his first full length journal is just around the corner and wish him good luck for his own Ph.D. journey. Special mention to Morteza[9], Vishnu[10], Mustafa[11], Mohamed[12], Chiranjib[13], Praful[14] and Keerthana[15] for being wonderful labmates.

[1] Dr. Michael R. Buehrer [2] Dr. Jeffrey H. Reed [3] Dr. Lei Zuo [4] Dr. Yaling Yang [5] Dr. Allen B. MacKenzie [6] Dr. Mehrnaz Afshang [7] Priyabrata Parida [8] Anish Pradhan [9] Morteza Banagar [10] Dr. Vishnu Vardhan Chetlur Ravi [11] Dr. Mustafa Kishk [12] Mohamed A. Abd-Elmagid [13] Dr. Chiranjib Saha [14] Dr. Praful Mankar [15] Keerthana Bhogi

And thanks to other colleagues from Wireless@VT: Mohammad[16], Raghu[17], Avik[18] and Tengchan[19].

I have to specially thank few other people in Wireless@VT and ECE department, particularly Hilda Reynolds who is always there to help. And thanks to Nancy and Makensi Ceriani for taking care of travel and conference reimbursements. I am also thankful to my graduate program advisors Mary Brewer, JoAnna Lewis and Laura Villada Esquivel for administrative help and paperwork processing.

I am grateful to National Science Foundation for supporting my research through Grants CPS-1739642 and CNS-1814477. I am also thankful to National Spectrum Consortium (NSC) and Draper laboratories for supporting my initial couple of years while working on the LTE Uplink Project. I would also like to mention my gratitude to MediaTek and my mentor Abhishek[20] for the internship opportunity during the last year of my graduate program.

I am also very lucky to have a good support system, particularly thankful to my undergrad and high school friends Somesh, Sharath, Rahul, Harsha, Dinesh, Shankar, Obaiah, Abhilash, Shanmukha, Sudeep, Rajdeep and Bharat who are always a call away whenever I needed to talk to them. I would also like to thank my friends here in Blacksburg Agastya[21] and Satvik[22] for being wonderful roommates over the past two years.

I am grateful to my wonderful family especially my parents and grandparents for supporting my decision to continue Ph.D. at Virginia Tech and for cheering me up whenever I was down. No amount of gratitude or thankfulness is sufficient for the sacrifices they have made to watch me succeed. I would also like to thank my brother, sister-in-law, and especially my niece for being a stress buster with her innocence and enthusiasm.

The whole world is currently dealing with many problems, primarily the COVID-19 outbreak that is still affecting the way we interact with one another. I thank the doctors, medical staff and the administrators all over the world for their courage and saving many lives. I strongly hope that the world can move past the pandemic and return to normalcy very soon.

[16] Dr. Mohammad Mozaffari [17] Dr. Raghunandan M Rao [18] Avik Dayal [19] Dr. Tengchan Zeng
[20] Dr. Abhishek Roy [21] Dr. Agastya Balantrapu [22] Satvik Chekuri

Contents

List of Figures

List of Tables

Chapter 1

Introduction

Internet of Things (IoT) has been envisioned as a network of tightly integrated devices connected to the internet which automate the decision making of everyday processes without the need for human intervention. This unprecedented integration of billions of physical devices such as sensors, actuators, wearables, home appliances and vehicles into the computer network opens up fundamental new ways of sensing and controlling variety of processes around us. For this vision to be successful, first the devices have to be *self-sustainable* as they are typically deployed in inaccessible locations, and second they should also be capable of supporting continuous exchange of information to take appropriate actions for the physical processes they are monitoring. Due to its ability to support these requirements of the IoT devices, ambient backscatter is quickly becoming one of the most promising technologies for the future wireless networks. The main premise of the ambient backscatter technology is to jointly utilize the ambient radio frequency (RF) waves such as cellular/Wi-Fi or television (TV) signals for harvesting energy to power the device and also as carrier for the data transmission. The ubiquitous presence of wireless networks provide a reliable source of EM waves even at inaccessible locations which can be utilized both for power and information exchange. Especially, the main advantage of the backscattering mechanism implemented for data modulation is that it precludes the use of power-intensive RF-chain components such as mixers, analog-to-digital converters (ADCs) and digital-to-analog converters (DACs), thereby greatly reducing the energy consumption [2, 3]. Although the ambient backscatter technology has shown a lot of potential, a strong theoretical foundation of the physical layer aspects of the technology is still in the nascent stages of the development. Therefore, the main objective of this dissertation is to develop a good theoretical understanding of the ambient backscatter by proposing new transmitter and receiver designs, and thoroughly investigating the signal detection and performance of the proposed techniques.

This introductory chapter is divided into three main sections. First, the background on the conventional and ambient backscatter, the main challenges and of the ambient backscatter technology and the limitations of the prior art are provided in Section 1.1. This section will also provide a good motivation for the different problems investigated in the dissertation work. Second, the main contributions of each of the studied problems are discussed in Section 1.3. Third, the organization of the remaining document is provided in Section 1.4 for the convenience of the reader. Finally, the list of the accepted and submitted publications from our work are provided at end of the introductory section.

1.1 Background

Traditional communication systems are inherently symmetric in the sense that both the transmitting and receiving devices use transceivers to modulate data onto carrier signals generated by their RF circuits. In other words, devices on both ends of a link implement power-hungry components like ADCs, DACs, mixers and power amplifiers. On the other hand, backscatter communication systems are asymmetric, meaning that one of the devices acts as a source by actively transmitting the carrier waves, and another device scavenges on the waves to transmit its own data by reflecting them to a receiver, which can either again be the source or a separate entity completely. The source and scavenging entities in the system are termed as *active* and *passive* devices, respectively. In the conventional backscatter, for example radio frequency identification (RFID), the source and receiver are same, while in the ambient backscatter the receiver is different from the source. The RF components of a backscatter device are designed such that the power hungry components are removed from the chain or replaced with low power alternatives. Hence, the backscatter systems can operate at a very low power compared to traditional devices, which is especially appealing from the perspective of extending the lifetime of IoT devices. The backscatter technology also has a wide-scale of applications in localization which range from the tracking of users in smart homes, low-cost tracking of objects to develop industrial automation in small-scale industries, and localization of in-body implants during surgical procedures.

A major limitation of the conventional backscatter systems is the requirement of standalone equipment to generate the source RF signals. Ambient backscatter, developed in [2, 3], is the first successful implementation of a backscatter system, which relied on the ambient RF waves for power source and circumvented the need for additional hardware to generate the source signals. This was followed by several other prototypes which established the feasibility of the ambient backscatter systems. However, ambient backscatter systems suffer from the same limitations of the conventional backscatter such as range and the direct link interference, which are in fact further aggravated in the case of ambient backscatter. In the next section, we discuss the challenges and limitations faced by ambient backscatter systems, which will form the main motivating factor for the work investigated in the later chapters of the document.

1.1.1 System Setup and Backscatter Operation

The setup of the ambient backscatter system and the operating mechanism of a general backscatter system are presented now. We consider a pair of devices, of which one is a backscatter transmitter (BTx) and the other is a receiver (Rx). The system model of the general ambient backscatter setup is shown in Fig. 1.1a. We assume the presence of modulated carrier waves generated by a source in the environment, henceforth referred to as *ambient waves* and *ambient source* respectively, and the devices communicate through scattering of the incident ambient waves as described shortly. This is a valid assumption since such sources of carrier waves, for example TV, cellular or Wi-Fi networks, are almost

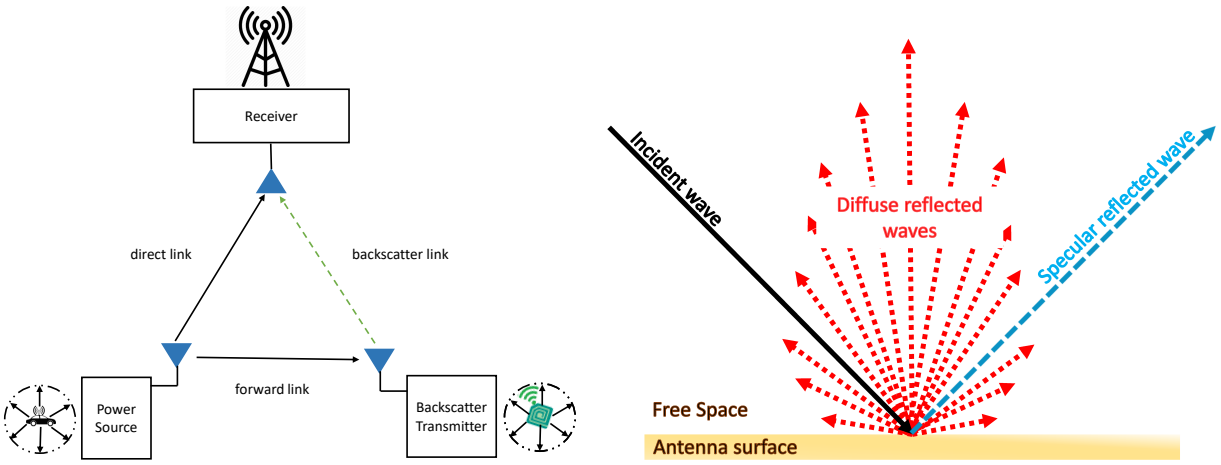

(a) (b)

Figure 1.1: (a) System model of the ambient backscatter setup, (b) Illustration of diffuse reflection and specular reflection.

omnipresent. Backscatter derives its name from the mode of information exchange, which is to communicate data through reflection of RF waves, and the procedure of backscattering ambient RF waves is called *ambient backscatter*. The word *backscatter* simply refers to the process of backward reflection of incident waves at a surface in different directions (called *diffuse reflection*), unlike the typical single reflection observed at the surface of a mirror (called *specular reflection*). This phenomenon is similar to how visible light is reflected by normal objects in all directions (not just a single reflection as in the case of a mirror) and is illustrated in Fig. 1.1b. There are some noteworthy differences between the ambient backscatter and conventional backscatter systems that contrast the implementation and design aspects of the two technologies. First and foremost, ambient backscatter uses ambient RF signals which are modulated carriers with encoded data, that necessitates the design of alternate decoding mechanisms at the receiver which are different from the ones implemented in conventional backscatter systems. Second, ambient backscatter systems do not require any dedicated hardware to generate signals for powering the devices, unlike the conventional backscatter systems that require a stand-alone device to continuously emit power signals.

In order to understand the operation of data modulation using backscatter, it is essential to look at the propagation of an electromagnetic (EM) wave between different surfaces. When EM waves propagating through free space hit the antenna, part of the wave is reflected back into free space due to the difference between the impedance of free space and antenna. The reflection coefficient Γ of the antenna, defined as the ratio of the amplitudes of the reflected wave to the incident wave, is given by:

$$\Gamma = \frac{A^-}{A^+} = \frac{\frac{Z_L}{Z_0} - 1}{\frac{Z_L}{Z_0} + 1}, \tag{1.1}$$

where Z_L is the impedance of the antenna and Z_0 is the impedance of free space. When $Z_L = Z_0$, the wave is completely absorbed with no reflection and the impedance matching is known as *reflection-less* matching. On the other hand, for $Z_L = 0$ the wave is completely reflected. Therefore, one can simply change the impedance of the antenna according to the data to be transmitted to generate a modulated reflected wave.

This phenomenon is exploited by the backscatter systems in a slightly modified way, where data modulation on the reflected wave is realized by manipulating the impedance mismatch between antenna and the load component (which forms the main circuit). The main reason is that, in a typical backscatter device, the chip is directly placed at the terminals of the antenna [4]. The load impedance is typically a complex value, due to which the wave reflection needs to be analyzed in terms of power [5]. Hence, the reflection coefficient Γ at the boundary between antenna and load is characterized in terms of power rather than voltage. The reflection coefficient here, termed as *power wave reflection coefficient*, is given by [5]:

$$\Gamma = \frac{\frac{Z_L}{Z_a^*} - 1}{\frac{Z_L}{Z_a} + 1}, \tag{1.2}$$

where Z_L and Z_a are the impedances of the load and antenna respectively and the symbol $*$ represents complex conjugate. In order to transfer all the power to load, the load impedance is set to $Z_L = Z_a^*$ which is known as *maximum power transfer* matching. On the other hand, in order to reflect all the power, the load impedance is set to $Z_L = 0$. Therefore, $Z_L = Z_a^*$ and $Z_L = 0$ are known as *non-reflecting* and *reflecting* states, respectively. The backscatter system can leverage this to modulate data by tuning impedance of the load to vary reflection coefficient at this boundary. In general, the signal scattered from the backscatter device to the receiver is given by [6]:

$$r = (A - \Gamma)\, s = As - \Gamma s, \tag{1.3}$$

where r is the signal at the receiver, s is the signal backcattered at the device, A is the load-independent complex coefficient of the device, and Γ is the reflection coefficient of backscatter node at the boundary of the antenna and the circuit. The device modulates the signal by varying the load impedance to change the parameter Γ that controls the reflected signal. The first and second terms in (1.3) correspond to the *structural mode* and *antenna mode* scattering components, respectively. A binary modulation scheme can be implemented by choosing two different values Γ_0 and Γ_1. As shown later, non-coherent detection will result in good error performance only for the case of on-off keying (OOK) modulation. It is possible to achieve this modulation for antennas with $|A| \leq 1$ by designing the appropriate load impedance using only passive components [7, 8]. A simple modulation scheme is to tune the circuit between reflecting and non-reflecting states when transmitting bits 1 and 0, respectively.

1.1.2 Link Budget of Backscatter Communication

The general belief regarding the communication range of backscatter is that the operational distance of the technology is much less compared to the required values for effective

far-field communication. While that may be true in some cases, there are ways to improve the communication range for example by deploying the ambient backscatter in *bistatic* mode instead of a *monostatic* operation. In the *monostatic* mode, the antenna of the ambient PS and Rx are one and the same and located on a single device, while in case of the *bistatic* mode the antenna of the ambient power source (PS) and Rx are different and located on two separate devices. The link budget study of a communication link provides a good estimate of the expected communication range. So, we will analyze the link budget of the ambient backscatter under simplified assumptions. The signal component propagating through the backscatter transmitter node determines the transmission range of backscatter communication. The path corresponding to this component is composed of two links: 1) *forward link* from the power source to the backscatter transmitter, and 2) *backscatter link* from the backscatter transmitter to the receiver. The free space Friis transmission equation for the overall backscatter link in bistatic operation mode is

$$P_R = \frac{P_T G_R G_T G_t^2 \lambda^4}{(4\pi)^4 r_f^2 r_b^2}, \tag{1.4}$$

where P_R is the received power at the Rx node, P_T is the isotropic transmit power of the ambient PS, G_R, G_T and G_t are the linear free space antenna gains of the Rx, PS and BTx, respectively, λ is the wavelength of the EM carrier wave (inversely related to its carrier frequency f), r_f is the separation between PS and BTx nodes in the forward link distance, and r_b is the separation between BTx and Rx nodes in the backscatter link. The same equation when represented in decibel (dB) form is

$$P_R = P_T + G_T + 2G_t + G_R - 20\log_{10} r_f - 20\log_{10} r_b - 40\log_{10} f - 64.88, \tag{1.5}$$

where the powers P_R and P_T are in dBm, gains G_T, G_t, and G_R are in dBi, the distances r_f and r_b are in km, and frequency f is in MHz. For a monostatic or co-located bistatic backscatter, where the PS and Rx are the same device, the equation can be further simplified as

$$P_R = P_T + G_T + 2G_t + G_R - 40\log_{10} r - 40\log_{10} f - 64.88, \tag{1.6}$$

where r is the separation between PS/Rx and BTx in km.

Now, we discuss the link budget performance of the ambient backscatter in ISM bands by considering the carrier frequencies of 915 MHz and 2.4 GHz. For this, we evaluate the feasibility of operating these devices under two extreme cases of signal-to-noise ratio (SNR) values under both general (bistatic) and monostatic/co-located bistatic mode of operation. The isotropic transmit power of the ambient PS is considered to be 36 dBm, while the Rx sensitivity is assumed to be -110 dBm. Considering a noise floor level of -174 dBm/Hz, the received signal power levels corresponding to the SNR values of 35 dB and -5 dB in a 10 MHz band are given by -69 dBm and -109 dBm, respectively. The second SNR considered for this discussion is close to the receiver sensitivity which will provide a good estimate for

Monostatic			Bistatic		
Freq. / SNR	915 MHz	2.4 GHz	Freq. / SNR	915 MHz	2.4 GHz
35 dB	22 m	8 m	35 dB	50 m	7 m
-5 dB	220 m	83 m	-5 dB	4.79 km	708 m

Table 1.1: Operating distance of ambient backscatter: monostatic distance r, and bistatic distance r_b (the forward link separation for bistatic mode is set to $r_f = 10$ m).

the range of operation of the backscatter communication under different setups. For this discussion, the antenna gain values are configured as $G_R = G_T = 6$ dBi and $G_t = 0$ dBi. For the bistatic operation mode, the separation distance in the forward link is configured to 10 m.

First, as expected, the operating distances of the backscatter in 2.4 GHz are small compared to the operating distances in 915 MHz. This is explained by the larger pathloss encountered by 2.4 GHz due to higher operating frequency of the band. The operational range of monostatic backscatter is 220 m and 83 m for the bands 915 MHz and 2.4 GHz, respectively, while the ranges under bistatic operation are 4.79 km and 708 m, respectively, for the same frequency bands. Our second observation is that the operational range of backscatter in monostatic mode is much lower compared to that of the bistatic mode. The operating distances of monostatic backscatter at an SNR of 35 dB are 22 m and 8m, respectively, for the 915 MHz and 2.4 GHz. On the other hand, the operating distances for the bistatic mode are 50 m and 7 m for the two same bands, respectively. These operating distances and ranges of the ambient backscatter are similar to the values observed in the real world deployment [9,10]. As will be discussed later, the main limiting factor for the ambient backscatter range is the interference from the direct link and the authors in [9,10] tackle that by either shifting the backscattered signal to a new non-overlapping frequency band [9] or spread spectrum based techniques to detect in the presence of the interference [10]. By frequency shifting the backscatter signal to remove the self-interference from the direct signal from the power source [9] achieved operating range of 3.4 km in bistatic mode of operation similar to ours. On the other hand, spreading techniques utilized in [10] can achieve ranges of 475 m and 2.8 km when operating in monostatic and bistatic mode, respectively.

Since our goal here was to provide a general idea about the potential ranges of the ambient backscatter links in different scenarios, this basic link budget discussion did not consider antenna and other losses that are inherent in the EM propagation for the backscatter. For a more thorough discussion on the link budget for ambient backscatter, interested readers are advised to refer to [11].

1.1.3 Performance Characterization

A natural extension to the link budget analysis is the characterization of the performance of the communication system. Due to the inherent randomness present in the communication system, because of either the receiver noise or the multi-path propagation, there is no guarantee that the received signal can be decoded within the communication range attained from the link budget study. It is therefore, important to characterize the system performance in terms of a metric that can fundamentally capture the random nature of the communication systems, such as the bit error rate (BER). For voice and video applications, the packet error rate (PER) is considered as a good estimate of the quality of service (QoS) since these applications can tolerate some packet errors. And it can be shown that, for small values of BER, the PER is linearly proportional to the BER and the packet size. Hence, the BER can be an effective measure of the QoS for these applications. On the other hand, data applications cannot tolerate packet errors and require either error correction mechanisms or retransmissions whenever errors are detected (implemented using redundant or parity bits). For these applications, perhaps latency is a more relevant metric to characterize the performance. Even here, BER can provide some measure of the expected performance since latency will increase with the BER. In all of our studies in this dissertation, the BER metric is used to quantify the performance of the ambient backscatter.

1.1.4 Challenges and Limitations

Due to the asymmetric operation of the ambient backscatter systems, the direct signal from the source to the receiver will act as interference, which needs to be accounted for in the detection mechanism of the receiver designs. Another serious limitation of the backscatter systems, due to this asymmetric operation, is the *two-way* propagation loss resulting in a limited communication range. In addition, the receivers in the ambient backscatter systems have to detect the backscatter data in the presence of the unknown and random ambient RF data. To facilitate this, the receivers perform some kind of averaging operation on the received signal samples to remove the impact of the unknown RF data. For a quick and wider adoption of the ambient backscatter technology, it is highly important to overcome these challenges and limitations of the ambient backscatter. Another important challenge in ambient backscatter is the frequency domain response of the reflected backscatter signal. The resultant backscatter signal of the ambient backscatter is the product of the ambient data signal and the backscatter data signal waveforms. The corresponding frequency domain waveform is given by the convolution of the frequency response of the individual waveforms. The exact impact on the bandwidth requirement of the reflected backscatter signal can be clearly understood from the following example. Suppose that the symbol duration of the ambient and backscatter data symbols are assumed to be equal, and that the waveforms are considered to be rectangular in the frequency domain. The bandwidth occupied by the backscatter signal will be twice the bandwidth of the independent waveforms since the convolution of two rectangular waveforms will result in a triangular waveform. In this case, one needs to take care to design the appropriate filter at the receiver so as to avoid losing

important signal information. Another point to note here is that the backscatter system does not have any control over the bandwidth used for the ambient signal transmission, meaning that the additional bandwidth occupied by the backscatter signal can be outside the bandwidth of the ambient signal. This will mean that there should either be enough guard band or the receiver has to have a mechanism to handle the unwanted interference from the neighboring transmissions. For the example above, the guard band required is more than double the bandwidth of the ambient signal which may not be feasible. This important aspect of the bandwidth requirement is generally ignored in many earlier studies of the ambient backscatter which will result in impractical systems showing very high promise but are not practically possible. One way to handle the additional bandwidth requirement is to limit the bandwidth requirement of the backscatter symbols by keeping the symbol duration to be much higher than that of the ambient data symbols.

Next, we briefly describe the approaches taken in the literature to overcome these challenges, and highlight how our work differentiates from these earlier investigations.

1.2 Selected Prior Art and Motivation

As discussed earlier, BER is one of the most widely used metric to benchmark the performance of communication systems, and is the metric used to characterize the performance of the ambient backscatter system in all of our studies. To be precise, the main focus of our work is to design different ambient backscatter systems, evaluate the theoretical BER of these systems, and come up with novel ways of improving the BER performance. The evaluation of the theoretical BER expressions allows one to find the main parameters that significantly impact the BER and provide some insights into the system design. Only the prior art relevant for our discussion here is mentioned in this section, with the exhaustive list of previous studies on ambient backscatter discussed in the later technical chapters.

Some of the earlier studies on the theoretical aspects of ambient backscatter like throughput and error rate performance are investigated in [1,12–19]. The test statistic used for signal detection in these studies is based on the average energy of the received signal samples. The design of maximum-likelihood and equiprobable-error detectors was first investigated in [12]. The detection using non-coherent and semi-coherent techniques at a receiver without channel state information was studied in [1, 13–15]. The detection of ambient backscatter signal with multiple receive antennas was performed in [16]. The statistical-covariance based signal detection to improve the BER of the system was investigated in [18]. The BER analysis of detection over ambient orthogonal frequency division multiplexing (OFDM) signals using interference cancellation techniques was investigated in [19]. However, the key enabler of the analysis in [1, 12–19] was the approximation of the probability density function (PDF) of the test statistic as Gaussian distributed. In the aforementioned works, the following two fundamental problems are still open despite all these studies on detection and BER analysis of the ambient backscatter systems: (i) the characterization of the exact distribution of the test statistic based on the average signal energy, and (ii) the characterization of exact average

BER in fading channels. These two problems are tackled in our first work [20] (Chapter 2), which distinguishes our work from the previous studies.

As pointed out earlier, the interference from direct link is one of the main factors limiting the performance of the ambient backscatter systems. In fact, the negative impact of this interference is demonstrated in our first work [20] (Chapter 2) by deriving the BER of the system. The investigation into the prototype development for the suppression of the direct link interference to improve the performance were first studied in [21, 22]. The theoretical investigation on the direct link suppression techniques are studied in [23, 24]. In [23], the prefix based repeating structure of the OFDM signalling is leveraged to remove the direct link interference. The receiver will have two copies of the same signal in each OFDM symbol that can be used to subtract and remove the direct link. Multiple antenna receivers are used in [24] using SIC based signal detection to successively decode backscatter data transmitted at a rate equivalent to that of the ambient RF data. In our second work [25] (Chapter 3), we have studied this problem of direct link interference suppression by designing a system that utilizes multiple antennas at the receiver to track the angle-of-arrival (AoA) of the direct link, and use it to remove the interference. The novelty of the work lies in the ability of the receiver to estimate the large scale parameter AoA and utilize it to non-coherently remove the direct link interference. For the same setup, in our third work [26] (Chapter 4), we have investigated the utilization of Manchester encoding at the transmitter, where we have shown the simplification of the detection procedure and the additional SNR gain of the new system.

Another method to improve the backscatter performance is to shift the backscatter signal to a frequency region different from the ambient interference signal [3,9,10,27–29], known as frequency-shift ambient backscatter. Mainly, [9, 10] demonstrated techniques that have shown to achieve long range (LoRa) backscatter with the communication range improved by an order of magnitude more. In our fourth work (Chapter 5), we have investigated the performance of frequency-shift ambient backscatter by evaluating the BER of a non-coherent receiver in a large-scale network. The available literature on stochastic geometry related to ambient backscatter network analysis is mainly focused on the power outage and coverage analysis [30–41]. It should be emphasized that none of these studies have analyzed the BER of backscatter in a large-scale network and our work is the first such comprehensive study underlining the contribution of our work. The impact of small-scale fading and the large-scale pathloss are investigated in the single-link interfering system and the large-scale interference network, respectively. In considering such large scale network, we have leveraged concepts from the stochastic geometry to evaluate the BER, and the contributions from this work go much beyond the simple BER analysis of a single link setup.

1.3 Contributions and Outcomes

In this section, the main contributions of our various studies are discussed.

Coherent and Semi-coherent detection in Slow Fading. We characterize the exact bit error rate for the ambient backscatter system with coherent and semi-coherent detectors. In addition, we explore the evaluation of maximum likelihood threshold, and provide two alternate detection threshold techniques due to the complexity of ML detection. The main feature of the analysis that distinguishes our work from the literature is the characterization of the exact conditional density functions of the average received signal energy for this setup. The key challenge of the analysis lies in the handling of correlation between the two channel gains of the binary hypothesis testing problem for the derivation of joint probability distribution of magnitude squared channel gains.

Non-coherent detection in Time-Selective Fading. The receiver architecture for the non-coherent detector used in this work is based on the direct averaging of the received signal samples, which departs from the conventional energy averaging-based receivers used in the literature. The impact of the direct link interference on the bit error rate is demonstrated by the poor performance of the non-coherent single-antenna receiver. The improvement in BER is realized by the interference nulling using a multi-antenna receiver, which removes the direct link interference non-coherently by tracking the AoA of the link. In addition, the analysis also quantifies the effect of improved angular resolution on the BER as a function of the number of receive antennas. A key intermediate step is the derivation of a new concentration result for a general sum sequence encountered while deriving the conditional distributions of the received signal.

Manchester Encoding for Non-coherent detection. The impact of encoding is investigated by evaluating the bit error rate of an ambient backscatter system with Manchester encoding implemented at the transmitter side. It is shown that the detection procedure of the non-coherent detector simplifies as a result of this encoding scheme. In addition, it is also demonstrated through extensive numerical results that there is an SNR gain of $3-4$ dB over the direct on-off (OOK) modulation in case of a multi-antenna receiver.

Frequency-Shift Ambient Backscatter. The mechanism of frequency-shifting the impending source signal by a backscatter node to spectrally separate the reflected signal can result in improved performance due to self-interference mitigation. The main goal of this paper is to investigate the bit error rate (BER) performance of such frequency-shift ambient backscatter system in a large-scale network. To achieve this, we first characterize the performance of a system implementing non-coherent detection in the presence of a single interfering device. Then, we compare the performance of the system in large scale network with interference devices modeled as a homogeneous Poisson point process (PPP). An interesting observation from our analysis is that the BER in general tends to gradually decrease with respect to the increasing sample-size of the averaging operation used in the backscatter system. As expected, the BER performance of the system in the large-scale network is

determined by the intensity of the point process of the interfering devices.

1.4 Organization

In Chapter 2, we present our work on bit error analysis of the coherent and semi-coherent ambient backscatter system in a slow fading channel. In Chapter 3, we discuss our work on non-coherent detection of ambient backscatter in time-selective fading using a multi-antenna receiver. Modeling the time-selective fading using a auto-regressive process, we obtain tractable expressions for the detection threshold and bit error rate. In Chapter 4, we improve the performance of the non-coherent ambient backscatter by transmitting Manchester encoded data symbols. In Chapter 5, we present our work on the non-coherent detection of frequency-shift ambient backscatter in a large-scale network. In Chapter 6, we summarize the main contributions of our work and briefly touch upon the potential future work.

1.5 List of Publications

This work has led to several journal and conference papers which are listed below.

Journals

- **J. K. Devineni** and H. S. Dhillon, "Ambient backscatter systems: Exact average bit error rate under fading channels", *IEEE Trans. on Green Commun. and Networking*, vol. 3, no. 1, pp. 11-25, 2019.

- **J. K. Devineni** and H. S. Dhillon, "Non-coherent detection and bit error rate for an ambient backscatter link in time-selective fading", *IEEE Trans. on Commun.*, vol. 69, no. 1, pp. 602-618, Jan. 2021.

- **J. K. Devineni** and H. S. Dhillon, "Manchester encoding for non-coherent detection of ambient backscatter in time-selective fading", *IEEE Trans. on Veh. Technology*, vol. 70, no. 5, pp. 5109 - 5114, Apr. 2021.

- **J. K. Devineni** and H. S. Dhillon, "Asymptotic bit error rate of non-coherent frequency-shift ambient backscatter in a large-scale network", *To be submitted*.

Conference Proceedings

- **J. K. Devineni** and H. S. Dhillon, "Exact bit error rate analysis of ambient backscatter systems under fading channels", Proc., *IEEE Veh. Technology Conf. (VTC)*, pp. 1-6, Aug. 2018.

- **J. K. Devineni** and H. S. Dhillon, "Non-coherent signal detection and bit error rate for an ambient backscatter link under fast fading", *Proc., IEEE Globecom*, Dec. 2019.
- **J. K. Devineni** and H. S. Dhillon, "Multi-antenna non-coherent detection of ambient backscatter under time-selective fading", *Proc., IEEE Globecom*, Dec. 2020.

Chapter 2

Bit Error Rate of Coherent and Semi-Coherent Ambient Backscatter under Slow Fading

2.1 Introduction

Ambient backscatter, with its technological capability of enabling low-rate and low-power communication among energy-constrained devices, is considered as a promising solution for the reliable exchange of data in the Internet-of-Things (IoT) paradigm. The main premise of ambient backscatter is to use omnipresent ambient EM waves, such as the radio frequency (RF) waves, cellular/WiFi or television (TV) signals, to both harvest energy at small IoT devices as well as to use these existing waves as carriers for data transmission. The utilization of backscattering mechanism for data modulation precludes the requirement of power-intensive RF-chain components like RF mixers, analog-to-digital converters (ADCs) and digital-to-analog converters (DACs), which greatly reduces the energy requirements of the circuit [2, 3]. Such a technology is especially attractive for IoT devices deployed at hard-to-reach locations for which recharging or replacing batteries may not be economically viable. The ubiquitous presence of wireless networks provide a reliable source of EM waves that can be utilized by such devices for data transmission using backscattering. Due to the wide-ranging potential advantages of this technology, it is of immediate interest to characterize various aspects of its performance accurately. In this work, we provide an exact characterization of BER for these ambient backscatter systems in a flat fading channel both in the presence and absence of channel state information (CSI).

2.1.1 Related Work

Although ambient backscatter communications have gained prominence recently, initial research on the fundamentals of backscatter systems dates back to 1948 when it was first applied in radar systems [42]. Later in the early 1990s and 2000s, it found a prominent application in inventory tracking and identification through radio frequency identification (RFID) systems. A serious drawback of these systems compared to traditional point-to-point communications is the *two-way* propagation loss resulting in a limited communication range. This motivated the study of channel characteristics and distance limitations of the conventional backscatter systems in [43,44]. To overcome this limitation, approaches such as

bistatic backscatter [45] were explored for improving range. The use of coding techniques and multiple antennas for performance improvements was explored in [46–49]. The security and protocol aspects of backscatter systems to achieve reliable communication were investigated in [50, 51].

A major drawback of the conventional backscattering systems is the need for a standalone equipment to send the source RF signals, which are scattered back by devices such as a moving vehicle or miniature tags. Ambient backscattering [2, 3] is the first successful implementation of backscatter systems that circumvents the need for extra hardware, thereby reducing the cost of infrastructure and maintenance. Some of the recent prototype implementations of the ambient backscatter include low-power communication to nearby devices by leveraging the TV/cellular waves [2], multiple antenna and coding techniques for improved throughput and range, respectively [52], passive Wi-Fi transmissions with very low circuit operational power [53], low-power self-interference cancellation techniques for full-duplex transmissions and frequency-modulation (FM) backscattering for smart and connected cities [54], inter-technology backscatter to convert Wi-Fi packets into bluetooth transmissions [27], and long range (LoRa) low-power communications in the battery-less devices [9, 10]. These proof-of-concept systems have demonstrated the feasibility of practical implementation of the ambient backscatter technology.

On the other hand, investigation into the theoretical aspects of ambient backscatter like throughput, error rates, and performance is still in the nascent stage. Several important steps in this direction had been taken in [1, 12–19]. The design of maximum-likelihood and equiprobable-error detectors was first investigated in [12]. The detection using non-coherent and semi-coherent techniques at a receiver without channel state information was studied in [1, 13–15]. The detection of ambient backscatter signal with multiple receive antennas was performed in [16]. The statistical-covariance based signal detection to improve the BER of the system was investigated in [18]. The BER analysis of detection over ambient orthogonal frequency division multiplexing (OFDM) signals using interference cancellation techniques was investigated in [19]. The capacity and throughput limits of an ambient scattering system were studied in [55]. In [56], the performance analysis of ambient backscatter in a network setup was performed in terms of the coverage probability and the transmission capacity using stochastic geometry framework.

The key enabler of the analysis in [1, 12–19] was the approximation of the probability density function (PDF) of average energy of the received signal as Gaussian distributed. Despite the progress made in detection and BER analysis of the ambient backscatter systems in the aforementioned works, the following two fundamental problems are still open: (i) the characterization of the exact distribution of average signal energy and (ii) the characterization of exact average BER in fading channels. Tackling these two problems is the main focus of this paper. Further details on the main contributions of the paper are provided next.

2.1.2 Contributions and Outcomes

Exact conditional distributions and detection mechanisms We investigate signal detection in ambient backscatter for two types of receivers, which we refer to as: i) receiver with CSI ($\mathcal{R}_1$) and ii) receiver without CSI ($\mathcal{R}_2$). We show that the exact conditional density functions of the average energy of the received signal follow noncentral chi-squared distribution (NC-χ^2). Characterization of the exact conditional signal distribution is an important component in the exact performance analysis, which differentiates our work from the earlier works that approximated this distribution as Gaussian [1, 12, 13, 16]. A binary hypothesis testing problem is formulated and the detection is performed by comparing the average energy of the signal to a threshold. Three detection strategies are considered for receiver $\mathcal{R}_1$: i) *mean threshold (MT) detection* in which the threshold is calculated as the mean of conditional expectations of the average signal energies received under different hypotheses, ii) *maximum likelihood threshold (MLT) detection* in which the threshold is evaluated as intersection point of the exact conditional PDFs, and iii) *Approximate MLT detection* where threshold is evaluated as the intersection point of approximations of the conditional PDFs. For receiver $\mathcal{R}_2$, differential encoding strategy is used at the transmitter to overcome the ambiguity in decoding process [2]. Simple threshold evaluation strategies, such as the MT threshold, are used in $\mathcal{R}_2$ because of the lack of complete channel information at the receiver in this case.

Joint distribution of correlated fading components A key challenge in the error analysis is the need to characterize the joint distribution of correlated fading components belonging to the different hypotheses. In particular, although the individual links in the system may experience independent fading, overlapping backscatter data onto radio signals eventually results in different but correlated fading components for the two hypotheses. A key driver of this evaluation is the independence of the fading component of alternate hypothesis conditioned on the fading component of null hypothesis. Further, characterization of the conditional BER in terms of the generalized Marcum Q-function allows us to come up with several system insights, which are discussed next.

Insights Using the conditional BER expressions, we deduce that the optimal performance of ambient backscatter is dependent only on signal-to-noise (SNR) of the ambient signal and not on the individual strengths of the ambient signal and noise. This trend is similar to the performance of the standard binary phase shift keying (BPSK) modulation in the classical setup. Second, the decay rate of BER defined as the rate of depreciation is observed to decrease with the increasing sample length N. This is in contrast to the constant BER decay rate observed when plotted against SNR of the signal. Third, the SNR gain of the system follows diminishing returns with increasing value of the sample length N. Further, our results show that there is no noticeable difference in the BER performance of the three detection threshold techniques considered in this work. Therefore, simpler techniques, such as the MT

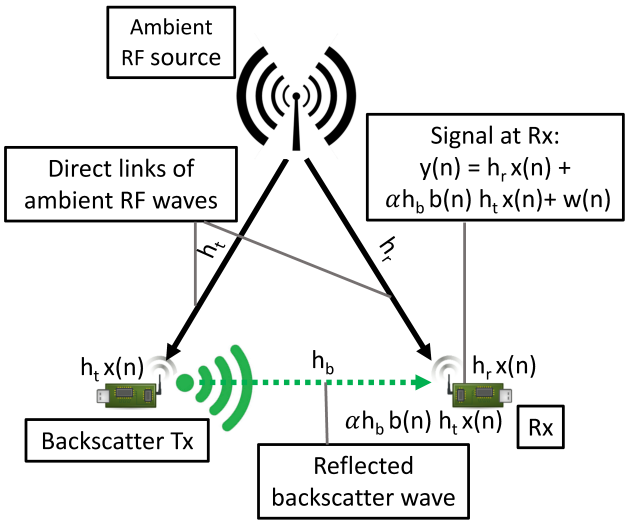

Figure 2.1: System model of ambient backscatter communication system.

technique, can be implemented without much degradation of the system performance.

2.2 System Model

We consider a pair of devices, of which one is a backscatter transmitter (BTx) and the other is a receiver (Rx). We assume the presence of modulated carrier waves generated by a source in the environment, henceforth referred to as *ambient waves* and *ambient source* respectively, and the devices communicate through scattering of the incident ambient waves. The system model for the ambient backscatter is illustrated in Fig. 2.1. The devices in the network are assumed to either have their own power source or generate enough power from the ambient waves to run their circuits. The latter assumption is quite reasonable because the ambient backscatter systems are designed to operate at a very low power, of the order of few micro-watts.

2.2.1 Channel Model

In this paper we focus on flat Rayleigh fading channel. Handling more general fading distributions is a useful direction of future work. In the backscatter setup illustrated in Fig. 2.1, there are two direct communication links, one each from *ambient source* to transmitter and receiver, and one backscatter communication link, from transmitter to receiver. The fading components of the direct links to receiver and transmitter, and the backscatter link are independent, identically distributed and are denoted by h_r, h_t and h_b, respectively. The variance $\sigma^2_{h_2}$ of the backscatter link h_b is assumed to be different from the variance $\sigma^2_{h_1}$ of the direct links h_r and h_t. When the communication range of backscatter is significantly high, the variance $\sigma^2_{h_2}$ is set to a value smaller than unity to model the additional attenuation. In

our setup, however, the extra attenuation in the backscatter link is assumed to be negligible and the large-scale fading is taken to be correlated, thus allowing us to capture the large-scale channel effects directly into the received SNR. The average energy of the ambient signal is assumed to be unity and the variance σ^2 of zero mean additive complex Gaussian noise is varied to obtain different SNR values. For this reason, the exact units of signal energy are not needed and SNR is used as a measure of the signal strength in the distribution plots.

2.2.2 Signal Model

At the BTx, a simple binary on-off modulation scheme is implemented by appropriately configuring the reflection coefficients Γ_0 and Γ_1 to transmit digital bits. The desired signal at the Rx (shown in Fig. 2.1) is the sum of two components, one directly received from the *ambient source* and the other reflected from the BTx. The received signal of an ambient backscatter system is mathematically expressed as follows:

$$y(n) = \underbrace{h_r x(n)}_{\text{radio signal}} + \underbrace{\alpha h_b\, b(n)\, h_t x(n)}_{\text{backscatter signal}} + \underbrace{w(n)}_{\text{i.i.d Gaussian noise}}, \tag{2.1}$$

where $x(n)$ is the complex baseband signal of the ambient source, $w(n)$ is the additive complex Gaussian noise at the receiver, $b(n) \in \{0, 1\}$ is the backscatter data, and α is related to the parameter Γ_1 of the BTx node. It should be noted that the backscatter data $b(n)$ has to be decoded in the presence of ambient source data $x(n)$ which is unknown at the receiver node.

Assuming that the data rate of backscatter communication is significantly lower than the data rate of ambient source (reasonable assumption for most IoT applications), the receiver can filter out the data $x(n)$ of ambient source by simply averaging the energy of the received signal over N samples, where N is the window over which the backscatter data $b(n)$ remains constant [2]. We note that no further assumptions, for example on the distribution of the ambient symbol sequence, are made except the following one. The average energy of $x(n)$ over the sample length N is assumed to be a constant given by:

$$\bar{E} = \frac{1}{N} \sum_{n=1}^{N} |x(n)|^2. \tag{2.2}$$

By taking $b(n) = b$ over sample length N, the model in (2.1) can be simplified, as follows:

$$y(n) = (h_r + \alpha h_b h_t b)\, x(n) + w(n), \qquad (1 \leq n \leq N). \tag{2.3}$$

To further simplify the model, received signal $y(n)$ can be expressed separately for each value of bit b with the following fading components:

$$y(n) = \begin{cases} h_0\, x(n) + w(n), & b = 0, \\ h_1\, x(n) + w(n), & b = 1, \end{cases} \tag{2.4}$$

where $h_0 = h_r$ and $h_1 = h_r + \alpha h_b h_t$ are fading components dependent on backscatter data b. The magnitude square of the fading components are denoted by $\mu = |h_0|^2$ and $\nu = |h_1|^2$.

Remark 2.1. It should be noted that the fading terms h_0 and h_1 (also μ and ν) are different and are correlated due to the common term h_r in their expressions, unlike a traditional BPSK system which has a single fading term.

2.2.3 Receiver Types

The BER performance of the two receiver types $\mathcal{R}_1$ and $\mathcal{R}_2$, which correspond to the receiver with CSI (*coherent* receiver) and receiver without CSI (*semi-coherent* receiver) respectively, is analyzed in the paper. The first receiver $\mathcal{R}_1$ is assumed to track CSI perfectly which means the fading components h_0 and h_1 are known at the receiver. However, the complexity in the estimation of CSI may preclude some of these energy-constrained devices from tracking the channel, which is the primary motivation behind considering receiver $\mathcal{R}_2$ for which coding techniques such as differential coding are needed at the transmitter side to enable it to estimate data without CSI. In the absence of CSI, a receiver would not be able to map the conditional distributions of the received signal to the true message bit, thereby resulting in a poor decoding performance. We will elaborate on this point further in Section 2.3.2. With the help of differential encoding, receiver $\mathcal{R}_2$ will decode data bits by observing the change in two consecutive symbols rather from absolute values, thereby improving the BER performance of the receiver compared to an uncoded transmission.

The coherent receiver in this work does not require the complete phase tracking of the channel gain that is generally attributed to coherent receivers in the literature. It should be noted that there are multiple interpretations of the terms *coherent* and *non-coherent* in the communication literature. In the conventional sense, coherent detection is used to refer to the communication systems which require phase tracking to synchronize the local carrier with that of the received signal. On the other hand, with respect to wireless communication systems, coherent detection is used to represent the tracking of the phase offset due to mainly multi-path propagation (and also local carrier offset) and mobility of the devices. This is because, generally, the local carrier estimation does not require frequent tracking while the channel state information (CSI) requires regular updates. Therefore, in the latter systems, coherent detection corresponds to systems that require CSI even partial knowledge such as magnitude of the channel gain coefficients, while non-coherent detection corresponds to systems that do not assume any knowledge of the CSI. (Note that even for non-coherent detection, assumptions are made about the statistics of the CSI like the PDF of the channel gain etc.) This is the interpretation that we followed in our work. Additionally, for semi-coherent detection, we do not directly estimate even the partial channel knowledge since we only require the joint information of the different channel gains to evaluate the threshold value. (Recall that the receiver in ambient backscatter perceives different channel gains due to on-off keying (OOK) modulation for different values of the backscatter data bit.)

Before going into further technical discussion, we define some key functional forms that

will be used throughout this paper.

Definition 2.2. The PDF of central chi-squared random variable $\chi^2(k)$ with degree k is given by:

$$f_{\chi^2}(x;k) = \begin{cases} \dfrac{x^{(\frac{k}{2}-1)}e^{-\frac{x}{2}}}{2^{\frac{k}{2}}\Gamma(\frac{k}{2})}, & x > 0, \\ 0, & \text{otherwise.} \end{cases} \tag{2.5}$$

Definition 2.3. The PDF of Rayleigh random variable with variance σ^2 of corresponding zero mean complex Gaussian RV is given by:

$$f_{\text{Ray}}(x;\sigma^2) = \begin{cases} \dfrac{2x}{\sigma^2}\exp\Big(-\dfrac{x^2}{\sigma^2}\Big), & x > 0, \\ 0, & \text{otherwise.} \end{cases} \tag{2.6}$$

Definition 2.4. The modified Bessel function of the first kind with order v is given by the expression:

$$I_v(z) = (\frac{z}{2})^v \sum_{i=0}^{\infty} \frac{(\frac{z^2}{4})^i}{i!\Gamma(v+i+1)}, \tag{2.7}$$

and the corresponding integral form when v is an integer n is given by:

$$I_n(z) = \frac{1}{\pi}\int_0^{\pi} e^{z\cos\theta}\cos(n\theta)\mathrm{d}\theta. \tag{2.8}$$

Definition 2.5. The modified Bessel function of the second kind with order v is given by the expression:

$$K_v(z) = \frac{\pi}{2}\frac{I_{-v}(z) - I_v(z)}{\sin v\pi}, \tag{2.9}$$

where $I_v(z)$ is the modified Bessel function of the first kind.

Definition 2.6. The generalized Marcum Q-function with degree M and parameters α, β [57] is given by the expression:

$$Q_M(\alpha,\beta) = \frac{1}{\alpha^{M-1}}\int_{\beta}^{\infty} v^M \exp\Big(-\frac{v^2+\alpha^2}{2}\Big) I_0(\alpha v)\,\mathrm{d}v. \tag{2.10}$$

2.3 Signal Detection

In this section, we first study the detection process at receiver $\mathcal{R}_1$ in detail, beginning with the derivation of conditional distributions of the average signal energy represented by random variable Y and the investigation of detection mechanisms to get the optimal detection threshold. We build on this analysis to study detection and error performance of receiver $\mathcal{R}_2$ focusing primarily on the elements differentiating the two receivers.

2.3.1 Receiver with CSI

Exact Distribution Functions

The BTx node will modulate its own data onto the reflected ambient radio waves which means that the Rx node has to implement a mechanism to separate backscatter data from the *ambient source* data. For this purpose, energy of the received signal is averaged over a window of N samples. This mechanism results in a random variable (RV) Y representing the average signal energy, and the operation is represented as follows [2]:

$$Y = \frac{1}{N}\sum_{n=1}^{N}|y(n)|^2 = \frac{1}{N}\sum_{n=1}^{N}|(h_r + \alpha h_b\ b\ h_t)x(n) + w(n)|^2. \tag{2.11}$$

This problem is formulated as a binary hypothesis testing problem where the scenarios conditioned on bits $b = 0$ and $b = 1$ are taken as $\mathcal{H}_0$ (Null Hypothesis) as $\mathcal{H}_1$ (Alternate Hypothesis) respectively:

$$\mathcal{H}_0 : Y = \frac{1}{N}\sum_{n=1}^{N}|h_0 x(n) + w(n)|^2, \qquad b = 0, \tag{2.12}$$

$$\mathcal{H}_1 : Y = \frac{1}{N}\sum_{n=1}^{N}|h_1 x(n) + w(n)|^2, \qquad b = 1. \tag{2.13}$$

The conditional probability density functions (PDFs) of Y are crucial in the detection and estimation of the transmitted bit and are derived in the following Lemma.

Lemma 2.7. *The PDFs of Y conditioned on $\mathcal{H}_0$, μ and $\mathcal{H}_1$, ν are respectively given by:*

$$f_{Y|\mathcal{H}_0,\mu}(t) = \frac{2N}{\sigma^2}\sum_{i=0}^{\infty}\frac{e^{-\frac{\mu N\bar{E}}{\sigma^2}}\left(\frac{\mu N\bar{E}}{\sigma^2}\right)^i}{i!}f_{\chi^2}(\frac{2N}{\sigma^2}t; 2N+2i), \tag{2.14}$$

$$f_{Y|\mathcal{H}_1,\nu}(t) = \frac{2N}{\sigma^2}\sum_{i=0}^{\infty}\frac{e^{-\frac{\nu N\bar{E}}{\sigma^2}}\left(\frac{\nu N\bar{E}}{\sigma^2}\right)^i}{i!}f_{\chi^2}(\frac{2N}{\sigma^2}t; 2N+2i). \tag{2.15}$$

Proof: See Appendix A.1. ■

Remark 2.8. It can be observed that the PDFs of Y conditioned on $\mathcal{H}_0$ and $\mathcal{H}_1$ are respectively dependent only on parameters μ and ν, which are the squares of absolute values of the respective channel coefficients h_0 and h_1. Thus, the average BER can be written as the expectation of BER conditioned jointly (since they are not independent) on just μ and ν.

Estimation of Channel Parameters

As highlighted in the remark 2.8 of the paper, the conditional PDFs of the average signal energy Y are only dependent on the absolute squares of the channel coefficients h_0 and h_1. Hence in this case, it is sufficient to estimate these *channel metrics* directly to perform the signal detection. Next we discuss a simple technique that could be easily implemented to estimate these channel metrics in the ambient backscatter communication systems.

Pilot signals are used in different wireless technologies to determine existence of carrier signals, perform carrier frequency or phase synchronization, and estimation of signal sampling time on the receiver end [58]. These signals carry little to no information and are already known at the receiver side. For example, Wi-Fi systems use pilot symbols known as *preamables* while LTE systems utilize special signals known as Primary Synchronization Signal (PSS) and Secondary Synchronization Signal (SSS) for detecting the carrier signals and estimating the carrier frequency and phase offsets. We assume a similar procedure where a stream of bits of value 0 followed by a stream of bits of value 1 are transmitted by the BTx at the beginning of a coherence period. The receiver will estimate the channel metrics using the similar energy averaging process and the metric for bit stream 0 can be estimated by taking mean value of Y which is given by:

$$\mathbb{E}[Y] = |h_0|^2\bar{E} + \sigma^2 \implies |h_0|^2 = \frac{\mathbb{E}[Y] - \sigma^2}{\bar{E}} \tag{2.16}$$

The other metric can be estimated through a similar procedure.

Comparison with Approximate Distribution Functions

The exact conditional PDFs derived here are compared with the approximations available in the literature. An alternate representation of Y can be derived by expanding (2.11) and is given by the expression:

$$Y = \frac{1}{N}\sum_{n=1}^{N}|y(n)|^2 = \frac{1}{N}\sum_{n=1}^{N} y(n)y^*(n) \tag{2.17}$$

$$= |h_r + \alpha h_b h_t b|^2 \frac{1}{N}\sum_{n=1}^{N}|x(n)|^2 + \frac{2}{N}\,\mathrm{Re}\left\{(h_r + \alpha h_b h_t b)\sum_{n=1}^{N} x(n)w^*(n)\right\} + \frac{1}{N}\sum_{n=1}^{N}|w(n)|^2 \tag{2.18}$$

$$= \underbrace{|h_r + \alpha h_b h_t b|^2\bar{E}}_{\text{constant}} + \underbrace{\frac{2}{N}\,\mathrm{Re}\left\{(h_r + \alpha h_b h_t b)\sum_{n=1}^{N} x(n)w^*(n)\right\}}_{\text{Gaussian RV}} + \underbrace{\frac{1}{N}\sum_{n=1}^{N}|w(n)|^2}_{\text{Central-}\chi^2\text{ RV}}. \tag{2.19}$$

One Gaussian approximation of Y can be made by approximating the Central-χ^2 RV with its mean value. This approximation is equivalent to the approximation given for a

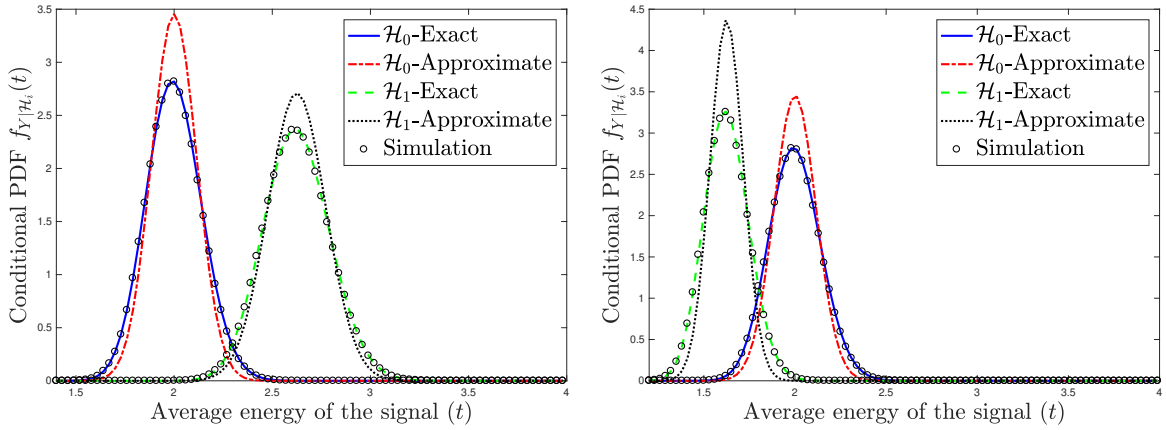

Figure 2.2: Comparison of exact (derived in this paper) and approximate conditional PDFs [1] of average signal energy Y for $\mu = 1, \nu = 1.625$ (left) and $\mu = 1, \nu = 0.625$ (right) at SNR $= 0$ dB, $N = 150$.

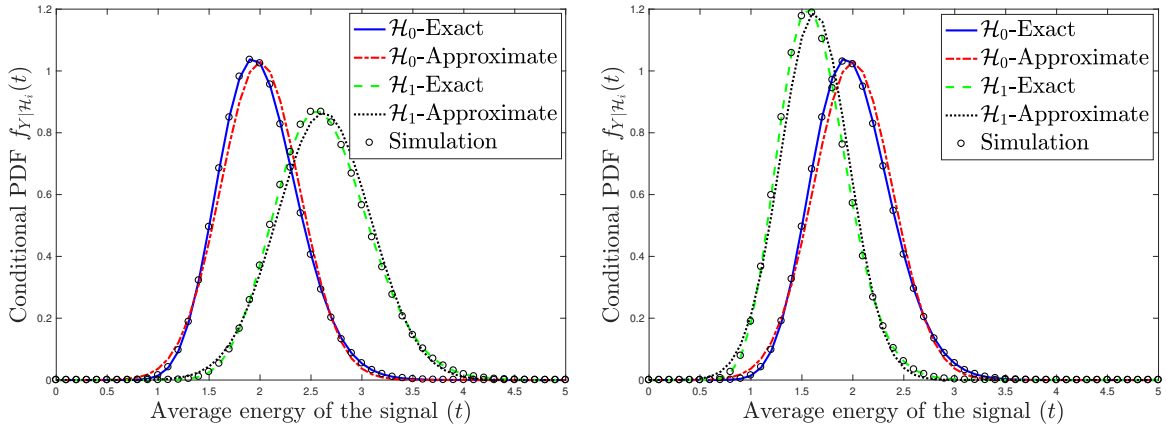

Figure 2.3: Comparison of exact and approximate conditional PDFs [1] of average signal energy Y for (a) $\mu = 1, \nu = 1.625$ (b) $\mu = 1, \nu = 0.625$ (SNR $= 0$ dB, $N = 20$).

large value of N in [1], which is also the preferred mode of approximation in the referenced paper. The exact and approximated conditional PDFs of the average signal energy Y for $N = 150$ and SNR = 0 dB are compared in Fig. 2.2, and the deviation in the plots is clearly noticeable. As expected, the exact distributions derived in this paper match exactly with the simulated conditional PDFs. On the other hand, the second Gaussian approximation of Y can be done by approximating the Central-χ^2 RV with a Gaussian RV of same mean and variance values. This approximation corresponds to the approximation given for a small value of N in [1]. The plots of the exact and approximated conditional PDFs in Fig. 2.3 show that the approximations work reasonably well. The reason for the deteriorating performance of the approximations in [1] with increasing value of N is due to the approximation of the aforementioned Central-χ^2 RV with its mean value at higher values of N which does not approximate the distribution properly. We observed that the approximation of this Central-χ^2 RV instead with Gaussian (also proposed in [1] for smaller N) works better for all values of N. From this point onward, the two approximations are referred to as the first and second Gaussian approximation of the conditional PDFs of Y.

The impact of channel variations on the conditional PDFs is analyzed by plotting them for the two sets of values of channel parameters μ and ν. When the two sub-plots in Figs. 2.2 and 2.3 are compared, the conditional distributions of two hypotheses are observed to interchange their positions which means that the relative positions of the conditional distributions of two hypotheses change with channel parameters μ and ν. Further, as the value of sample length N increases the conditional variance of Y decreases and this results in the concentration of the conditional PDFs. This effect can be observed in Figs. 2.2 and 2.3 by checking the difference in the supports over which the PDFs are mainly concentrated.

Detection Threshold

In the optimal detection of the standard BPSK modulation using MLT detection, the threshold value calculated as the intersection point of conditional likelihood functions has a tractable solution. However, the solution for the MLT estimation in an ambient backscatter system is intractable, and for this reason, we consider two other strategies called MT detection and approximate MLT detection along with the optimal MLT detection.

Mean Threshold (MT) Detection The threshold value of MT detection method is evaluated as the mean of the conditional expectations of average signal energy Y given $\mathcal{H}_0, \mu$ and $\mathcal{H}_1, \nu$:

$$T_{\text{mt}} = \frac{\mathbb{E}[Y|\mathcal{H}_0] + \mathbb{E}[Y|\mathcal{H}_1]}{2} = \sigma^2 + \frac{\bar{E}(\mu + \nu)}{2}. \tag{2.20}$$

Maximum Likelihood Threshold (MLT) Detection Here, we derive the expression of optimal threshold value for maximum likelihood detection. The representation of the

conditional PDFs of Y in terms of "sums of terms" as given in (2.14) and (2.15) can be modified to an alternate integral form using the modified Bessel function of first kind which is given for any integer order. Using this integral representation we can derive expression for the MLT, which unfortunately however does not have a tractable form. This result is presented in the following Lemma.

Lemma 2.9. *The optimal detection rule or threshold T_{mlt} (a function of μ and ν) is calculated by solving the expression given below:*

$$\begin{aligned}&\frac{N}{\sigma^2}e^{-\left(\frac{N}{\sigma^2}T_{\text{mlt}}+\frac{N\mu\bar{E}}{\sigma^2}\right)}\left(\frac{4T_{\text{mlt}}}{\mu\bar{E}}\right)^{\frac{N-1}{2}}I_{N-1}\left(\frac{2N}{\sigma^2}\sqrt{\mu\bar{E}T_{\text{mlt}}}\right)\\&=\frac{N}{\sigma^2}e^{-\left(\frac{N}{\sigma^2}T_{\text{mlt}}+\frac{N\nu\bar{E}}{\sigma^2}\right)}\left(\frac{4T_{\text{mlt}}}{\nu\bar{E}}\right)^{\frac{N-1}{2}}I_{N-1}\left(\frac{2N}{\sigma^2}\sqrt{\nu\bar{E}T_{\text{mlt}}}\right),\end{aligned}\tag{2.21}$$

and the expression can be simplified as follows:

$$e^{\frac{N}{\sigma^2}\bar{E}(\nu-\mu)}\left(\frac{\nu}{\mu}\right)^{\frac{N-1}{2}}\int_0^{\pi}e^{\frac{2N}{\sigma^2}\sqrt{\mu\bar{E}\,T_{\text{mlt}}}\cos\theta}\cos(N-1)\theta\,\mathrm{d}\theta=\int_0^{\pi}e^{\frac{2N}{\sigma^2}\sqrt{\nu\bar{E}\,T_{\text{mlt}}}\cos\theta}\cos(N-1)\theta\,\mathrm{d}\theta.\tag{2.22}$$

Proof: See Appendix A.2. ∎

Approximate MLT Detection As discussed above, solving (2.22) gives the optimal ML threshold value. The presence of T_{mlt}, the variable we are evaluating, inside the integral makes the problem highly intractable and the procedure is not so straightforward. To simplify the computations, we provide approximate solutions using Gaussian approximations of the conditional PDFs that we discussed earlier. We remind again that the selection of threshold value is an independent process from the characterization of signal distributions. The conditional distributions derived in subsection 2.3.1 are exact without any approximations as mentioned in the contributions of this paper. The approximations of the conditional distributions is only used for the derivation of tractable solutions to MLT to enable faster numerical computations. These approximate MLT thresholds are similar to the ones used in [1].

Lemma 2.10. *The approximate ML thresholds $T_{\text{mlt,app1}}$ and $T_{\text{mlt,app2}}$ for the two Gaussian approximations of conditional distributions of Y are given by the following expressions:*

$$T_{\text{mlt,app1}}=\sigma^2+\sqrt{\mu\nu\bar{E}\left(\frac{2\sigma^2}{N(\nu-\mu)}\ln\left(\frac{\nu}{\mu}\right)+\bar{E}\right)},\tag{2.23}$$

$$T_{\text{mlt,app2}}=\frac{\sigma^2}{2}+\sqrt{\frac{\sigma^4}{4}+\mu\nu\bar{E}^2+\frac{\mu+\nu}{2}\bar{E}\sigma^2+\frac{\left(2\mu\bar{E}+\sigma^2\right)}{2N}\frac{\left(2\nu\bar{E}+\sigma^2\right)\sigma^2}{(\nu-\mu)\bar{E}}\ln\left(\frac{2\nu\bar{E}+\sigma^2}{2\mu\bar{E}+\sigma^2}\right)}.\tag{2.24}$$

Proof: See Appendix A.3. ∎

2.3.2 Receiver without CSI

The assumption of CSI tracking at receiver $\mathcal{R}_1$ gave one the freedom to choose different evaluation strategies in estimating the threshold value. For energy-constrained devices like sensors, tracking a channel continuously may not be the ideal use of their energy and would be beneficial if detection mechanisms without (or partial) channel information can be implemented. By partial channel information, we mean that there is some measure of the channel like mean energy of the channel estimates. Additionally, energy constraints in some of the devices restrict the evaluation of complex numerical operations inhibiting the implementation of most of the threshold techniques. These are the primary factors motivating the pursuit of detection schemes in a receiver without (or partial) channel estimates which can result in reasonable performance.

The fading components in the binary hypothesis problem formulated earlier in (2.4) are observed to be different under each hypothesis. Both of the fading terms are complex and the magnitude of one component can be either smaller or bigger than the other component. As observed in the analysis related to conditional distributions, the conditional PDFs interchange positions with respect to the relative values of these components. Without information on the relative location of the conditional distributions of the two hypotheses, the threshold detector can incorrectly map the received average signal to a different hypothesis with high probability. To overcome the ambiguity of mapping correct conditional PDFs at receiver $\mathcal{R}_2$, differential encoding is implemented at the transmitter which reduces the complexity of the receiver *albeit* with a slight degradation in error performance [2]. Mathematically, the output of a differential encoding block is given by:

$$b(n) = b(n-1) \oplus m(n), \tag{2.25}$$

where $\oplus$ is the exclusive-or (XOR) operation, $b(n)$ is the transmitted bit at current time instant, $b(n-1)$ is the bit transmitted in previous time instant, and $m(n)$ is the message bit to be transmitted in the current time instant. At the receiver, $m(n)$ can be decoded with a similar XOR operation given by:

$$\hat{m}(n) = \hat{b}(n) \oplus \hat{b}(n-1), \tag{2.26}$$

where $\hat{b}(n)$ and $\hat{b}(n-1)$ are the symbols received at the current and previous time instants respectively. It can be observed that the information in differential encoding is encoded as a change rather than absolute values of the transmitted symbols, and in the differential decoding block at the receiver two consecutive symbols are used to detect each bit in the stream. Since the differential decoding takes in two consecutive symbols at a time, the value of fading coefficient is assumed to be the same over the two symbols (fairly reasonable assumption).

Threshold Strategies As there is no channel information at $\mathcal{R}_2$, we can only use threshold techniques which do not involve the explicit estimation of the channel state. This is where

the simplicity of evaluating the Mean threshold (MT) allows one to employ the technique for this receiver. The threshold of MT detection can be implemented in practice by averaging the energy of samples received over the first few time slots in the channel coherence period.

2.4 Bit Error Rate Analysis

In this section, we analyze the performance of the detection strategies by evaluating the BER expressions. The conditional BER expressions are also evaluated in terms of the generalized Marcum Q-function similar to the accepted representation of BER of the Gaussian distributed signals using the standard Q-function. This form of presentation of the conditional BER allows us to show the dependence of optimal BER performance on the SNR of the ambient signal which is demonstrated in the next subsection.

As noted in Remark 2.8, the average BER of an ambient backscatter system is dependent on joint distribution of the fading components μ and ν. The analytical expression of the average BER in a fading channel can be written as:

$$P_e = \mathbb{E}_{\mu,\nu}[P(e|\mu,\nu)] = \int_0^\infty \int_0^\infty f_{\mu,\nu}(\mu,\nu) P(e|\mu,\nu)\, \mathrm{d}\nu\, \mathrm{d}\mu, \tag{2.27}$$

where $f_{\mu,\nu}(\mu,\nu)$ is the joint probability density of fading components μ and ν, and $P(e|\mu,\nu)$ is the error probability conditioned on μ and ν. To the best of our understanding, existing works do not deal with the characterization of this joint probability density and hence the average BER analysis for this setup.

2.4.1 Conditional Error Probability

First, we derive the expressions of conditional error probabilities for receiver $\mathcal{R}_1$ and then extend the analysis to receiver $\mathcal{R}_2$. The conditional error probability $P(e|\mu,\nu)$ of a receiver is given by the expression:

$$P(e|\mu,\nu) = P(\mathcal{H}_0)P(e|\mathcal{H}_0,\mu) + P(\mathcal{H}_1)P(e|\mathcal{H}_1,\nu). \tag{2.28}$$

Assuming the symbols are equally likely, the prior probabilities of the two hypotheses are given by $P(\mathcal{H}_0) = P(\mathcal{H}_1) = \frac{1}{2}$. The conditional error probability of each hypothesis of receiver $\mathcal{R}_1$ is given by the following relation since the relative values of μ and ν change the relative positions of the conditional distribution curves:

$$P_{\mathcal{R}_1}(e|\mathcal{H}_0,\mu) = \begin{cases} \int_0^{T(\mu,\nu)} f_{Y|\mathcal{H}_0,\mu}(t)\, \mathrm{d}t, & \nu < \mu, \\ \int_{T(\mu,\nu)}^{\infty} f_{Y|\mathcal{H}_0,\mu}(t)\, \mathrm{d}t, & \nu \geq \mu. \end{cases} \quad P_{\mathcal{R}_1}(e|\mathcal{H}_1,\nu) = \begin{cases} \int_{T(\mu,\nu)}^{\infty} f_{Y|\mathcal{H}_1,\nu}(t)\, \mathrm{d}t, & \nu < \mu, \\ \int_0^{T(\mu,\nu)} f_{Y|\mathcal{H}_1,\nu}(t)\, \mathrm{d}t, & \nu \geq \mu. \end{cases} \tag{2.29}$$

When $\nu \geq \mu$, analytical expression of the conditional bit error rate is given by:

$$P^1_{\mathcal{R}_1}(e|\mu,\nu) = P(\mathcal{H}_0)P_{\mathcal{R}_1}(e|\mathcal{H}_0,\mu) + P(\mathcal{H}_1)P_{\mathcal{R}_1}(e|\mathcal{H}_1,\nu) \tag{2.30}$$

$$= \frac{1}{2}\int_T^\infty f_{Y|\mathcal{H}_0,\mu}(t)\,\mathrm{d}t + \frac{1}{2}\int_0^T f_{Y|\mathcal{H}_1,\nu}(t)\,\mathrm{d}t. \tag{2.31}$$

On the other hand for $\nu < \mu$, the conditional bit error rate is given by:

$$P^2_{\mathcal{R}_1}(e|\mu,\nu) = P(\mathcal{H}_0)P_{\mathcal{R}_1}(e|\mathcal{H}_0,\mu) + P(\mathcal{H}_1)P_{\mathcal{R}_1}(e|\mathcal{H}_1,\nu) \tag{2.32}$$

$$= \frac{1}{2}\int_0^T f_{Y|\mathcal{H}_0,\mu}(t)\,\mathrm{d}t + \frac{1}{2}\int_T^\infty f_{Y|\mathcal{H}_1,\nu}(t)\,\mathrm{d}t = 1 - P^1_{\mathcal{R}_1}(e|\mu,\nu). \tag{2.33}$$

The value of conditional BER is a function of the instantaneous values of parameters μ and ν and can take either $P_{\mathcal{R}_1}(e|\mu,\nu) = P^1_{\mathcal{R}_1}(e|\mu,\nu)$ or $P_{\mathcal{R}_1}(e|\mu,\nu) = P^2_{\mathcal{R}_1}(e|\mu,\nu)$ depending on the relative values of the two parameters. When differential encoding is implemented at transmitter for receiver $\mathcal{R}_2$, the conditional BER expression simplifies to a single expression. For the receiver $\mathcal{R}_2$, error is going to occur at the output of differential decoding when only one of the two consecutive bits of the received symbols flips. Also, observe that both of the detected bits are independent which simplifies the analysis, and we can write the expression of the conditional BER as follows:

$$\begin{aligned} P_{\mathcal{R}_2}(e|\mu,\nu) &= P(\hat{Y}_k \neq Y_k)P(\hat{Y}_{k-1} = Y_{k-1}) + P(\hat{Y}_k = Y_k)P(\hat{Y}_{k-1} \neq Y_{k-1}) \\ &= 2\,P(\hat{Y}_k \neq Y_k)P(\hat{Y}_{k-1} = Y_{k-1}) = 2\,P^1_{\mathcal{R}_1}(e|\mu,\nu)P^2_{\mathcal{R}_1}(e|\mu,\nu). \end{aligned} \tag{2.34}$$

The Marcum Q-function is extensively used as a cumulative distribution function for noncentral chi, noncentral chi-squared and Rice distributions and many algorithms for efficient evaluation of the function are implemented in hardware and software. Hence, it would be highly beneficial to give equivalent representations of the conditional BER in terms of Marcum Q-function.

The conditional error probabilities of the two receivers $\mathcal{R}_1$ and $\mathcal{R}_2$ of ambient backscatter systems in terms of the generalized Marcum Q-function can be expressed as [57, 59]:

$$P_{\mathcal{R}_1}(e|\mu,\nu) = \begin{cases} P^1_{\mathcal{R}_1}(e|\mu,\nu) & \nu < \mu, \\ P^2_{\mathcal{R}_1}(e|\mu,\nu) & \nu \geq \mu. \end{cases} = \begin{cases} \dfrac{1}{2}\left\{1 + Q_N\left(\sqrt{2N\dfrac{\mu\bar{E}}{\sigma^2}}, \sqrt{2N\dfrac{T(\mu,\nu)}{\sigma^2}}\right)\right. \\ \qquad \left. - Q_N\left(\sqrt{2N\dfrac{\nu\bar{E}}{\sigma^2}}, \sqrt{2N\dfrac{T(\mu,\nu)}{\sigma^2}}\right)\right\} \nu < \mu, \\ \dfrac{1}{2}\left\{1 + Q_N\left(\sqrt{2N\dfrac{\nu\bar{E}}{\sigma^2}}, \sqrt{2N\dfrac{T(\mu,\nu)}{\sigma^2}}\right)\right. \\ \qquad \left. - Q_N\left(\sqrt{2N\dfrac{\mu\bar{E}}{\sigma^2}}, \sqrt{2N\dfrac{T(\mu,\nu)}{\sigma^2}}\right)\right\} \nu \geq \mu. \end{cases} \tag{2.35}$$

$$P_{\mathcal{R}_2}(e|\mu,\nu) = 2P^1_{\mathcal{R}_1}(e|\mu,\nu)P^2_{\mathcal{R}_1}(e|\mu,\nu)$$
$$= \frac{1}{2} - \frac{1}{2}\left\{Q_N\left(\sqrt{2N\frac{\nu\bar{E}}{\sigma^2}}, \sqrt{2N\frac{T(\mu,\nu)}{\sigma^2}}\right) - Q_N\left(\sqrt{2N\frac{\mu\bar{E}}{\sigma^2}}, \sqrt{2N\frac{T(\mu,\nu)}{\sigma^2}}\right)\right\}^2. \tag{2.36}$$

Remark 2.11. We can observe from (2.35) and (2.36) that the conditional BER expressions are functions of the parameters N, $\frac{\mu\bar{E}}{\sigma^2}$, $\frac{\nu\bar{E}}{\sigma^2}$ and $\frac{T(\mu,\nu)}{\sigma^2}$. The fractions $\frac{T(\mu,\nu)}{\sigma^2}$ for the MT threshold and the two approximate MLTs threshold techniques can be modified as:

$$\frac{T_{\text{mt}}}{\sigma^2} = 1 + \frac{\frac{\mu\bar{E}}{\sigma^2} + \frac{\nu\bar{E}}{\sigma^2}}{2}, \tag{2.37}$$

$$\frac{T_{\text{mlt,app1}}}{\sigma^2} = 1 + \sqrt{\frac{\nu\bar{E}}{\sigma^2}\left(\frac{2\frac{\mu\bar{E}}{\sigma^2}}{N\left(\frac{\nu\bar{E}}{\sigma^2} - \frac{\mu\bar{E}}{\sigma^2}\right)}\ln\left(\frac{\frac{\nu\bar{E}}{\sigma^2}}{\frac{\mu\bar{E}}{\sigma^2}}\right) + \frac{\mu\bar{E}}{\sigma^2}\right)}, \tag{2.38}$$

$$\frac{T_{\text{mlt,app2}}}{\sigma^2} = \frac{1}{2} + \sqrt{\frac{1}{4} + \frac{\nu\bar{E}}{\sigma^2}\frac{\mu\bar{E}}{\sigma^2} + \frac{\frac{\mu\bar{E}}{\sigma^2} + \frac{\nu\bar{E}}{\sigma^2}}{2} + \frac{\left(\frac{2\mu\bar{E}}{\sigma^2}+1\right)\left(\frac{2\nu\bar{E}}{\sigma^2}+1\right)}{2N\left(\frac{\nu\bar{E}}{\sigma^2} - \frac{\mu\bar{E}}{\sigma^2}\right)}\ln\left(\frac{\frac{2\nu\bar{E}}{\sigma^2}+1}{\frac{2\mu\bar{E}}{\sigma^2}+1}\right)}, \tag{2.39}$$

which are functions of the other three parameters N, $\frac{\mu\bar{E}}{\sigma^2}$ and $\frac{\nu\bar{E}}{\sigma^2}$.

Even though MLT technique does not have a closed form expression for the threshold, we show that the solution $\frac{T_{\text{mlt}}}{\sigma^2}$ of (2.22) has to be a function of the same three parameters. The rearranged form of (2.22) given below is a function of the three parameters N, $\frac{\mu\bar{E}}{\sigma^2}$ and $\frac{\nu\bar{E}}{\sigma^2}$ and hence, the solution $\frac{T_{\text{mlt}}}{\sigma^2}$ of the equation would also be a function of the three parameters.

$$e^{N\left(\frac{\nu\bar{E}}{\sigma^2} - \frac{\mu\bar{E}}{\sigma^2}\right)}\left|\frac{\frac{\nu\bar{E}}{\sigma^2}}{\frac{\mu\bar{E}}{\sigma^2}}\right|^{\frac{N-1}{2}}\int_0^\pi e^{2N\sqrt{\frac{\mu\bar{E}}{\sigma^2}\frac{T_{\text{mlt}}}{\sigma^2}}\cos\theta}\cos(N-1)\theta\,\mathrm{d}\theta = \int_0^\pi e^{2N\sqrt{\frac{\nu\bar{E}}{\sigma^2}\frac{T_{\text{mlt}}}{\sigma^2}}\cos\theta}\cos(N-1)\theta\,\mathrm{d}\theta. \tag{2.40}$$

The fractions $\frac{\mu\bar{E}}{\sigma^2}$ and $\frac{\nu\bar{E}}{\sigma^2}$ are the received SNRs under the two hypotheses. Hence, it can be concluded that the conditional BER of the MT, approximate MLTs and the optimal MLT threshold mechanisms depend upon the signal and noise strengths through SNR and not their respective energies separately.

2.4.2 Average Error Probability

The second component required in the average BER expression is the joint distribution function of fading components μ and ν, which is derived in the following Lemma.

Lemma 2.12. *The joint density of the fading components μ and ν is given by the following expression:*

$$f_{\mu,\nu}(\mu,\nu) = \frac{2}{\pi\sigma_{h_1}^2} e^{-\frac{\mu}{\sigma_{h_1}^2}} \frac{1}{|\alpha|^2\sigma_{h_1}^2\sigma_{h_2}^2} \int_0^{\pi} K_0\left(\frac{\sqrt{\mu+\nu-2\sqrt{\mu\nu}\cos\theta}}{\frac{|\alpha|\sigma_{h_1}\sigma_{h_2}}{2}}\right) \mathrm{d}\theta. \tag{2.41}$$

where $K_0(z)$ is the zeroth order modified Bessel function of second kind.

Proof: See Appendix A.4. ∎

We can now provide the final result of the paper which quantifies the error performance of ambient backscatter systems in terms of the average BER. The following theorem gives the final average BER expressions for both receivers $\mathcal{R}_1$ and $\mathcal{R}_2$ in the ambient backscatter systems.

Theorem 2.13. *The average BER of the receivers $\mathcal{R}_1$ (with CSI) and $\mathcal{R}_2$ (without CSI) in an ambient backscatter system are given by (2.45) and (2.46) respectively and $T(\mu,\nu)$ in the equations represents the threshold value which depends on the employed detection strategy.*

Proof: Using the definition of average BER in (2.27) of an ambient backscatter system, the equivalent expression for receiver $\mathcal{R}_1$ is given by:

$$P_{\mathcal{R}_1}(e) = \int_0^{\infty}\int_0^{\infty} f_{\mu,\nu}(\mu,\nu) P_{\mathcal{R}_1}(e|\mu,\nu)\,\mathrm{d}\nu\,\mathrm{d}\mu \tag{2.42}$$

$$\overset{(a)}{=} \int_0^{\infty}\int_0^{\mu} f_{\mu,\nu}(\mu,\nu) P^1_{\mathcal{R}_1}(e|\mu,\nu)\,\mathrm{d}\nu\,\mathrm{d}\mu + \int_0^{\infty}\int_{\mu}^{\infty} f_{\mu,\nu}(\mu,\nu) P^2_{\mathcal{R}_1}(e|\mu,\nu)\,\mathrm{d}\nu\,\mathrm{d}\mu, \tag{2.43}$$

where (a) follows from the piece-wise expressions of $P_{\mathcal{R}_1}(e|\mu,\nu)$ for the disjoint sets $\nu<\mu$ and $\nu\geq\mu$. By substituting the expressions of $P^1_{\mathcal{R}_1}(e|\mu,\nu)$ and $P^2_{\mathcal{R}_1}(e|\mu,\nu)$ provided in (2.35) and $f_{\mu,\nu}(\mu,\nu)$ provided in (2.41), we get the result given in the theorem.

Similarly, the average BER expression for receiver $\mathcal{R}_2$ is given by:

$$P_{\mathcal{R}_2}(e) = \int_0^{\infty}\int_0^{\infty} f_{\mu,\nu}(\mu,\nu) P_{\mathcal{R}_2}(e|\mu,\nu)\,\mathrm{d}\nu\,\mathrm{d}\mu. \tag{2.44}$$

Substituting the expressions of $P_{\mathcal{R}_2}(e|\mu,\nu)$ and $f_{\mu,\nu}(\mu,\nu)$ given in (2.36) and (2.41) respectively, we get the result. ∎

$$
\begin{aligned}
&P_{\mathcal{R}_1}(e) \\
&= \frac{1}{2} + \int_{\mu=0}^{\infty}\int_{\nu=0}^{\mu} \frac{2}{\pi\sigma_{h_1}^2} e^{-\frac{\mu}{\sigma_{h_1}^2}} \frac{1}{|\alpha|^2\sigma_{h_1}^2\sigma_{h_2}^2} \int_0^{\pi} K_0\left(\frac{\sqrt{\mu+\nu-2\sqrt{\mu\nu}\cos\theta}}{\frac{|\alpha|\sigma_{h_1}\sigma_{h_2}}{2}}\right) \mathrm{d}\theta \\
&\quad \times \frac{1}{2}\left\{ Q_N\left(\sqrt{2N\frac{\mu\bar{E}}{\sigma^2}}, \sqrt{2N\frac{T(\mu,\nu)}{\sigma^2}}\right) - Q_N\left(\sqrt{2N\frac{\nu\bar{E}}{\sigma^2}}, \sqrt{2N\frac{T(\mu,\nu)}{\sigma^2}}\right) \right\} \mathrm{d}\nu\,\mathrm{d}\mu \\
&\quad + \int_{\mu=0}^{\infty}\int_{\nu=\mu}^{\infty} \frac{2}{\pi\sigma_{h_1}^2} e^{-\frac{\mu}{\sigma_{h_1}^2}} \frac{1}{|\alpha|^2\sigma_{h_1}^2\sigma_{h_2}^2} \int_0^{\pi} K_0\left(\frac{\sqrt{\mu+\nu-2\sqrt{\mu\nu}\cos\theta}}{\frac{|\alpha|\sigma_{h_1}\sigma_{h_2}}{2}}\right) \mathrm{d}\theta \\
&\quad \times \frac{1}{2}\left\{ Q_N\left(\sqrt{2N\frac{\nu\bar{E}}{\sigma^2}}, \sqrt{2N\frac{T(\mu,\nu)}{\sigma^2}}\right) - Q_N\left(\sqrt{2N\frac{\mu\bar{E}}{\sigma^2}}, \sqrt{2N\frac{T(\mu,\nu)}{\sigma^2}}\right) \right\} \mathrm{d}\nu\,\mathrm{d}\mu,
\end{aligned}
\tag{2.45}
$$

$$
\begin{aligned}
P_{\mathcal{R}_2}(e) &= \int_{\mu=0}^{\infty}\int_{\nu=0}^{\infty} \frac{2}{\pi\sigma_{h_1}^2} e^{-\frac{\mu}{\sigma_{h_1}^2}} \frac{1}{|\alpha|^2\sigma_{h_1}^2\sigma_{h_2}^2} \int_0^{\pi} K_0\left(\frac{\sqrt{\mu+\nu-2\sqrt{\mu\nu}\cos\theta}}{\frac{|\alpha|\sigma_{h_1}\sigma_{h_2}}{2}}\right) \mathrm{d}\theta \\
&\quad \times \left(\frac{1}{2} - \frac{1}{2}\left\{ Q_N\left(\sqrt{2N\frac{\nu\bar{E}}{\sigma^2}}, \sqrt{2N\frac{T(\mu,\nu)}{\sigma^2}}\right) - Q_N\left(\sqrt{2N\frac{\mu\bar{E}}{\sigma^2}}, \sqrt{2N\frac{T(\mu,\nu)}{\sigma^2}}\right) \right\}^2 \right) \mathrm{d}\nu\,\mathrm{d}\mu,
\end{aligned}
\tag{2.46}
$$

Remark 2.14. While the procedure used for the derivation of the conditional PDFs in 2.7 can be easily extended to a higher order modulation scheme, the approach used in the derivation of the conditional BER and the average BER cannot be directly extended to an M-ary modulation scheme. One often has to resort to bounds, for example using the union bound, which are carefully constructed based on the constellation structure of the M-ary scheme of interest (e.g., using the nearest neighbor distances between constellation points). In this energy based detection of ambient backscatter, the relative positions of the points in the constellation change depending on the relative values of the channel coefficients, which may result in intractable piece-wise expressions. As a result, the formal treatment of M-ary modulation schemes in this setup is left as a promising direction for future work.

Remark 2.15. From the system equation in (2.1), we can see that the received signal has a direct component from the ambient source that does not contain any data. We can interpret that as an *interfering signal* to the backscatter signal, which might act as a bottleneck to the BER performance of the system. We answer this here by analytically showing the exact impact of the direct link on BER.

The conditional PDF of the average received energy Y can be closely approximated using the second Gaussian approximation. That means one can evaluate the conditional BER

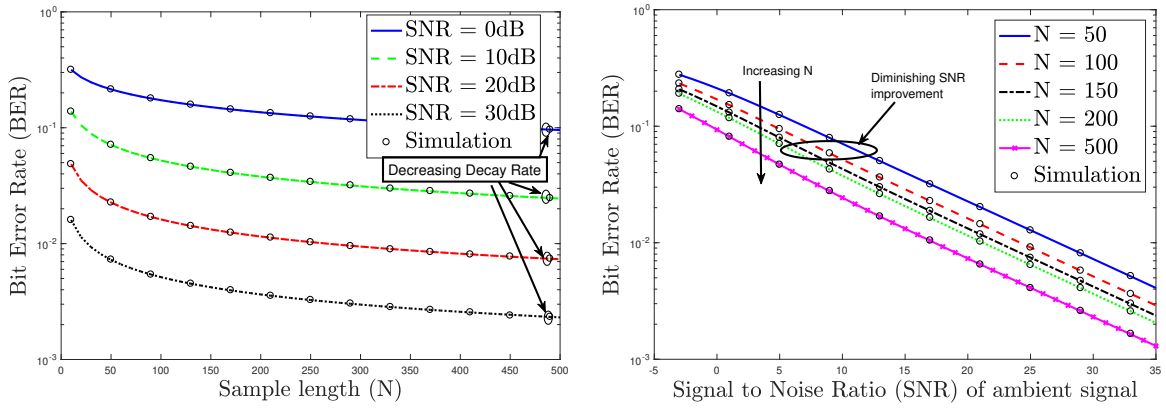

(a) (b)

Figure 2.4: Performance comparison in MT technique: (a) BER vs N for different SNR, (b) BER vs SNR for different N.

using the Q-function instead of the generalized Marcum-Q function. Making the assumption $\sigma^4 \ll 1$ at high SNR, the conditional BER of an ambient backscatter system using the MT threshold can be approximated as:

$$P_{\mathcal{R}_1}(e|\mu,\nu) = \begin{cases} \frac{1}{2} + \frac{1}{2}\left\{ Q\left(\frac{\left(\sqrt{\mu}+\sqrt{\nu}\right)\left(\sqrt{\frac{\mu}{\nu}}-1\right)}{2\sqrt{2N}} \sqrt{\frac{\bar{E}}{\sigma^2}} \right) - Q\left(\frac{\left(\sqrt{\mu}+\sqrt{\nu}\right)\left(\sqrt{\frac{\nu}{\mu}}-1\right)}{2\sqrt{2N}} \sqrt{\frac{\bar{E}}{\sigma^2}} \right) \right\} & \nu < \mu, \\ \frac{1}{2} + \frac{1}{2}\left\{ Q\left(\frac{\left(\sqrt{\mu}+\sqrt{\nu}\right)\left(\sqrt{\frac{\nu}{\mu}}-1\right)}{2\sqrt{2N}} \sqrt{\frac{\bar{E}}{\sigma^2}} \right) - Q\left(\frac{\left(\sqrt{\mu}+\sqrt{\nu}\right)\left(\sqrt{\frac{\mu}{\nu}}-1\right)}{2\sqrt{2N}} \sqrt{\frac{\bar{E}}{\sigma^2}} \right) \right\} & \nu \geq \mu. \end{cases} \tag{2.47}$$

The input to the first and second Q-functions in the two expressions of (2.47) are of positive and negative values respectively, meaning the relative values of parameters μ and ν result in an asymptotic conditional BER of value 0 when the SNR tends to infinity. However, since the first Q-function is positive at smaller SNR, the obvious way of improving the conditional BER is to completely remove the positive term in (2.47) which is to set $\mu = 0$. This essentially means that the conditional BER can always be improved if the direct path from the power source at the receiver is removed. We have shown this observation for receiver $\mathcal{R}_1$ (with CSI) but the same analysis can be applied to receiver $\mathcal{R}_2$ (without CSI).

2.5 Numerical Results and Discussion

In this section, we plot the analytical results derived in the previous section to obtain useful system design insights. The analytical results are also validated by comparing with Monte Carlo simulations. The reflection coefficient α is set appropriately to approximate the 1.1 dB signal attenuation mentioned in [3] and the variances $\sigma^2_{h_1}$ and $\sigma^2_{h_2}$ of fading links is set to 1 for the performance evaluation. First, the results of receiver $\mathcal{R}_1$ (with CSI) are

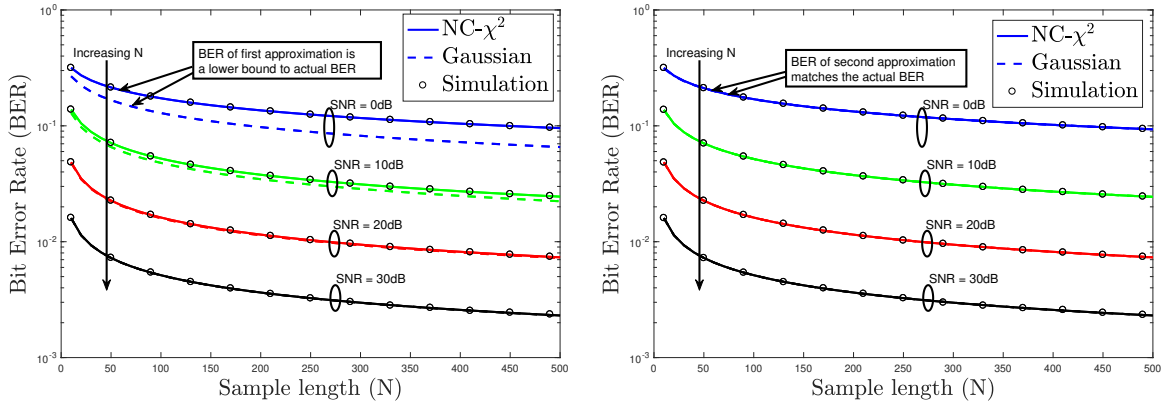

Figure 2.5: BER comparisons of actual and Gaussian approximated distributions for different SNR values using approximate ML threshold: (a) Actual vs first approximation, (b) Actual vs second approximation.

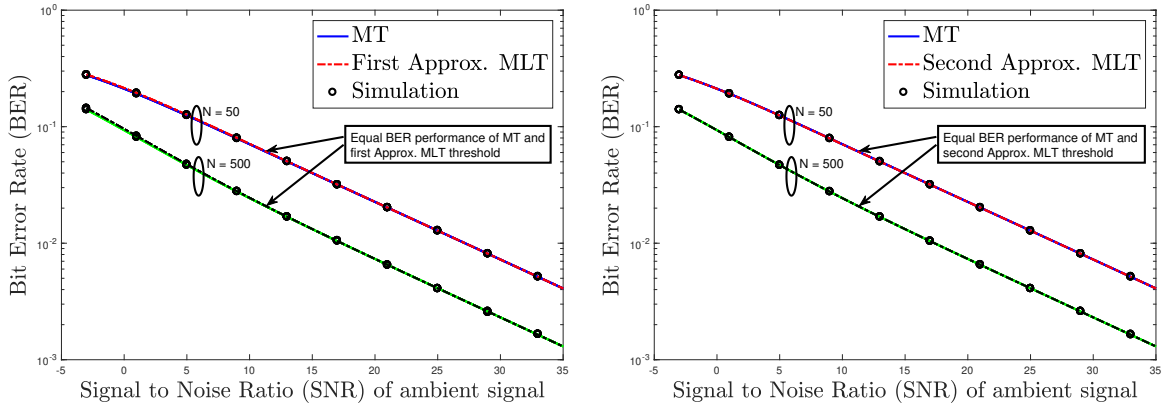

Figure 2.6: Performance comparison of the two Approximate MLTs and MT at different values of N: (a) BER versus SNR for first approximate MLT and MT thresholds, (b) BER versus SNR for second approximate MLT and MT thresholds.

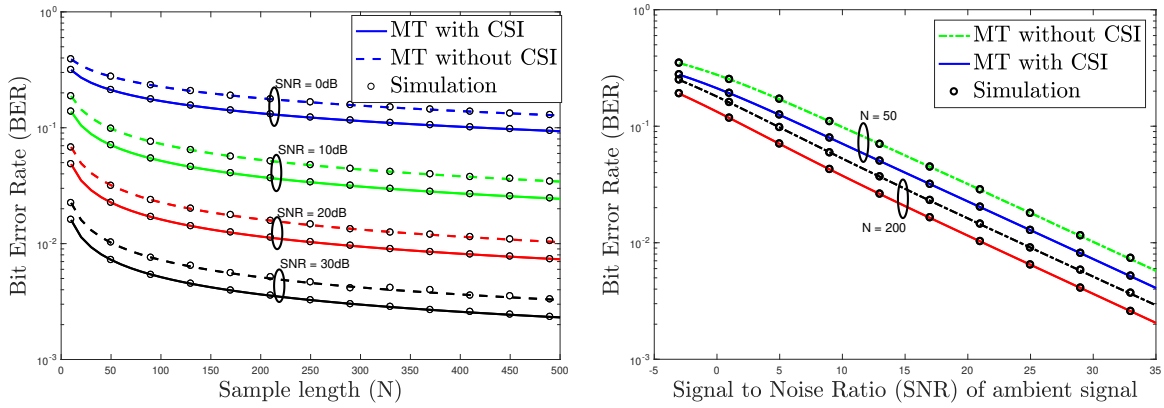

Figure 2.7: Performance comparison of Receiver with CSI and Receiver without CSI in MT technique: (a) BER vs N, (b) BER vs SNR.

presented before moving to receiver $\mathcal{R}_2$ (without CSI). With respect to any given system parameter, we refer to *decay rate* as the rate of decrement in BER with the increasing value of that parameter. In Fig. 2.4a, we present the BER as a function of sample length N for different SNR values. It can be observed that the decay rate decreases with respect to N. A similar comparison is shown in Fig. 2.4b by plotting BER against SNR for different values of N. The gain in SNR of the system has diminishing returns with increasing N as the performance of the energy averaging operation at the receiver converges to a limit, thereby limiting the improvement in BER.

The difference in BER accuracy when using the approximated distributions instead of the exact distribution are compared in Figs. 2.5a and 2.5b. The first Gaussian approximation does not result in accurate BER at the lower SNR range as shown in Fig. 2.5a. The tightness of this approximation improves with increasing SNR. Further as shown in Fig. 2.5b, the second Gaussian approximation results in BER that is very accurate with respect to actual BER given by the exact distributions. For this reason, it can be concluded that the second Gaussian approximation should be the preferred mode of approximation out of the two at all values of N.

We now compare the BER performance of the threshold techniques MT and the two approximate MLTs. In particular, Figs. 2.6a and 2.6b depict the performance of the first approximate MLT and the second approximate MLT respectively compared to MT, from which we can conclude that both the approximate MLT techniques give similar BER performance as the MT technique. Hence, MT technique could be preferred due to the ease of implementation in either of the two receivers $\mathcal{R}_1$ and $\mathcal{R}_2$.

The performance of the two receivers $\mathcal{R}_1$ and $\mathcal{R}_2$ is compared in Figs. 2.7a and 2.7b. As expected in the case of differential encoding, the performance of $\mathcal{R}_2$ is 3 dB worse than

that of $\mathcal{R}_1$. The final insight from the analysis is that the BER of the optimal MT and other threshold techniques is dependent only on the received SNRs of the signal and not on the individual signal and noise energies. The technical discussion of this final insight is already presented in Remark 2.11.

Some of the existing literature, both experimental and theoretical studies, have also looked at the BER performance characterization of the ambient backscatter systems which can be used to compare with the BER results obtained in our work. This discussion is very much applicable to the upcoming chapters but is limited to the current chapter to avoid repetition. The experimental studies have shown that the operational BER of 0.01 can be achieved at a distance of 27 m in ambient backscatter even at very low transmit power of 0 dBm using coding and multiple antennas techniques [60]. Similarly, the general BER values observed for theoretical studies are in the range of 0.01 for SNR of 30 dB [1, 13]. As shown here (and will also be shown in the upcoming chapters), the BER results obtained in our studies are consistent with these observations. In fact, this dissertation has performed a comprehensive analysis to determine under what scenarios will the BER go below the operational value of 0.01, and have come up with efficient techniques to improve the BER performance of the ambient backscatter systems.

2.6 Summary

In this paper, the error performance of an ambient backscatter system in a flat Rayleigh fading channel is characterized by deriving the exact analytical expressions of average BER both for the receivers with and without CSI. As part of the BER analysis, the exact conditional distributions of the average energy of the received signal is characterized in terms of the noncentral chi-squared distribution. The analysis requires careful treatment of the joint distribution of correlated fading components that appear in the two hypotheses in the BER derivation. Several key insights are drawn from the aforementioned analyses. First, the optimal BER of the ambient backscatter system is dependent on the energies of the signal and noise through SNR and not separately on the individual energies. Second, increasing the sample length N provides diminishing returns in terms of BER improvement.

This work has numerous extensions. The power sources of ambient backscatter systems are not exactly stable and a nice extension to our work would be to incorporate this instability in the BER analysis. Second, the error analysis performed in this work is applicable only for slow varying channels. It is therefore important to extend it to fast fading scenarios as well. Third, in this work, we focused on the error performance of an isolated link. It is worthwhile to investigate if interference will have any noticeable impact on the BER in a dense IoT deployment. This analysis can perhaps be performed using tools from stochastic geometry. In the coming chapters, we consider the problem of symbol detection in time-selective channels which necessitate the investigation into the performance analysis of non-coherent receivers.

Chapter 3

Bit Error Rate of Non-Coherent Ambient Backscatter in Time-Selective Fading

3.1 Introduction

In the previous chapter, we studied the problem of coherent and semi-coherent detection for ambient backscatter which are more relevant for a slow varying channel. In this chapter, we investigate non-coherent detection in ambient backscatter motivated by the problem of communication in a fast varying channel. In particular, given the diverse nature of applications envisioned in the Internet-of-Things (IoT) ecosystem, the channel conditions experienced by the IoT devices across different applications could vary significantly [61]. In the context of this work, the channel coherence time experienced by these devices could vary by orders of magnitude across applications. For instance, IoT devices deployed in high mobility scenarios, such as vehicles, road signs, or traffic posts, are expected to experience higher Doppler spread, and hence lower channel coherence time, compared to the IoT devices deployed in relatively static scenarios, such as homes, offices, and public places. While the latter case has implicitly been the focus of most of the prior work on ambient backscatter communication systems, the former is equally, if not more, important but has received much less attention. Most notably, lower coherence time makes it difficult to implement channel estimation and tracking procedure using either training or blind estimation. Because of this, one needs to consider non-coherent detection schemes for such scenarios, which have not yet been investigated in the context of ambient backscatter communications. Motivated by this knowledge gap, this work focuses on receiver design and comprehensive performance characterization of non-coherent detection-based ambient backscatter system under time-selective fading channels.

3.1.1 Related Work

As noted above, the existing literature on ambient backscatter is mainly focused on the slow fading channels that assume a block fading model [1,12–20,62–68]. Maximum-likelihood (ML) detection under an ambient backscatter setup was first investigated in [12]. The signal detection under non-coherent and semi-coherent setups is analyzed in [1,12–16,18]. The signal detection at a multiple antenna receiver is studied in [16] and the statistical-covariance

based detection is explored in [18]. While [6]-[12] were based on the Gaussian distribution approximation for the conditional distributions of the average energy of the received signal, the exact bit error rate (BER) analysis for the slow fading case was performed in [5]. Interested readers can also refer to [5] for a detailed overview of the backscatter concept. Ambient backscatter communication using orthogonal frequency division multiplexing (OFDM) is investigated in [19,62]. On the same lines, [17,63] explored new coding schemes, such as Manchester coding, to improve detection performance. Some of the existing literature that have worked on reducing the affect of the direct link (DL) interference in ambient backscatter are [19, 52, 62, 69]. In [52], a multiple antenna prototype is developed which overcomes the affect of DL interference by estimating the channel using the preamble bits of Wi-Fi. In [19], the repetitive pattern of the data in OFDM, due to the use of cyclic prefix, is exploited to cancel the DL interference. Meanwhile, [62] has designed a non-coherent detector which totally avoids the DL interference by utilizing the null sub-carriers in OFDM. In [69], an analog-digital hybrid beamformer receiver, that designs the optimal beamforming vector using the angle-of-arrival (AoA) of the DL, is proposed for a deterministic line-of-sight (LOS) channel. However, these works [19, 52, 62, 69] consider a block fading channel and none of them have jointly investigated non-coherent detection and time-selective fading which distinguishes our work.

A general requirement of coherent detection is the transmission of pilot/training symbols from transmitter to receiver nodes for the estimation of channel state information (CSI). This will require some form of cooperation between the primary and backscatter network nodes which might not always be possible. Hence, alternate approaches that avoid the transmission of pilots, such as blind channel estimation techniques, have also been investigated for ambient backscatter [64–68]. These approaches use different techniques from Bayesian statistics such as expectation-maximization (EM) or space alternating generalized expectation-maximization (SAGE) to iteratively implement the maximum *a posteriori* probability (MAP) or ML methods to perform the channel estimation from the received signal directly. The performance of these techniques depends on the accuracy and the convergence rate of the blind channel estimation procedures. Therefore, if the convergence rate is slow, these techniques might not be suitable for implementation in a time-selective fading channel. We overcome this drawback by investigating a non-coherent detection technique that only requires estimating large-scale parameters.

3.1.2 Contributions

To the best of our knowledge, this is the first work that presents a comprehensive analytical treatment of non-coherent detection in ambient backscatter under time-selective fading channels. The time-selective fading channel is modeled using a first-order AR process, and for this setup a binary hypothesis testing problem is formulated to investigate the BER performance of the two following receivers: 1) single-antenna (SA) receiver, and 2) multi-antenna (MA) receiver.

New Receiver Architecture The receiver architecture used in the prior studies of ambient backscatter requires the computation of the test statistic (TS) based on the average energy of the received signal samples. In our work, we consider a different receiver architecture based on the direct averaging of the received signal samples which requires lesser number of operations, thereby reducing the complexity. Besides, it is more tractable compared to the conventional architecture as derivations for the optimal detection strategies in that detector are not easy [20]. In addition, due to the exclusive linear operations in the new architecture, the receiver is shown to be resilient to synchronization and timing errors. By deriving BER for the non-coherent setup, we concretely demonstrate that while the new architecture is inadequate for an SA receiver, it has good BER performance when used in conjunction with a MA receiver, which is attributed to the elimination of the strong interference generated by the DL from the power source. The novelty of the MA receiver designed here lies in its ability to exploit the fact that the time-scale over which AoA varies is much larger than the time-scale over which the overall channel gain varies and use it for tracking the AoA of the DL. As implied already, the new receiver architecture also results in tractable conditional distributions, which facilitates the derivation of the optimal detection strategy and the evaluation of the exact BER.

Asymptotic Growth Rate of a Generalized Sum Sequence In the process of deriving conditional distributions, we come across a sum sequence with correlation across samples. We investigate the asymptotic growth rate of this sum sequence and use it to derive a new concentration result for another specific sequence of interest. This contribution is central to the evaluation of the exact asymptotic conditional distributions and to the subsequent BER analysis.

Insights Our analysis has shown that the SA receiver quickly reaches a BER floor due to the strong interference resulting from the DL of the ambient power source. The performance is shown to improve drastically after canceling this interference, which is achieved by tracking the AoA of the DL using the MA receiver. Further, with multiple antennas it is possible to achieve antenna gain, including an additional angular resolution when the the number of receive antennas are increased beyond two. This improvement in angular resolution plays an important role in applications where the AoAs of the DL and backscatter link (BL) are similar. The BER with the new receiver architecture is shown to be independent of the signal sample-size of the averaging operation for some cases, such as zero expected value of the ambient data sequence and/or uncorrelated time-domain fading. For the more general case of correlated fading, the BER is observed to improve with increasing time-domain correlation of the fading. Due to the diminishing returns in the improvement of BER with increasing sample size, the BER initially decreases and then reaches an asymptotic value. In addition, the first-order auto-regressive (AR) process is shown to be a good approximation of the reference models available for the time-selective fading channels by comparing their BER performance under different scenarios.

3.2 System Model

3.2.1 System Setup and Channel Model

The backscatter system in our current setup has three devices: ambient power source (PS), backscatter transmitter (BTx), and receiver (Rx), as illustrated in Fig. 3.1. The channel considered in the work is flat Rayleigh faded whose coherence time is of the order of duration of each ambient symbol, with spatial correlation at the Rx. The received signal contains two elements, the DL coming from the ambient PS, and the BL reflected from the BTx, with their respective AoAs given by θ_1 and θ_2. Both the PS and BTx can be in motion, due to which the channel gain of the three links (including the link from PS to BTx) will be changing with time. As shown in [9], ambient backscatter can achieve communication with a far away receiver like base station (BS) if the PS is not too far and the receiver can find a way to separate the two links, which is the primary motivation for the setup shown in Fig 3.1. Emerging applications that motivate the selection of time-selective fading channel for ambient backscatter include smart fabrics where tags/sensors are integrated into garments for monitoring vital signs [29], and sensors deployed on the traffic signs. The impulse response of the channel at Rx corresponding to the DL and BL links in terms of the dominant non line-of-sight (NLOS) path and the Rx antenna array response is given as follows [70, 71]:

$$\mathbf{h}(t) = \underbrace{\sum_{n=1}^{N} c_n e^{j\phi_n - j2\pi c\tau_n/\lambda + j2\pi f_d \cos\psi_n t}}_{h_0(t)} \mathbf{a}(\theta)\delta\left(t-\bar{\tau}\right), \tag{3.1}$$

where the dominant NLOS path can be assumed to be a combination of N independent and non-resolvable sub-paths due to the presence of local scatterers around the transmitter. The nth sub-path is characterized by the gain c_n, the phase offset ϕ_n, the time delay τ_n, the maximum Doppler spread (DS) f_d, and the angle of departure (AoD) ψ_n at the transmitter, as given in the equation, δ represents the delta function, and $\bar{\tau}$ is the mean of the individual delays τ_n of the sub-paths. The remaining parameters $\mathbf{a}(.)$ and θ are the Rx antenna array response vector, and AoA of the NLOS path, respectively. The phase offset ϕ_n of each sub-path is uniformly distributed over $[0, 2\pi)$, and the additional phase offset resulting from the path-delay τ_n can also be shown to be uniformly distributed over $[0, 2\pi)$ since the frequency of operation is very high [72, Lemma 4]. Applying the central limit theorem (CLT) to the n independent sub-paths, the magnitude of the variable $h_0(t)$ can be shown as Rayleigh distributed. This channel environment is illustrated in Fig. 3.2. The channel described here is valid when one of the PS or BTx or both are mobile, and the receiver is located above the rooftops (such as BS) resulting in spatial correlation across the antennas. The channel of the PS-BTx link will be similar to $h_0(t)$ with additional DS coming from the local scatterers around BTx.

The rate at which the coefficient $h_0(t)$ varies is dependent on the maximum Doppler spread f_d and the angular spread ψ_n of the sub-paths at the mobile user. These parameters

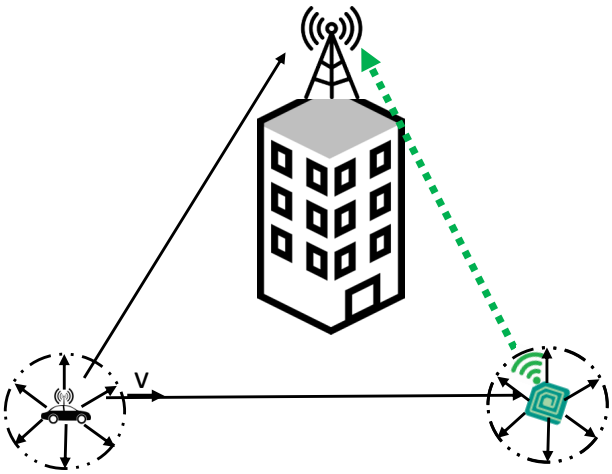

Figure 3.1: System model for the ambient backscatter setup.

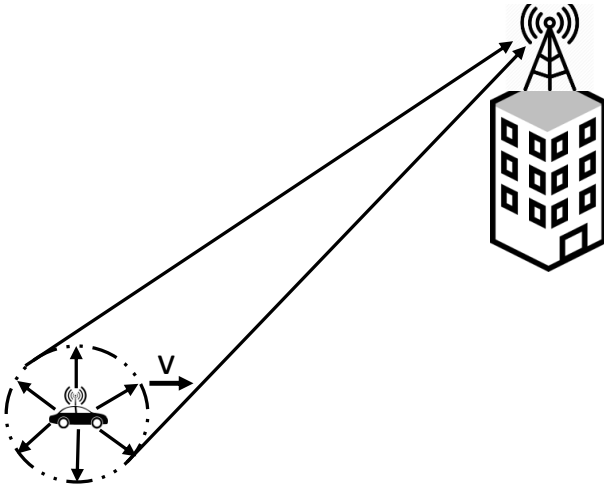

Figure 3.2: Illustration of the time-selective fading channel.

are large enough in this case due to the movement of the user and the presence of local scatterers, resulting in a fast variation of $h_0(t)$. On the other hand, the array response vector $\mathbf{a}(.)$ depends on the AoA θ of the NLOS path. The time-scale over which this parameter θ evolves is several orders of magnitude larger compared to the coherence time of $h_0(t)$, and hence can be tracked by the system. Therefore, while the channel coefficient at the receiver will be changing for each ambient symbol, the angular variation corresponding to AoA of the received signal will not change at the same rate and can be assumed to be constant for few symbol periods. The MA receiver designed in this work will build on this point to improve the BER performance of the system. More information on this property of the fading channels can be found in [73–75].

Remark 3.1. The assumption of spatially correlated channel at the Rx is typically valid for a BS located above the rooftops as the angular spread is small in these scenarios. We assume this to be valid for a backscatter device also by considering a single dominant NLOS path. Handling the case of multiple angular paths at the Rx is left as a promising future work. Further, extension of the non-coherent detection approach proposed in the current work to a frequency-selective channel is another promising area for future investigation.

The auto-correlation function (ACF) of the fading process for the DL and BL links is

$$\mathbb{E}_{\theta_n,\tau_n,\bar{\psi}}\left[h_0(t)h_0^*(t+t_d)\right] = \left(\sum_{n=1}^{N}|c_n|^2\right)\mathbb{E}_{\bar{\psi}}[e^{-j2\pi f_d \cos\bar{\psi}t_d}] = J_0(2\pi f_d t_d), \tag{3.2}$$

where $J_0(.)$ is the zero order Bessel function of the first kind. This result obtained under the assumption of uniformly distributed azimuthal AoD and unit sum energy of the sub-paths is known as Clarke's reference model [76]. Similarly, the ACF for the PS-BTx link is

given by $J_0(2\pi f_d t_d)J_0(2\pi a f_d t_d)$, where a is the ratio of the DS at BTx and PS. The Clarke's model cannot be exactly realized in practice, and therefore the Jake's model based on sum of sinusoids is used to generate channel samples that have characteristics similar to the reference model [76].

Autoregressive (AR) modeling of fading channels

Though Jakes' sum of sinusoids approach to model the temporal-fading process is widely used, it requires large number of sinusoids (and thereby increased complexity) to match the Clarke's reference model and is not mathematically tractable. Hence, this approach is not always convenient to apply for procedures such as channel modeling, estimation and equalization. Instead, AR models are used either to decrease the complexity of generating accurate correlated samples of the time-domain fading process or for the derivation of the equalization parameters [77–80]. Therefore, to simplify the analysis, the time-selective fading channel in our work is modeled as an AR process. The correlation matching (CM) criterion of the AR model imposes a condition that the ACF of the approximated process matches the sampled ACF of the Jakes' model. An AR process of order p is given by [77]:

$$h[n] = \sum_{k=1}^{p} a_k h[n-k] + v[n], \tag{3.3}$$

where $v[n]$ is a complex white Gaussian noise process with uncorrelated real and imaginary components. In the case of Rayleigh fading, $v[n]$ has zero mean. The parameters related to the AR model are given by $\{a_1, a_2, ..., a_k\}$ and the variance of $v[n]$ by σ_p^2. The ACF of this approximated process of order p matches exactly with the samples of the desired ACF upto p taps. The accuracy of this modeling approach using AR process increases with higher order approximations. However, as shown in [81], the first order AR model obtained by setting $p = 1$ is a sufficiently accurate model which can be represented as [78]:

$$h[n] = \rho\, h[n-1] + \sqrt{1-\rho^2}\, g[n], \tag{3.4}$$

where $h[n]$ and $h[n-1]$ are the channel gains in the current and previous time periods, $g[n]$ is the complex white Gaussian noise process with variance σ_h^2, and $\rho \in [0, 1)$ is the correlation between the fading coefficients of the consecutive symbols. Depending on the link, the correlation factor ρ is given by either $J_0(2\pi f_d T_s)$ or $J_0(2\pi f_d T_s)J_0(2\pi a f_d T_s)$, where T_s is the symbol duration. The value of ρ determines the rate at which the current channel coefficient de-correlates across time. The recursive relation in (3.4) can be written in the direct form as:

$$h[n] = \rho^{n-1} h[1] + \sqrt{1-\rho^2} \left\{ \sum_{k=1}^{n-1} \rho^{n-k-1} g[k] \right\}. \tag{3.5}$$

Note that the modeling of the time-selective fading using the first order AR process in the current work is a good first step, and can be extended to a higher order AR process in future studies.

Remark 3.2. The time-selective fading implicitly handles the extreme cases of independent fading ($\rho = 0$) and highly correlated fading ($\lim \rho \to 1^-$). However, the block fading obtained by configuring $\rho = 1$ requires a separate analysis, and will be handled separately in a future work.

3.2.2 Signal Model

In general, the signal scattered from the backscatter device to the receiver is given by [6]:

$$r = (A - \Gamma)\, s = As - \Gamma s, \tag{3.6}$$

where r is the signal at the receiver, s is the signal backcattered at the device, A is the load-independent complex coefficient of the device, and Γ is the reflection coefficient of backscatter node at the boundary of the antenna and the circuit. The device modulates the signal by varying the load impedance to change the parameter Γ that controls the reflected signal. The first and second terms in (1.3) correspond to the *structural mode* and *antenna mode* scattering components, respectively. A binary modulation scheme can be implemented by choosing two different values Γ_0 and Γ_1. As shown later, non-coherent detection will result in good error performance only for the case of on-off keying (OOK) modulation. It is possible to achieve this modulation for antennas with $|A| \leq 1$ by designing the appropriate load impedance using only passive components [7, 8].

Since the data rate of most IoT applications is rather small, it is reasonable to assume that the data rate of backscatter is lower compared to that of the ambient symbols. Under this assumption, a single variable is enough to represent the backscatter data for a signal sample set of size N. The signal at the SA receiver is the summation of the direct and backscatter signals, which can be mathematically represented as follows:

$$y[n] = \underbrace{h_r[n]x[n]}_{\text{direct signal}} + \underbrace{\alpha b\; h_b[n]\; h_t[n]x[n]}_{\text{backscatter signal}} + \underbrace{w[n]}_{\text{AWGN}}, \tag{3.7}$$

where $x[n]$ is the ambient symbol sequence in complex baseband, $w[n]$ is the additive complex Gaussian noise, $h_r[n], h_b[n]$ and $h_t[n]$ are independent and identical distributed (i.i.d.) zero mean complex Gaussian channel coefficients with variance σ_h^2, b is the backscatter data, α is related to the parameter Γ_1 of the BTx node. The channel coefficients $h_r[n], h_b[n]$ and $h_t[n]$ are modeled using the AR process of order 1, each having a different correlation factor given by ρ_r, ρ_b, and ρ_t, respectively. Since non-coherent detection does not require the CSI, the channel gains $h_r[n], h_b[n]$ and $h_t[n]$ are unknown at the Rx. The received signal at the MA receiver with antennas $M_r \geq 2$ is given by:

$$\mathbf{y}[n] = \begin{bmatrix} y_0[n] \\ y_1[n] \\ \vdots \\ y_{M_r-1}[n] \end{bmatrix} = h_r[n] \begin{bmatrix} 1 \\ e^{j\phi_1} \\ \vdots \\ e^{j(M_r-1)\phi_1} \end{bmatrix} x[n] + \alpha b\, h_b[n] h_t[n] \begin{bmatrix} 1 \\ e^{j\phi_2} \\ \vdots \\ e^{j(M_r-1)\phi_2} \end{bmatrix} x[n] + \begin{bmatrix} w_0[n] \\ w_1[n] \\ \vdots \\ w_{M_r-1}[n] \end{bmatrix}, \tag{3.8}$$

where the phase offset ϕ_i between consecutive antenna elements for each link is given by $\frac{2\pi}{\lambda} d \cos\theta_i$ for a linear uniform antenna array. Note that the AoA θ_2 of the BL is independent of the AoA θ_1 of the DL.

The null and alternate hypotheses of the binary hypothesis testing problem are denoted as $\mathcal{H}_0$ and $\mathcal{H}_1$, respectively. The BTx modulates the backscatter data using the binary OOK modulation scheme. As is generally the case, the ambient symbol sequence $x[n]$ is assumed to be i.i.d., with unit energy on average. We also assume that the noise energy σ_n^2, the average channel energy σ_h^2, and the correlation factors ρ_r, ρ_b, and ρ_t are known at the receiver. In fact, they can be perfectly estimated with a long observation interval under the assumption that they remain constant, which is true as they are large-scale parameters.

Test Statistic (TS)

Due to the reasons outlined in contributions, the receiver architecture is based on the TS of the mean of the received signal samples, unlike the conventional TS of the average energy of the received signal samples. The new TS can be mathematically denoted as:

$$Z = \frac{1}{N} \sum_{n=1}^{N} y[n] \tag{3.9}$$

It should be noted that derivation of the optimal TS for the time-selective channel is still an open problem. In fact, the optimality of the TS, although important in general, has not really been the main focus of the receiver design for ambient backscatter systems. Some very recent work on the optimal detection and the selection of testing variable for a non-coherent detector under block fading channel can be found in [82, 83].

3.3 Detection at a Single Antenna Receiver

In this section, we initially derive the growth rate of the expectation and variance of the generalized sum sequence of interest. This result is then used to evaluate the conditional distributions of the signal of the two hypotheses, and ultimately the BER of the SA receiver.

3.3.1 Growth Rate of a Generalized Sum Sequence of Interest

Consider the general sum sequence $S_N = \sum_{n_1,n_2} \rho^{|n_1-n_2|} x[n_1]x^*[n_2]$, where $m \in \{1, 2\}$, defined as the sum of non-i.i.d. RVs, which plays an important role in the signal detection procedure. In particular, the asymptotic property of the sum sequence given by $M_N = \frac{S_N}{N}$ is required to derive the conditional distributions. For this setup, if we can show that the growth rate of both the expectation and variance of S_N is of the order of N (the number of samples), that is sufficient to conclude that the sequence M_N converges to its mean value as the sample size tends to infinity. Using the Chebyshev inequality, it is possible to show that

this will indeed be the case if the higher order moments of the RV X representing the i.i.d. ambient data sequences $x[n]$ are finite. These conditions on the moments of $x[n]$ might be stronger than necessary but are nevertheless reasonable and assumed here to simplify the derivation. One of the second order moments of the ambient sequences $x[n]$ is the sample energy which is given by:

$$\bar{E} = \mathbb{E}\left[|X|^2\right] = \frac{1}{N}\sum_{n=1}^{N}|x[n]|^2. \tag{3.10}$$

The result capturing the growth rate of S_N is provided in the following Lemma. Note that one has to be careful in deriving these concentration results since the sum sequence S_N is not composed of i.i.d elements. Please see the proof of the following Lemma for more details.

Lemma 3.3. *The expectation and variance of the sum sequence S_N both grow asymptotically of the order of N, i.e., $\mathbb{E}[S_N] = \Theta(N)$ and $\mathrm{Var}[S_N] = \Theta(N)$, where $f(x) = \Theta(g(x))$ means that $f(x)$ is asymptotically bounded both from above and below by $g(x)$. As a consequence, the sequence M_N concentrates around $\mathbb{E}[M_N]$ when $N \to \infty$, where*

$$\mathbb{E}\left[M_N\right] = \mathbb{E}\left[|X|^2\right] + \frac{2\rho}{1-\rho}\left(1 - \frac{1-\rho^N}{N(1-\rho)}\right)|\mathbb{E}[X]|^2. \tag{3.11}$$

Proof: See Appendix B.1. ■

The analysis related to Lemma 3.3 on the asymptotic growth rate of S_N is discussed now by plotting the simulation results. The plots for the distributions of M_N and M_N^b with increasing sample size N are shown in Figs. 3.3a and 3.3b, where it can be observed that the mean values remain constant while their variances decrease as the signal sample size increases.

3.3.2 Conditional Distributions of the Signal

The null and alternate hypotheses $\mathcal{H}_0$ and $\mathcal{H}_1$ correspond to the scenarios of the transmitted backscatter data $b \equiv 0$ and $b \equiv 1$, respectively.

Null Hypothesis $\mathcal{H}_0$

For the AR process used in this paper to model the time-selective fading, the channel gain evolves with time according to (3.4), which can be described as a weighted average of the previous channel gain and a new variable. Due to this dependence of the current channel gain on the previous gains, the received signal samples are correlated, and hence the co-variances of the samples are non-zero in general. As a consequence, both the variances and co-variances of the signal has to be evaluated to derive the variance of the the mean received signal Z. We transform the expression for each received signal sample into a sum

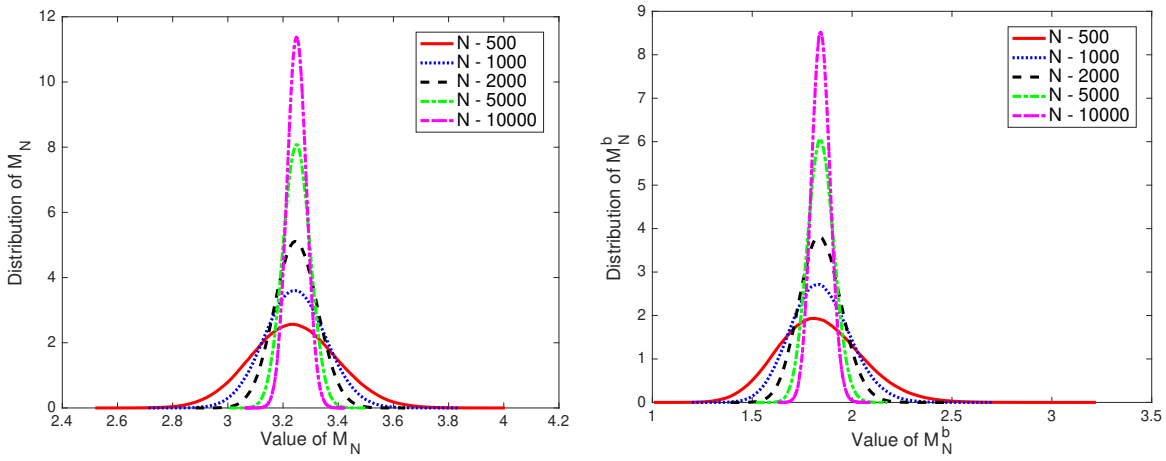

(a) (b)

Figure 3.3: Probability density functions of (a) M_N and (b) M_N^b for varying N with $\rho = 0.6$.

representation of independent RVs. This will simplify the evaluation of both the variance of each signal sample and the subsequent evaluation of the variance of Z. This can be represented as following:

$$y[n] = h_r[n]x[n] + w[n] = \left(\rho_r^{n-1}h_r[1] + \sqrt{1-\rho_r^2}\left\{\sum_{k=1}^{n-1}\rho_r^{n-k-1}g_r[k]\right\}\right)x[n] + w[n], \quad (3.12)$$

where the channel gain $h_r[1]$ in the first time slot of a window can be independently configured.

Lemma 3.4. *The probability density function (PDF) of Z conditioned on $\mathcal{H}_0$ is given by*

$$\mathcal{H}_0 : Z \sim \mathcal{CN}\left(0, \mathrm{Var}_0^{\mathrm{SA}}\right), \quad (3.13)$$

where $\mathrm{Var}_0^{\mathrm{SA}} = \frac{\sigma_h^2\mathbb{E}\left[|X|^2\right]+\sigma_h^2\frac{2\rho_r}{1-\rho_r}\left(1-\frac{1-\rho_r^N}{N(1-\rho_r)}\right)|\mathbb{E}[X]|^2+\sigma_n^2}{N}$ *is the conditional variance of $\mathcal{H}_0$.*

Proof: See Appendix B.2. ■

Alternate Hypothesis $\mathcal{H}_1$

The received signal for a sample n, where $1 \leq n \leq N$, under the alternate hypothesis $\mathcal{H}_1$ is given by:

$$y[n] = h_r[n]x[n] + \underbrace{\alpha h_b[n]h_t[n]x[n]}_{y_b[n]} + w[n], \quad (3.14)$$

where $h_r[n], h_b[n]$ and $h_t[n]$ are the fading gains following the process defined by (3.5). Unlike the case of $\mathcal{H}_0$, further work is needed to derive the distribution for $\mathcal{H}_1$ since the conditional distribution of each sample is not complex Gaussian anymore. However, we preserve the Gaussian property of the samples by further conditioning on $h_b[n]$ and show that this conditional distribution asymptotically matches the true distribution. Only the distribution corresponding to $y_b[n]$ is needed to be derived and the sequence

$$M_N^b = \sum_{n_1,n_2} \rho_t^{|n_1-n_2|}\, h_b[n_1] h_b^*[n_2] x[n_1] x_2^*[n_2]$$

related to $y_b[n]$ is the corresponding parameter of $\mathcal{H}_1$, similar to M_N of $\mathcal{H}_0$. The following Lemma captures this analysis on the conditional distribution of $\mathcal{H}_1$.

Lemma 3.5. *The PDF of Z conditioned on $\mathcal{H}_1$ is given by*

$$\mathcal{H}_1 : Z \sim \mathcal{CN}\left(0, \mathrm{Var}_1^{\mathrm{SA}}\right), \tag{3.15}$$

where $\mathrm{Var}_1^{\mathrm{SA}} = \frac{\sigma_h^2(1+|\alpha|^2\sigma_h^2)\mathbb{E}\left[|X|^2\right]+\sigma_h^2\left[\frac{2\rho_r}{1-\rho_r}\left(1-\frac{1-\rho_r^N}{N(1-\rho_r)}\right)+|\alpha|^2\sigma_h^2\frac{2\rho_t\rho_b}{1-\rho_t\rho_b}\left(1-\frac{1-\rho_t^N\rho_b^N}{N(1-\rho_t\rho_b)}\right)\right]|\mathbb{E}[X]|^2+\sigma_n^2}{N}$.

Proof: See Appendix B.3. ∎

The results are valid for all ρ_r, ρ_b and $\rho_t \in [0, 1)$, and the special case of independent fading analyzed in the conference version [84] can be obtained by configuring ρ_r, ρ_b and ρ_t all to zero.

3.3.3 Bit Error Rate

From the conditional distribution analysis, we see that the PDFs of the two hypotheses have same mean but different variances, which are compared to obtain the optimal detection threshold.

Theorem 3.6. *The average BER of a SA receiver is given by*

$$P_{\mathrm{SA}}(e) = \frac{1}{2} - \frac{1}{2}e^{-\frac{T_{\mathrm{SA}}}{\mathrm{Var}_1^{\mathrm{SA}}}} + \frac{1}{2}e^{-\frac{T_{\mathrm{SA}}}{\mathrm{Var}_0^{\mathrm{SA}}}}, \tag{3.16}$$

where $T_{\mathrm{SA}} = \ln\left(\frac{\mathrm{Var}_1^{\mathrm{SA}}}{\mathrm{Var}_0^{\mathrm{SA}}}\right)\frac{\mathrm{Var}_1^{\mathrm{SA}}\mathrm{Var}_0^{\mathrm{SA}}}{\mathrm{Var}_1^{\mathrm{SA}}-\mathrm{Var}_0^{\mathrm{SA}}}$ *is the optimal detection threshold.*

Proof: See Appendix B.4. ∎

Asymptotic analysis

The ratio of the variances of $\mathcal{H}_0$ and $\mathcal{H}_1$ of the SA receiver is:

$$K = \frac{\mathrm{Var}_1^{\mathrm{SA}}}{\mathrm{Var}_0^{\mathrm{SA}}} = 1 + \frac{|\alpha|^2\sigma_h^4\left\{1+\frac{2\rho_t\rho_b}{1-\rho_t\rho_b}\left(1-\frac{1-\rho_t^N\rho_b^N}{N(1-\rho_t\rho_b)}\right)\frac{|\mathbb{E}[X]|^2}{\mathbb{E}[|X|^2]}\right\}}{\sigma_h^2\left\{1+\frac{2\rho_r}{1-\rho_r}\left(1-\frac{1-\rho_r^N}{N(1-\rho_r)}\right)\frac{|\mathbb{E}[X]|^2}{\mathbb{E}[|X|^2]}\right\}+\mathrm{SNR}^{-1}}. \tag{3.17}$$

The asymptotic average BER can be simplified as follows:

$$P_{\mathrm{SA}}^{\mathrm{asym}}(e) \overset{(a)}{=} \lim_{\mathrm{SNR}\to\infty} \frac{1}{2}(1 - K^{\frac{-1}{K-1}} + \frac{1}{K}^{\frac{1}{1-\frac{1}{K}}}) \overset{(b)}{=} \frac{1}{2}(1 - K_{\infty}^{\frac{-1}{K_{\infty}-1}} + \frac{1}{K_{\infty}}^{\frac{1}{1-\frac{1}{K_{\infty}}}}), \tag{3.18}$$

where (a) results from the substitution of the expression for T_{SA} and replacing the ratio $\frac{\mathrm{Var}_1^{\mathrm{SA}}}{\mathrm{Var}_0^{\mathrm{SA}}}$ with K defined earlier, and (b) follows from the substitution of K with K_∞ obtained as $\mathrm{SNR} \to \infty$.

Remark 3.7. Clearly, the BER expressions under the new receiver architecture are independent of N when the expectation $\mathbb{E}[X]$ of the ambient data sequence is zero and/or the time-domain fading is uncorrelated (all the ρ's equal 0). Furthermore, the asymptotic BER value, with respect to the increasing SNR, reaches an error floor instead of converging to zero. This error floor is numerically demonstrated later in Fig. 3.5a. This necessitates the need to develop better techniques to decode data in a time-selective channel, which takes us to the next main contribution.

3.4 Detection at a Multi-Antenna Receiver

3.4.1 Effective Signal and Antenna Gain

The main reason for the poor BER performance of the SA receiver is the presence of the DL from the ambient PS, which only acts as an interference since it does not carry any backscatter data. The signals impinging on the neighboring antenna elements are phase shifted versions of the signal at the first antenna in addition to the independent additive noise. Observe that the phase offset of the BL is independent of the phase offset of the DL. The interference of the DL can be canceled by reversing the DL phase offset at each antenna starting from the second element, and subtracting the resultant signal with that at the first antenna, as given below:

$$\tilde{\mathbf{y}}[n] = \begin{bmatrix} e^{-j\phi_1} y_1[n] - y_0[n] \\ \vdots \\ e^{-j(M_r-1)\phi_1} y_{M_r-1}[n] - y_0[n] \end{bmatrix} = \tilde{\mathbf{a}}\, \alpha b\, h_b[n] h_t[n] x[n] + \tilde{\mathbf{w}}[n], \tag{3.19}$$

where the effective antenna array and noise vectors $\tilde{\mathbf{a}}$ and $\tilde{\mathbf{w}}[n]$, respectively, are given by:

$$\tilde{\mathbf{a}} = \begin{bmatrix} 2\sin(\frac{\phi_2-\phi_1}{2}) e^{j(\frac{\phi_2-\phi_1}{2})} \\ \vdots \\ 2\sin(M_r-1)(\frac{\phi_2-\phi_1}{2}) e^{j(M_r-1)(\frac{\phi_2-\phi_1}{2})} \end{bmatrix}, \tilde{\mathbf{w}}[n] \quad = \begin{bmatrix} e^{-j\phi_1} w_1[n] - w_0[n] \\ \vdots \\ e^{-j(M_r-1)\phi_1} w_{M_r-1}[n] - w_0[n] \end{bmatrix}. \tag{3.20}$$

The covariance matrix of the resultant noise vector $\tilde{\mathbf{w}}[n]$ is given by:

$$\mathbf{K}_{\tilde{\mathbf{W}}} = \sigma_n^2 \hat{\mathbf{K}}_{\tilde{\mathbf{W}}}, \quad \text{where } \hat{\mathbf{K}}_{\tilde{\mathbf{W}}} = \begin{bmatrix} 2 & 1 & \dots & 1 \\ \vdots & \vdots & \ddots & \vdots \\ 1 & 1 & \dots & 2 \end{bmatrix}, \tag{3.21}$$

which means that the resultant noise after the DL cancellation is correlated. The vector detection problem can be converted to scalar detection by appropriately designing the weight vector. The effective scalar signal samples for the averaging operation can be obtained by the following steps: 1) Whiten the additive noise with the linear transformation $\hat{\mathbf{K}}_{\tilde{\mathbf{W}}}^{-\frac{1}{2}}$, and 2) Project the output of the first step along the direction of the resultant antenna array response $\hat{\mathbf{K}}_{\tilde{\mathbf{W}}}^{-\frac{1}{2}}\tilde{\mathbf{a}}$. The combined weight vector of the two operations is $\mathbf{r} = \frac{\hat{\mathbf{K}}_{\tilde{\mathbf{W}}}^{-1}\tilde{\mathbf{a}}}{|\hat{\mathbf{K}}_{\tilde{\mathbf{W}}}^{-\frac{1}{2}}\tilde{\mathbf{a}}|}$, and the effective signal after these steps is:

$$y_{\text{eff}}[n] = \mathbf{r}^*\tilde{\mathbf{y}}[n] = \frac{\tilde{\mathbf{a}}^*\hat{\mathbf{K}}_{\tilde{\mathbf{W}}}^{-1}\tilde{\mathbf{a}}}{|\hat{\mathbf{K}}_{\tilde{\mathbf{W}}}^{-\frac{1}{2}}\tilde{\mathbf{a}}|}\alpha b\, h_b[n]h_t[n]x[n] + \frac{\tilde{\mathbf{a}}^*\hat{\mathbf{K}}_{\tilde{\mathbf{W}}}^{-1}}{|\hat{\mathbf{K}}_{\tilde{\mathbf{W}}}^{-\frac{1}{2}}\tilde{\mathbf{a}}|}\tilde{\mathbf{w}}[n]. \tag{3.22}$$

Hence, the gain in the average signal power with multiple antennas is $\tilde{\mathbf{a}}^*\hat{\mathbf{K}}_{\tilde{\mathbf{W}}}^{-1}\tilde{\mathbf{a}}$, while the noise power remains at σ_n^2. Therefore, the antenna (SNR) gain due to multiple antennas is given by $\tilde{\mathbf{a}}^*\hat{\mathbf{K}}_{\tilde{\mathbf{W}}}^{-1}\tilde{\mathbf{a}}$. This procedure to generate the scalar sample $y_{\text{eff}}[n]$ maximizes the SNR of the signal. In addition the resultant sample $y_{\text{eff}}[n]$ is a sufficient statistic for the detection procedure that follows. It can be further shown that this procedure also minimizes the mean square error for the signal estimation, and is hence known as the linear minimum mean squared error estimation (MMSE) [85]. The phase-offset components $e^{j\phi_1}$ and $e^{j\phi_2}$ of the two links can be estimated from the received signal by formulating a parameter estimation problem. However, this is beyond the scope of the current work, and hence they are assumed to be perfectly known at the receiver. The sample average given by $Z = \frac{1}{N}\sum_{n=1}^{N} y_{\text{eff}}[n]$ is used as the new test statistic for detection.

Lemma 3.8. *The antenna (SNR) gain $G = \tilde{\mathbf{a}}^*\hat{\mathbf{K}}_{\tilde{\mathbf{W}}}^{-1}\tilde{\mathbf{a}}$ of the MA receiver is given by:*

$$G = M_r - \frac{1}{M_r} - \frac{2}{M_r}\frac{\sin\left((M_r-1)\frac{\phi_2-\phi_1}{2}\right)}{\sin\left(\frac{\phi_2-\phi_1}{2}\right)}\cos\left(\frac{M_r}{2}(\phi_2-\phi_1)\right) - \frac{1}{M_r}\frac{\sin^2\left((M_r-1)\frac{\phi_2-\phi_1}{2}\right)}{\sin^2\left(\frac{\phi_2-\phi_1}{2}\right)}. \tag{3.23}$$

Proof: See Appendix B.5. ∎

For notational simplicity, the antenna gain is represented as a single variable G without any input arguments even though it is a function of the two phase offsets (and hence the AoAs).

Remark 3.9. The antenna gain of a dual-antenna Rx ($M_r = 2$) will simplify to $G = 2\sin^2\left(\frac{\phi_2-\phi_1}{2}\right)$, which is zero when the AoAs of the DL and BL links are almost the same. On the other hand, the antenna gain G for a Rx with $M_r > 2$ equals $(1-\frac{1}{M_r})(M_r-2)$, which is non-zero even when the two AoAs are almost the same. Hence, additional angular resolution is obtained with $M_r > 2$, which is useful for the applications where the AoAs of the DL and BL links are similar.

3.4.2 Conditional Distributions of the Effective Signal and Bit Error Rate

Now, we derive the conditional distributions of the effective signal derived in (3.22), and then use them to evaluate the average BER of the MA receiver.

Lemma 3.10. *The conditional PDFs of Z for the two hypotheses $\mathcal{H}_0$ and $\mathcal{H}_1$ are given by*

$$\mathcal{H}_i : Z \sim \mathcal{CN}\left(0, \mathrm{Var}_i^{\mathrm{MA}}\right), \tag{3.24}$$

where $\mathrm{Var}_0^{\mathrm{MA}} = \frac{\sigma_n^2}{N}$ *and* $\mathrm{Var}_1^{\mathrm{MA}} = \frac{G|\alpha|^2\sigma_h^4\left\{\mathbb{E}\left[|X|^2\right]+\frac{2\rho_t\rho_b}{1-\rho_t\rho_b}\left(1-\frac{1-\rho_t^N\rho_b^N}{N(1-\rho_t\rho_b)}\right)|\mathbb{E}[X]|^2\right\}+\sigma_n^2}{N}$.

Proof: See Appendix B.6. ∎

Theorem 3.11. *The average BER of the MA receiver is given by:*

$$P_{\mathrm{MA}}(e) = \int_{-\pi}^{\pi}\int_{-\pi}^{\pi}\frac{1}{2\pi}\times\frac{1}{2\pi}\times\frac{1}{2}\left(1-e^{-\frac{T_{\mathrm{MA}}}{\mathrm{Var}_1^{\mathrm{MA}}}}+e^{-\frac{T_{\mathrm{MA}}}{\mathrm{Var}_0^{\mathrm{MA}}}}\right)\mathrm{d}\theta_1\mathrm{d}\theta_2, \tag{3.25}$$

where $T_{\mathrm{MA}} = \ln\left(\frac{\mathrm{Var}_1^{\mathrm{MA}}}{\mathrm{Var}_0^{\mathrm{MA}}}\right)\frac{\mathrm{Var}_1^{\mathrm{MA}}\mathrm{Var}_0^{\mathrm{MA}}}{\mathrm{Var}_1^{\mathrm{MA}}-\mathrm{Var}_0^{\mathrm{MA}}}$ *is the optimal detection threshold.*

Proof: See Appendix B.7. ∎

It should be noted that the SA scenario is not exactly a special case of the MA scenario, even though there are similarities in the non-coherent detection approach and the subsequent bit error rate evaluation of the two receivers. Mainly, the additional operation of the DL interference cancellation in the MA scenario results in an effective antenna array vector and correlated additive noise, which necessitates the handling of the MA receiver separately from the SA receiver.

Asymptotic analysis

The ratio of the variances of $\mathcal{H}_0$ and $\mathcal{H}_1$ of the MA receiver is:

$$K = \frac{\mathrm{Var}_1^{\mathrm{MA}}}{\mathrm{Var}_0^{\mathrm{MA}}} = 1 + G|\alpha|^2\sigma_h^4\left\{1+\frac{2\rho_t\rho_b}{1-\rho_t\rho_b}\left(1-\frac{1-\rho_t^N\rho_b^N}{N(1-\rho_t\rho_b)}\right)\frac{|\mathbb{E}[X]|^2}{\mathbb{E}\left[|X|^2\right]}\right\}\mathrm{SNR}. \tag{3.26}$$

From this, the asymptotic conditional BER of the MA receiver as SNR $\to \infty$ can be derived as:

$$P_{\text{MA}}^{\text{asym}}(e|\phi_1,\phi_2) = \frac{1}{2}(1 - e^{-\frac{T_{\text{MA}}}{\text{Var}_1^{\text{MA}}}} + e^{-\frac{T_{\text{MA}}}{\text{Var}_0^{\text{MA}}}}) \overset{(a)}{=} \frac{1}{2}(1 - K^{\frac{-1}{K-1}} + \frac{1}{K}^{\frac{1}{1-\frac{1}{K}}}) \overset{(b)}{=} 0, \tag{3.27}$$

where (a) results from substituting the expression for T_{MA}, and replacing $\frac{\text{Var}_1^{\text{MA}}}{\text{Var}_0^{\text{MA}}}$ with K defined in (3.26), and (b) follows from the standard limit $\lim_{x\to\infty}(x)^{-1/x-1} = 1$, and $\frac{1}{K} \to 0$ as SNR $\to \infty$. It should be noted that the asymptotic value of K when $N \to \infty$ is non-zero. Hence, the BER does not converge to 0.5 as $N \to \infty$ even though the individual variances converge to zero.

Remark 3.12. In case of fast-fading, where the fading gains are independent across the ambient symbols, the average BER is only dependent on the expected value of the energy of the ambient symbol. This special case concurs with our analysis in [84]. Alternatively, if the mean value of the ambient symbol is zero (which is the case for most of the modulation schemes), then again the average BER is only dependent on the expected value of the energy. Lastly, it can be inferred from the BER expression that the average BER is an increasing function of the correlation factor.

3.5 Receiver Synchronization and Parameter Estimation

3.5.1 Delay Parameters

In this section, we discuss receiver synchronization in ambient backscatter, which is an important ingredient of the proposed system design. First, we briefly mention the parameters to be estimated, and then either provide an analysis of the impact of incorrect estimation of the parameter on the detection performance or provide a procedure to estimate the parameter. In general, the estimation of both the timing delay and the carrier phase offset is necessary in a communication system. In our setup, however, carrier phase estimation is not required since non-coherent detection is employed. As the symbol duration of the backscatter data is larger than that of the ambient data, it is not required to perform symbol synchronization at the backscatter device. Therefore, the symbol timing recovery at the receiver is our main concern. The parameters T_a and N represent the duration of the ambient symbol and the sample window size at the receiver, respectively, which are assumed to be known *a priori*. The duration of the backscatter symbol T_b is related to the above two parameters as $T_b = NT_a$. Due to the architecture adopted at the receiver, it needs to estimate the following parameters: (i) the timing delay $\tau \in [0, T_a)$ of the ambient data to obtain signal samples correctly, and (ii) the sample number $k \in \{0, 1, 2, \cdots, N-1\}$ to reset the counter of the signal sample window. The estimation of the delay τ for time-selective fading channels is a well-studied topic, where correlation-based techniques are widely used

to solve the ML estimation problem [86]. However, before going into those details, it would be worthwhile to investigate how significant would be the impact of incorrect estimation of the delay (given by $\hat{\tau}$) on the achievable BER. For the purpose of exposition, we assume that the pulse shape of the ambient symbols is rectangular, and hence the matched filter pulse is also rectangular. Due to the mismatch of the estimated delay, the discrete samples obtained at the SA receiver after the matched filtering can be represented as:

$$y[n] = \frac{\Delta\tau}{T_a} e^{j\phi_r} h_r[n-1]x[n-1] + \frac{T_a - \Delta\tau}{T_a} e^{j\phi_r} h_r[n]x[n] + \frac{\Delta\tau}{T_a} e^{j\phi_b} \alpha h_t[n-1]h_b[n-1]x[n-1] + e^{j\phi_r} \alpha h_t[n]h_b[n] \frac{T_a - \Delta\tau}{T_a} x[n] + w[n],$$

where $\Delta\tau = \tau - \hat{\tau} \in [0, T_a)$ equals the difference of the actual and the estimated path delays.

For a window of samples, the average of the samples will simplify as follows:

$$Z = \frac{1}{N}\sum_{n=1}^{N} y[n] = \frac{e^{j\phi_r}}{N}\left(\frac{\Delta\tau}{T_a} h_r[-1]x[-1] + \sum_{n=1}^{N-1} h_r[n]x[n] + \frac{T_a - \Delta\tau}{T_a} h_r[N]x[N]\right) + \frac{e^{j\phi_b}\alpha}{N}\left(\frac{\Delta\tau}{T_a} h_t[-1]h_r[-1]x[-1] + \sum_{n=1}^{N-1} h_t[n]h_b[n]x[n] + \frac{T_a - \Delta\tau}{T_a} h_t[N]h_b[N]x[N]\right). \tag{3.28}$$

From (3.28), it is clear that the impact of the timing recovery error on Z (and hence on the BER) will be negligible. In fact, due to the linear averaging operation of the new architecture, the receiver is robust to synchronization errors, and it does not require the estimation of delay τ.

For the other parameter of interest k, a procedure for estimation is provided. Suppose that backscatter device sends a preamble sequence of alternating bits $1010\cdots10$ (of length N_b), and the index k represents the delay reset of the counter corresponding to the window of signal samples. It should be noted here that the alternating bit sequences are commonly used in conventional networks for clock and frame synchronization, e.g., see [87]. The sample mean corresponding to backscatter symbols of $'0'$ and $'1'$ taken with a delay l are denoted as Z_0^l and Z_1^l, respectively. For the purpose of exposition, assume that the delay k is zero. When the sampling window is aligned properly, the energy of the average of the samples $|Z_0^0|^2$ and $|Z_1^0|^2$ corresponding to symbols $'0'$ and $'1'$ can be approximated by $\mathrm{Var}_0^{\mathrm{SA}}$ and $\mathrm{Var}_1^{\mathrm{SA}}$, respectively. Since, the received signal corresponding to symbol $'1'$ has both the DL and BL links, $\mathrm{Var}_1^{\mathrm{SA}}$ is higher compared to $\mathrm{Var}_0^{\mathrm{SA}}$ resulting in the ratio $\frac{|Z_1^0|}{|Z_0^0|} = C > 1$. When the sampling window is misaligned by exactly half the window size N, then both $Z_0^{N/2}$ and $Z_1^{N/2}$ contain equal number of ambient symbols that correspond to backscatter symbols $'1'$ and $'0'$, resulting in the ratio $\frac{|Z_1^{N/2}|}{|Z_0^{N/2}|} = 1$. In fact, the ratio $\frac{|Z_1^l|}{|Z_0^l|}$ for a general delay l will lie in the interval $(1, C)$. From this, one can conclude that $\frac{|Z_1^l|}{|Z_0^l|}$ is maximized when the sample

window is aligned to the delay k, and therefore the problem of estimating the parameter k can be formulated as following:

$$\hat{k} = \underset{l\in\{0,1,\cdots N-1\}}{\arg\max} \frac{|Z_1^l|}{|Z_0^l|}. \tag{3.29}$$

3.5.2 Correlation Factor and Phase Offset Inversion Parameters

Supposing that the delay k is perfectly estimated in the synchronization module, consider the consecutive samples $y_0^k[n]$ and $y_0^k[n+1]$ corresponding to the preamble bit 0 at the SA receiver. Taking cross-correlation of the two signals, the DL correlation factor ρ_r can be evaluated as:

$$\begin{aligned} E[y_0^k[n](y_0^k[n+1])^*] &= \mathbb{E}\left[(h_r[n]x[n]+w[n])((h_r^*[n+1]x^*[n+1]+w^*[n+1])\right] \\ &= \rho_r \mathbb{E}\left[|h_r[n]|^2\right]|\mathbb{E}\left[X\right]|^2 = \rho_r\sigma_h^2|\mathbb{E}\left[X\right]|^2 \implies \rho_r = \frac{E[y_0^k[n](y_0^k[n+1])^*]}{\sigma_h^2|\mathbb{E}\left[X\right]|^2}. \end{aligned} \tag{3.30}$$

Similarly, the combined correlation factor $\rho_t\rho_b$ of the BL can be evaluated as follows:

$$\rho_t\rho_b = \frac{E[y_1^k[n](y_1^k[n+1])^*] - E[y_0^k[n](y_0^k[n+1])^*]}{|\alpha|^2\sigma_h^4|\mathbb{E}\left[X\right]|^2}. \tag{3.31}$$

Now, consider the parameters $\mathbf{Z}_0^k$ and $\mathbf{Z}_1^k$ of the MA receiver for deriving the phase offset inversion components $e^{-j\phi_1}$ and $e^{-j\phi_2}$. Next, we provide a method to determine $e^{-j\phi_1}$ of the DL at the receiver. The samples corresponding to the preamble bit 0 at the consecutive antenna elements m and $m+1$ of the MA receiver are given by:

$$\begin{bmatrix} y_{0,m}^k[n] \\ y_{0,m+1}^k[n] \end{bmatrix} = h_r[n]e^{jm\phi_1}\begin{bmatrix} 1 \\ e^{j\phi_1} \end{bmatrix}x[n] + \begin{bmatrix} w_m[n] \\ w_{m+1}[n] \end{bmatrix}.$$

Taking the mean over samples for each preamble symbol of value 0 will result in:

$$\mathbf{Z}_0^k = \sum_{n=1}^{N}\frac{\mathbf{y}_0^k[n]}{N} = \begin{bmatrix} \sum_{n=1}^{N}\frac{y_{0,m}^k[n]}{N} \\ \sum_{n=1}^{N}\frac{y_{0,m+1}^k[n]}{N} \end{bmatrix} = \sum_{n=1}^{N}\frac{h_r[n]e^{jm\phi_1}x[n]}{N}\begin{bmatrix} 1 \\ e^{j\phi_1} \end{bmatrix} + \begin{bmatrix} \sum_{n=1}^{N}\frac{w_m[n]}{N} \\ \sum_{n=1}^{N}\frac{w_{m+1}[n]}{N} \end{bmatrix} = c_0\begin{bmatrix} 1 \\ e^{j\phi_1} \end{bmatrix} + \begin{bmatrix} n_0 \\ n_1 \end{bmatrix},$$

where $c_0 \sim \mathcal{CN}\left(0, \frac{1}{N}\left\{\mathbb{E}[|X|^2] + \frac{2\rho_r}{1-\rho_r}\left(1-\frac{1-\rho_r^N}{N(1-\rho_r)}\right)|\mathbb{E}\left[X\right]|^2\right\}\sigma_h^2\right)$, $n_0 \sim \mathcal{CN}(0, \frac{1}{N}\sigma_n^2)$ and $n_1 \sim \mathcal{CN}(0, \frac{1}{N}\sigma_n^2)$. Taking cross-correlation between the first and second elements of $\mathbf{Z}_0^k$, we get:

$$\mathbb{E}\left[\sum_{n=1}^{N}\frac{y_{0,m}^k[n]}{N}\sum_{n=1}^{N}\frac{(y_{0,m+1}^k)^*[n]}{N}\right] = \mathbb{E}\left[|c_0|^2\right]e^{-j\phi_1} + \mathbb{E}\left[c_0n_1^*\right] + \mathbb{E}\left[c_0^*e^{-j\phi_1}n_0\right] + \mathbb{E}\left[n_0n_1^*\right]$$

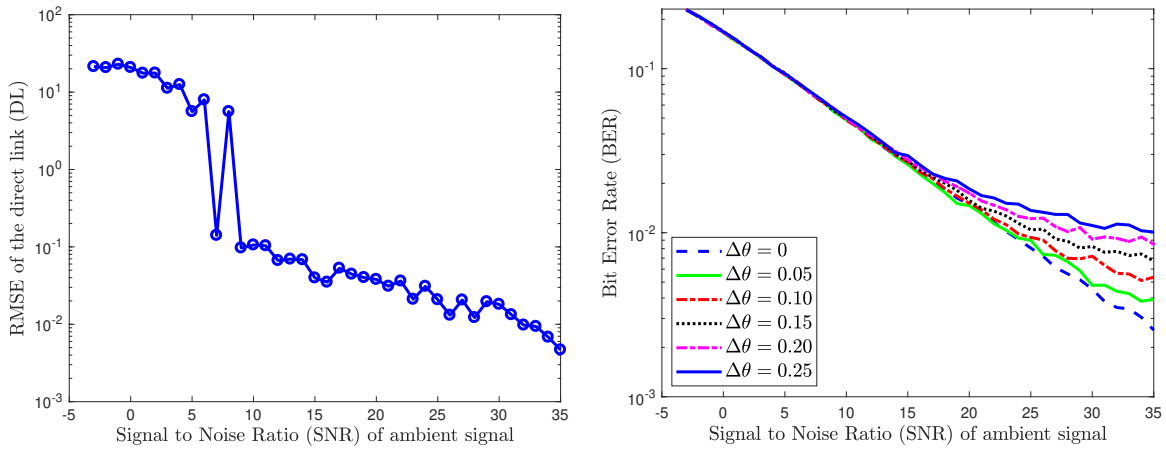

(a) (b)

Figure 3.4: (a) Root mean square error (RMSE) values of the estimated AoAs for the direct link (DL), and (b) BER performance comparison with estimation errors in AoA with $\Delta\theta = \{0, 0.05, 0.10, 0.15, 0.20, 0.25\}$.

$$= \frac{1}{N}\left\{\mathbb{E}\left[|X|^2\right] + \frac{2\rho_r}{1-\rho_r}\left(1 - \frac{1-\rho_r^N}{N(1-\rho_r)}\right)|\mathbb{E}\left[X\right]|^2\right\}\sigma_h^2 e^{-j\phi_1}$$

$$\implies e^{-j\phi_1} = \frac{\mathbb{E}\left[\sum_{n=1}^{N}\frac{y_{0,m}^k[n]}{N}\sum_{n=1}^{N}\frac{(y_{0,m+1}^k)^*[n]}{N}\right]}{\frac{1}{N}\left\{\mathbb{E}\left[|X|^2\right] + \frac{2\rho_r}{1-\rho_r}\left(1 - \frac{1-\rho_r^N}{N(1-\rho_r)}\right)|\mathbb{E}\left[X\right]|^2\right\}\sigma_h^2}. \tag{3.32}$$

A better estimate can be obtained by averaging over all the possible values of m as follows:

$$e^{-j\phi_1} = \frac{\sum_{m=0}^{M_r-2}\mathbb{E}\left[\sum_{n=1}^{N}\frac{y_{0,m}^k[n]}{N}\sum_{n=1}^{N}\frac{(y_{0,m+1}^k)^*[n]}{N}\right]}{\frac{M_r-1}{N}\left\{\mathbb{E}\left[|X|^2\right] + \frac{2\rho_r}{1-\rho_r}\left(1 - \frac{1-\rho_r^N}{N(1-\rho_r)}\right)|\mathbb{E}\left[X\right]|^2\right\}\sigma_h^2}. \tag{3.33}$$

Since this averaging operation over different antenna elements has independent noise terms, the accuracy of the estimate improves with the increasing value of M_r. The root mean square error (RMSE) of the DL AoA as a function of the SNR is shown in Fig. 3.4a. As expected, the RMSE improves with the increasing SNR. The BER performance of the MA receiver over the RMSE values of interest is plotted in Fig. 3.4b. Using a similar method for estimating the AoA of the BL does not result in good RMSE performance, which is mainly attributed to the interference from the DL. Hence, alternate techniques are necessary to accurately estimate the AoA of the BL, and one potential method is to utilize the residual signal from the DL cancellation operation for the AoA estimation. Due to space limitations, it was not possible to include it in this paper and is hence left as a promising future work.

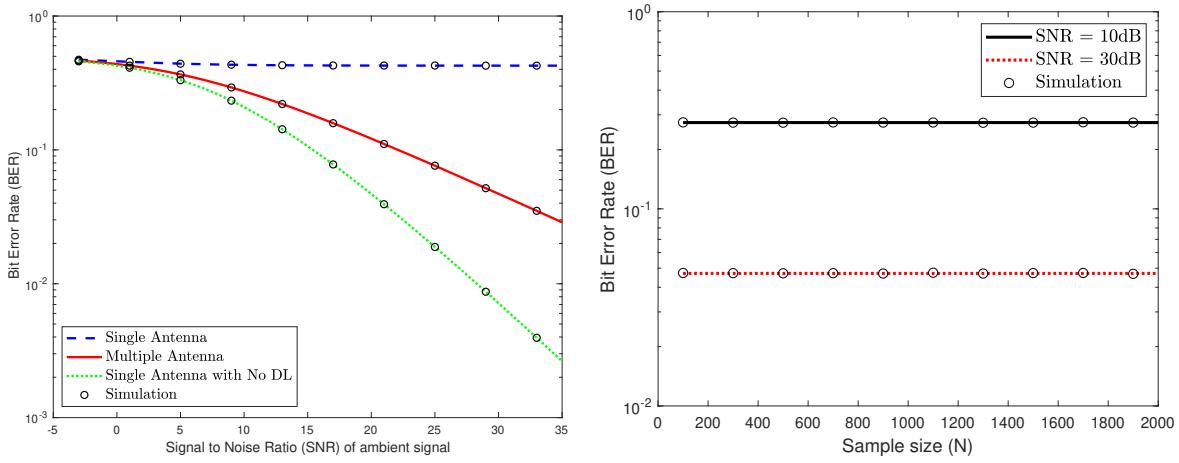

(a) (b)

Figure 3.5: (a) BER comparison of the SA Rx and the MA Rx with $M_r = 2$ under independent fading and/or ambient sequence with $\mathbb{E}[X] = 0$, and comparison of the MA Rx with DL and the SA Rx without DL is also shown. (b) BER performance of the MA Rx with increasing N.

3.6 Numerical Results and Discussion

In this section, the accuracy of our analysis is verified by comparing with Monte-Carlo simulations. In addition, some useful system design insights are also provided. The reflection coefficient Γ_1 is configured appropriately to set the parameter α that will result in a signal attenuation of 1.1 dB, and the variance of the fading gain σ_h^2 is set to 1. The BER performance of the two receivers related to the special cases of independent fading ($\rho = 0$) and/or ambient sequence with zero expectation ($\mathbb{E}[X] = 0$), are compared in Fig. 3.5a. We observe that with increasing SNR, the BER saturates quickly for a SA receiver without any further improvement. This behavior can be attributed to the dependence of a non-coherent detector on differences in the conditional variances of the received symbol. With the strong interference from power source, the variances of the two hypotheses scale similarly with increasing SNR. On the other hand, as shown in Fig. 3.5a, the MA receiver can drastically improve the BER by removing the direct path from the ambient power source. In this case, BER decreases continuously without reaching any error floor. When the interference from the DL is removed in the MA receiver, only the variance of alternate hypothesis scales proportionally to the increasing SNR which ultimately results in the improved BER. Further, the average BER under these two cases is independent of the signal sample size N as shown in Fig. 3.5b. The effectiveness of the proposed DL cancellation technique is verified by comparing the BER of MA and SA receivers with and without the DL interference, respectively. As shown in Fig. 3.5a, performance of the SA receiver without DL is better compared to the MA receiver with DL. This is expected because the BER of the MA receiver is averaged over the joint distribution of AoAs θ_1 and θ_2, and the performance is limited when the AoAs are

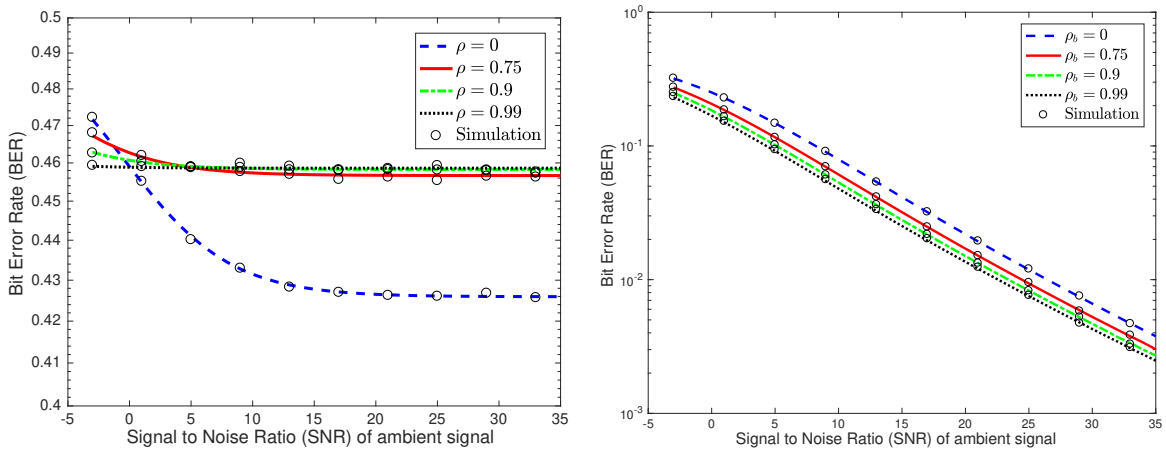

(a) (b)

Figure 3.6: (a) BER performance and the error floor of the SA Rx for different ρ, (b) BER comparison of the MA Rx with $M_r = 9$ for changing ρ_b, and the other parameters configured to $\rho_r = 0.5$ and $\rho_t = \rho_r \rho_b$.

similar.

The results for more general cases are discussed now. Unless specified explicitly for the particular plot, the values of different correlation factors ρ_r, ρ_b, and ρ_t are all considered equal and represented as ρ. The error floor in a SA receiver decreases with correlation factor ρ, as shown in Fig. 3.6a, and it can be inferred that a SA receiver is insufficient for non-coherent detection as the error floor values are very close to 0.5, which corresponds to the BER of a naive hit/miss receiver. From Fig. 3.6a, it can also be verified that the numerically obtained BER floor values of the SA receiver match with the asymptotic BER analytically derived in (3.18). The waterfall curve, as shown in Fig. 3.6b, validates our asymptotic BER analysis presented in (3.27) for the MA receiver with unequal values for different correlation factors. The BER performance with increasing SNR in a MA receiver for different values of the correlation factor ρ is presented in Fig. 3.7a, where it can be seen that the BER improves with increasing ρ. Likewise, the BER performance with increasing sample size N for varying ρ is shown in Fig. 3.7b, and interestingly the BER increases and saturates quickly with increasing N. However, as expected, there is an increasing mismatch between the simulated and theoretical results of BER at lower values of N as the value of ρ is increased. This mismatch occurs due to the need of a larger sample-size N for the averaging operation, so that the simulation and theoretical results converge with increasing ρ. The BER improvement observed with increasing ρ and N can be attributed to the increment in variance of the alternate hypothesis while the variance of the null hypothesis remains constant. The antenna gain achieved with additional antennas is presented in Fig. 3.8a, that shows around 8 dB gain with the doubling of antennas. The simulation result for the analysis in Remark 3.9, corresponding to the additional angular resolution achievable with

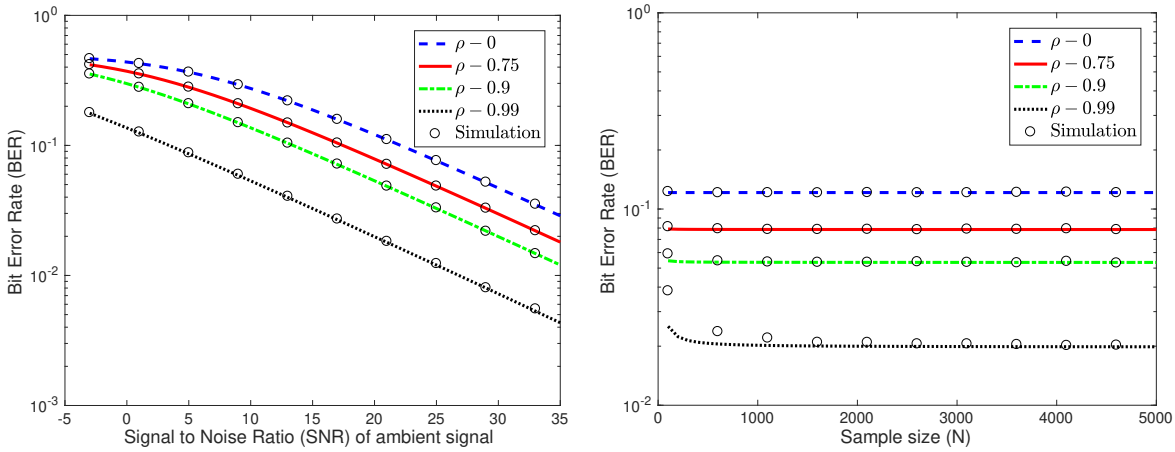

(a) (b)

Figure 3.7: (a) BER vs SNR comparison of the MA Rx with $M_r = 2$ for varying correlation factor ρ and $N = 5000$, (b) BER vs N comparison of the MA Rx with $M_r = 2$ for changing correlation factor ρ with SNR $= 20$ dB.

antennas beyond two, is shown in Fig. 3.8b. For this comparison, one can assume the AoA θ_1 of the DL to be uniformly distributed between $(-\pi, \pi]$, and the AoA θ_2 of the BL to be uniformly distributed with mean θ_1 and width $\Delta\theta = 10°$. The results of the plot demonstrate that while the BER of the dual-antenna Rx is close to 0.5, an antenna gain of around 9 dB is achieved with the doubling of antennas in this case. The comparison between AR and Jakes' channel models discussed in Sec. 3.2.1 is shown in Fig. 3.9a. Two scenarios are considered for comparison: 1) speed of PS and BTx are both 150 kmph, and 2) speed of PS and BTx are both 5 kmph. The corresponding values of the correlation factors for a signal of bandwidth 1.5 KHz turns out to be: 1) $\rho_r = 0.74$, $\rho_b = 0.74$ and $\rho_t = 0.55$, and 2) $\rho_r = 0.99$, $\rho_b = 0.99$ and $\rho_t = 0.99$. The BER performance of our proposed approach for the AR model is similar to that of the Jakes' channel under these two scenarios. We checked many other scenarios and noticed a close match in all of them. We can therefore conclude that the simplified AR model approximates the actual complex time-selective channel very closely, while endowing tractability to the analysis. The approximation can be further improved by using a higher order AR process for modeling the time-selective fading channel. Finally, as shown in Fig. 3.9b, the impact of timing recovery errors is shown to be negligible, which corroborates our timing analysis in Section 3.5.

3.7 Conclusion

Ambient backscatter systems have mainly been studied for low mobility scenarios that are modeled using a block fading channel. While the block fading model is sufficient for stationary environments like home and office, a time-selective fading model is more suitable for non-stationary environments, such as roads and campuses. Therefore, in this paper, we

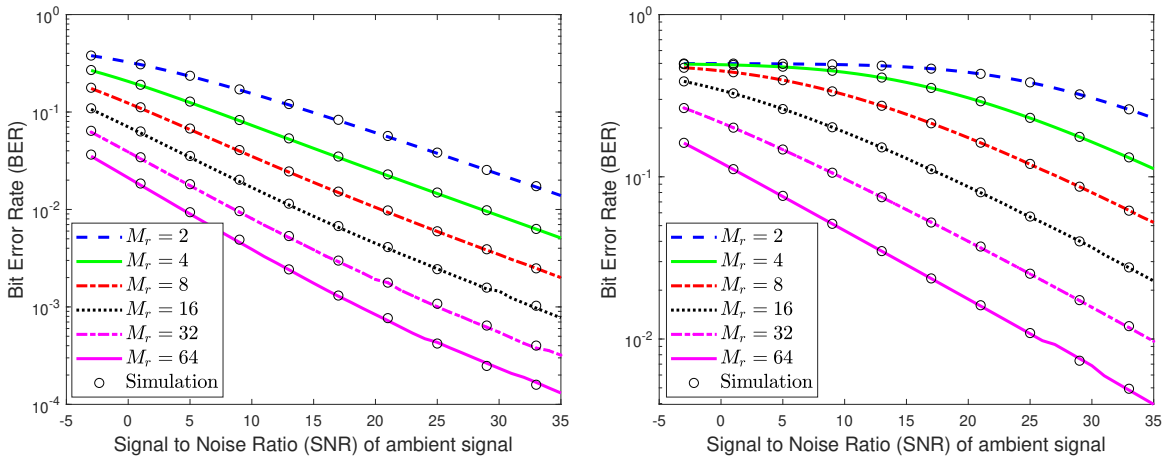

(a) (b)

Figure 3.8: BER vs SNR comparison for changing antenna elements M_r at the receiver with $\rho_r = 0.5, \rho_b = 0.75, \rho_t = 0.38$ and $N = 2000$: (a) uniformly distributed AoAs, and (b) narrowly distributed AoAs.

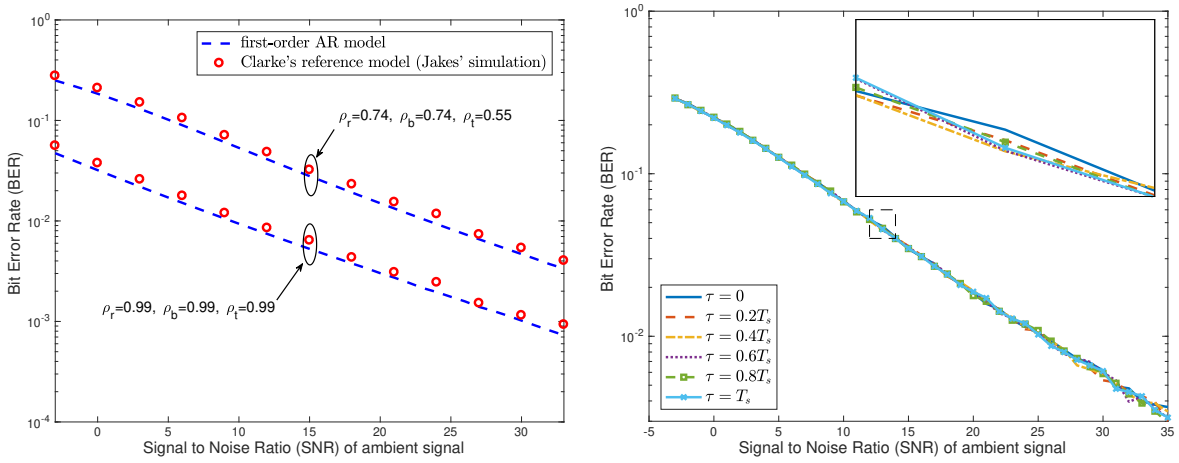

(a) (b)

Figure 3.9: (a) BER performance comparison of AR model channel with that of the channel developed using Jakes' simulation model, and (b) Impact of changing timing error on the BER performance.

have investigated the performance of an ambient backscatter system by studying the design and BER of a non-coherent detector under time-selective fading channels. To the best of our knowledge, this is the first work that has incorporated both non-coherent detection and time-selective fading into the ambient backscatter setup. Unlike the conventional architecture, which is implemented using the average of the energy of the received signal samples, a new receiver architecture based on the direct average of the signal samples is proposed. The new architecture is simpler to implement, robust to timing errors, and lends tractability to the asymptotic analysis. We have shown in the analysis that a BER floor exists for the SA receiver due to the DL interference of the ambient power source, thereby resulting in an unacceptable performance. The BER is drastically improved using a MA receiver by tracking the AoA of the DL and using it to eliminate the interference. Further, having more than two receive antennas allows additional angular resolution, which can support applications where the AoAs of the DL and BL links are very close. Though the BER in the time-selective fading improves with increasing signal sample-size, it saturates to an asymptotic value. Additionally, the BER is observed to improve with increasing temporal-correlation of the fading channel. By comparing the BER, the simple first-order AR process is shown to be an effective approximation of the Clarke's reference model available for the time-selective fading channel. A natural extension of this work is to implement an ambient backscatter system that can function in a channel with multiple angular paths at the receiver. In the next chapter, we look at the problem of encoding in ambient backscatter, and demonstrate the advantages of utilizing coding schemes for the message data before the symbol modulation and transmission.

Chapter 4

Manchester Encoding for Non-coherent Detection of Ambient Backscatter in Time-Selective Fading

4.1 Introduction

In Chapter 3, we have seen the advantages of deploying multiple antennas at the receiver that is reflected in the bit error rate (BER) improvement of the system. Similarly, in this chapter we look at the advantages of employing Manchester encoding at the transmitter side for non-coherent detection by deriving the optimal decision rule and the BER expressions. Due to the difficulty of acquiring channel state information (CSI) for fast varying channels, it might be detrimental to build an ambient backcatter system based on coherent communication, and could be more beneficial to choose non-coherent transmission as the preferred mode of communication in such channels. It is, therefore, very important to improve the performance of non-coherent detection for the ambient backscatter to accelerate its widespread adoption and implementation for applications that experience fast varying channels, such as the vehicular communications systems. Towards this goal, we investigate the advantages of employing Manchester encoding for the non-coherent transmission of ambient backscatter symbols under a time-selective fading setup. We show that this encoding scheme reduces the detection complexity at the receiver, while improving the BER performance compared to the popular on-off keying (OOK) modulation.

Related Work: With respect to the assumptions about the channel model, the current literature on non-coherent ambient backscatter can be broadly divided into two categories. The first category belongs to slow fading channels, for which the non-coherent receiver designs based on maximum-likelihood (ML) detection [15], semi-coherent detection [14], and orthogonal frequency division multiplexing (OFDM) [62, 88] are proposed. Also, the blind channel estimation techniques that do not require transmission of separate pilot signals are studied in [64, 65] for the ambient backscatter setup. Manchester encoding was first explored in [63] for a slow fading ambient backscatter setup. In [89], the angle of arrival (AoA) estimation using a reader with a massive number of antennas is explored for the ambient backscatter setup. The second category relates to the time-selective fading channels, which is of more interest to us but has not received much attention. The most relevant prior art in this direction is our own work [25], which focuses on the non-coherent multi-antenna re-

ceiver design for direct OOK modulation. However, the bit error rate (BER) analysis of the ambient backscatter systems under Manchester encoding and time-selective fading is an open problem, which is solved in this paper. A particular technical novelty of the paper is in carefully handling the correlation between the test statistics corresponding to the two codewords of the encoded symbol, which is crucial for the exact BER analysis.

Contributions: In this work, we introduce Manchester encoding to the time-selective fading setup of an ambient backscatter system, and analyze the performance of the scheme. We also determine the advantages of Manchester encoding over the direct OOK modulation by comparing the complexity of the two detection mechanisms and their BER performance. A low-complexity receiver architecture based on the direct averaging of the received signal samples is considered for the setup. This architecture diverges from the conventional one based on the averaging of energy of the received signal samples, which is commonly used in the ambient backscatter literature [20]. The main contributions of our current work can be summarized as follows: 1) evaluation of the conditional joint distributions and the average BER of Manchester encoding for both the single antenna (SA) and multi-antenna (MA) receivers, and 2) novel analysis that demonstrates the advantages of Manchester encoding over the popular direct OOK modulation. To be exact, we analytically show that the optimal detection rule of the ambient backscatter with Manchester encoding is independent of the system and channel parameters, which greatly simplifies the receiver implementation. In addition, the encoding scheme also results in an SNR gain over the direct OOK modulation, when used in conjunction with an MA receiver implementing the direct-link (DL) cancellation. The exact gain in SNR is dependent on the joint distribution of the AoAs of the DL and backscatter link (BL). For the uniform spread and narrow spread joint distributions of the AoAs considered in our work, the SNR gain comes out to be around 4 dB and 3 dB, respectively.

4.2 System Model

The setup for the ambient backscatter system mainly consists of three devices, namely the ambient power source (PS), the backscatter transmitter (BTx), and the receiver (Rx). The ambient PS and BTx are surrounded by local scatterers resulting in independent subpaths with uniformly distributed angle of departure (AoD), while the Rx only has dominant scatterers that are far away, resulting a narrow spread for the AoA. Hence, the signal at Rx can be modeled as spatially correlated with two receive links, namely DL and BL that arrive at AoAs θ_1 and θ_2, respectively, after propagating through a flat Rayleigh fading channel. The described system setup of the ambient backscatter is illustrated in Fig. 4.1. In addition, the ambient PS and BTx could be in motion independently of each other, resulting in a time-varying channel. Under the local scattering assumptions, the auto-correlation function (ACF) for the fading process of the DL and BL links is given by $J_0(2\pi f_d t_d)$, where $J_0()$ is the zero order Bessel function of the first kind, f_d is the maximum Doppler spread (DS) of the link and t_d is the delay [76]. Similarly, the ACF for the PS-BTx link is given by

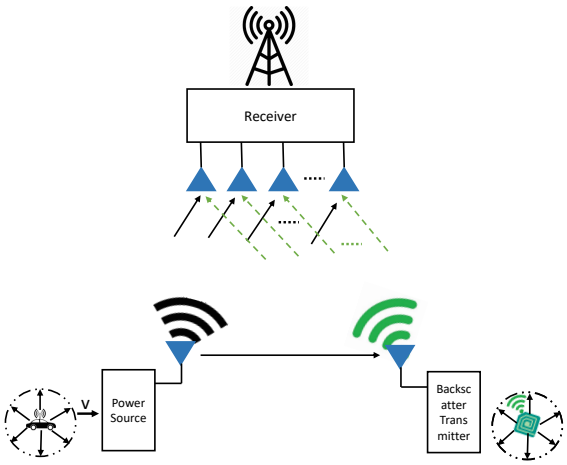

Figure 4.1: System model for the ambient backscatter setup.

$J_0(2\pi f_d t_d)J_0(2\pi a f_d t_d)$, where a is the ratio of the DS present at these two devices of the link [76]. For tractability, the temporal fading of each link is modeled as a first-order AR process given by $h[n]=\rho h[n-1]+\sqrt{1-\rho^2}g[n]$, where $h[n]$ and $h[n-1]$ are the gains of the current and previous time instants, respectively, $g[n]$ is the complex Gaussian process of variance σ_h^2, and $\rho \in [0,1)$ is the correlation factor [78]. Depending on the link, the value of ρ is given by either $J_0(2\pi f_d T_s)$ or $J_0(2\pi f_d T_s)J_0(2\pi a f_d T_s)$, where T_s is the symbol duration. The MA receiver of the current setup utilizes the slow varying rate of the large scale parameter AoA, in comparison to varying rate of the overall channel gain of the fading channel, to track the AoA of the DL and cancel its interference [25].

By intentionally keeping the data rate of backscatter lower compared to that of the ambient data, the signal at the SA receiver can be expressed as:

$$y[n] = h_r[n]x[n] + \alpha b\, h_b[n]\, h_t[n]x[n] + w[n], \tag{4.1}$$

where $x[n]$ is the ambient data sequence, $w[n]$ is the additive Gaussian noise, $h_r[n], h_b[n]$ and $h_t[n]$ are i.i.d. zero mean complex Gaussian channel coefficients with variance σ_h^2 and are unknown at Rx, b is the backscatter data bit, and α is related to the parameter Γ_1 (the reflection coefficient of the tag when bit '1' is transmitted) of the BTx node. The channel coefficients $h_r[n], h_b[n]$ and $h_t[n]$ are modeled using a first-order AR process, each having a separate correlation factor ρ_r, ρ_b, and ρ_t, respectively. Similarly, the resultant signal at the MA receiver after the DL cancellation is given by:

$$\tilde{\mathbf{y}}[n] = \tilde{\mathbf{a}}\, \alpha b\, h_b[n]h_t[n]x[n] + \tilde{\mathbf{w}}[n], \tag{4.2}$$

where the resultant vectors $\tilde{\mathbf{a}}$ and $\tilde{\mathbf{w}}[n]$ are given by:

$$\tilde{\mathbf{a}} = \begin{bmatrix} 2\sin(\frac{\phi_2-\phi_1}{2})e^{j(\frac{\phi_2-\phi_1}{2})} \\ \vdots \\ 2\sin(M_r-1)(\frac{\phi_2-\phi_1}{2})e^{j(M_r-1)(\frac{\phi_2-\phi_1}{2})} \end{bmatrix}, \tilde{\mathbf{w}}[n] = \begin{bmatrix} e^{-j\phi_1}w_1[n] - w_0[n] \\ \vdots \\ e^{-j(M_r-1)\phi_1}w_{M_r-1}[n] - w_0[n] \end{bmatrix}. \tag{4.3}$$

The phase offset ϕ_i of each link is given by $\frac{2\pi}{\lambda} d \cos\theta_i$. Additional details on the setup, channel and signal model can be found in [25]. However, unlike the direct OOK modulation used in [25], the transmitter in this case sends out codewords [0 1] and [1 0], known as Manchester coding, using the OOK modulation for message (b) bits 0 and 1, respectively. For completeness, note that a preliminary study of Manchester encoding appears in our conference paper [84], which is limited to a dual-antenna receiver and assumed independent fading across the ambient symbols. For a fair comparison with the direct OOK modulation, we assume that each codeword of Manchester encoding is sent within a single symbol duration of the backscatter data instead of the time duration of two symbols. The test statistics (TSs) Z_0 and Z_1 are evaluated for the two symbols of the codeword by taking half the samples each from the sample size N, and are given by $Z_0 = \frac{2}{N}\sum_{n=1}^{N/2} y[n]$ and $Z_1 = \frac{2}{N}\sum_{n=N/2+1}^{N} y[n]$. Although the setup of the paper is inspired by [25], the new analysis for Manchester encoding under time-selective fading channel is fundamentally different and non-trivial due to correlation between the two variables Z_0 and Z_1.

4.3 Detection at the Single Antenna Receiver

In this section, we evaluate the performance of Manchester encoding in the SA receiver by deriving the conditional probability density functions (PDFs) and BER of the receiver. In this work, the BER probability of the detector is represented using one of the commonly used notations $P(e)$, where e is the bit error event.

4.3.1 Conditional Distributions of the Signal

The null and alternate hypotheses $\mathcal{H}_0$ and $\mathcal{H}_1$ of the encoding scheme correspond to the backscatter bit $b \equiv 0$ and $b \equiv 1$, respectively. Since the transmitter sends out codewords, we have to derive the joint conditional distributions of the TSs Z_0 and Z_1 evaluated for each symbol of the codeword.

Lemma 4.1. *The joint PDFs of Z_0 and Z_1 conditioned on $\mathcal{H}_0$ and $\mathcal{H}_1$ for Manchester encoding in SA receiver are given by:*

$$\mathcal{H}_0 : f_{Z_0,Z_1}(z_0,z_1) = \frac{\exp\left\{-\left(\frac{|z_0|^2\mathrm{Var}_1^{\mathrm{SA}}+|z_1|^2\mathrm{Var}_0^{\mathrm{SA}}-(z_0z_1^*+z_0^*z_1)\mathrm{Cov}^{\mathrm{SA}}}{\mathrm{Var}_0^{\mathrm{SA}}\mathrm{Var}_1^{\mathrm{SA}}-\left(\mathrm{Cov}^{\mathrm{SA}}\right)^2}\right)\right\}}{\pi^2\left(\mathrm{Var}_0^{\mathrm{SA}}\mathrm{Var}_1^{\mathrm{SA}}-\left(\mathrm{Cov}^{\mathrm{SA}}\right)^2\right)}, \tag{4.4}$$

$$\mathcal{H}_1 : f_{Z_0,Z_1}(z_0,z_1) = \frac{\exp\left\{-\left(\frac{|z_0|^2\mathrm{Var}_0^{\mathrm{SA}}+|z_1|^2\mathrm{Var}_1^{\mathrm{SA}}-(z_0z_1^*+z_0^*z_1)\mathrm{Cov}^{\mathrm{SA}}}{\mathrm{Var}_0^{\mathrm{SA}}\mathrm{Var}_1^{\mathrm{SA}}-\left(\mathrm{Cov}^{\mathrm{SA}}\right)^2}\right)\right\}}{\pi^2\left(\mathrm{Var}_0^{\mathrm{SA}}\mathrm{Var}_1^{\mathrm{SA}}-\left(\mathrm{Cov}^{\mathrm{SA}}\right)^2\right)}, \tag{4.5}$$

where $\mathrm{Var}_0^{\mathrm{SA}} = \frac{2(\sigma_h^2\mathbb{E}\left[|X|^2\right]+\sigma_h^2\frac{2\rho_r}{1-\rho_r}(1-\frac{2(1-\rho_r^{N/2})}{N(1-\rho_r)})|\mathbb{E}[X]|^2+\sigma_n^2)}{N}$, $\mathrm{Cov}^{\mathrm{SA}} = \frac{4\rho_r\left(1-\rho_r^{N/2}\right)^2}{N^2(1-\rho_r)^2}|\mathbb{E}[X]|^2$, *and*

$$\mathrm{Var}_1^{\mathrm{SA}}=\frac{2}{N}(\sigma_h^2(1+|\alpha|^2\sigma_h^2)\mathbb{E}\left[|X|^2\right]+\sigma_h^2\Big[\frac{2\rho_r}{1-\rho_r}(1-\frac{2(1-\rho_r^{N/2})}{N(1-\rho_r)})$$
$$+|\alpha|^2\sigma_h^2\frac{2\rho_t\rho_b}{1-\rho_t\rho_b}(1-\frac{2(1-\rho_t^{N/2}\rho_b^{N/2})}{N(1-\rho_t\rho_b)})\Big]|\mathbb{E}[X]|^2+\sigma_n^2).$$

Proof: See Appendix C.1. ■

4.3.2 Bit Error Rate

The conditional PDFs of Z_0 and Z_1 under the two hypotheses are compared to derive the optimal threshold, which is used to evaluate the BER of the SA receiver.

Theorem 4.2. *The average BER of Manchester encoding in the SA receiver is given by:*

$$P_{\mathrm{SA}}(e) = \int_0^{\infty}\int_v^{\infty} \frac{\exp\left\{-\left(\frac{u}{(1-\rho^2)\mathrm{Var}_0^{\mathrm{SA}}}+\frac{v}{(1-\rho^2)\mathrm{Var}_1^{\mathrm{SA}}}\right)\right\}}{\pi(1-\rho^2)\mathrm{Var}_0^{\mathrm{SA}}\mathrm{Var}_1^{\mathrm{SA}}} \times I_0\left(\frac{\rho\sqrt{uv}}{(1-\rho^2)\sqrt{\mathrm{Var}_0^{\mathrm{SA}}\mathrm{Var}_1^{\mathrm{SA}}}}\right)\mathrm{d}u\,\mathrm{d}v, \tag{4.6}$$

where I_0 *is zeroth order modified Bessel function of the first kind. The expression in* (4.6) *can be well approximated as*

$$P_{\mathrm{SA}}(e) = \left(1+\frac{\mathrm{Var}_1^{\mathrm{SA}}}{\mathrm{Var}_0^{\mathrm{SA}}}\right)^{-1} \tag{4.7}$$

for large values of the sample size N*, since the two variances* $\mathrm{Var}_0^{\mathrm{SA}}$ *and* $\mathrm{Var}_1^{\mathrm{SA}}$ *both decay at the rate of* $\Theta(N^{-1})$ *while the covariance* $\mathrm{Cov}^{\mathrm{SA}}$ *decays at the rate of* $\Theta(N^{-2})$*.*

Proof: See Appendix C.2. ■

Asymptotic analysis

The ratio of the variances of the null and alternate hypotheses of the SA receiver is

$$K = 1 + \frac{|\alpha|^2\sigma_h^4\left\{1+\frac{2\rho_t\rho_b}{1-\rho_t\rho_b}(1-\frac{2(1-\rho_t^{N/2}\rho_b^{N/2})}{N(1-\rho_t\rho_b)})\frac{|\mathbb{E}[X]|^2}{\mathbb{E}[|X|^2]}\right\}}{\sigma_h^2\left\{1+\frac{2\rho_r}{1-\rho_r}(1-\frac{2(1-\rho_r^{N/2})}{N(1-\rho_r)})\frac{|\mathbb{E}[X]|^2}{\mathbb{E}[|X|^2]}\right\}+\mathrm{SNR}^{-1}}.$$

The asymptotic BER of Manchester encoding in the SA receiver is given by:

$$P_{\mathrm{SA}}^{\mathrm{asym}}(e) = \lim_{\mathrm{SNR}\to\infty}(1+K)^{-1} = \left(2+\frac{|\alpha|^2\sigma_h^4+|\alpha|^2\sigma_h^4\frac{2\rho_t\rho_b}{1-\rho_t\rho_b}(1-\frac{2(1-\rho_t^{N/2}\rho_b^{N/2})}{N(1-\rho_t\rho_b)})\frac{|\mathbb{E}[X]|^2}{\mathbb{E}[|X|^2]}}{1+\frac{2\rho_r}{1-\rho_r}(1-\frac{2(1-\rho_r^{N/2})}{N(1-\rho_r)})\frac{|\mathbb{E}[X]|^2}{\mathbb{E}[|X|^2]}}\right)^{-1}.$$

Remark 4.3. It is important to highlight the advantages of Manchester encoding over the direct OOK modulation. The decision rule, given in (C.2), for Manchester encoding is just a function of the relative magnitudes of the two RVs Z_0 and Z_1. On the other hand, the decision rule of the direct OOK modulation is based on the comparison of the magnitude of a single TS Z (evaluated over all the N samples) with a threshold, which can be expressed as follows:

$$|z|^2 \gtrless_0^1 \ln(\frac{s_1}{s_0})\frac{s_1 s_0}{s_1 - s_0}, \tag{4.8}$$

where $s_0 = \frac{(\sigma_h^2\mathbb{E}\left[|X|^2\right]+\sigma_h^2\frac{2\rho_r}{1-\rho_r}(1-\frac{(1-\rho_r^N)}{N(1-\rho_r)})|\mathbb{E}[X]|^2+\sigma_n^2)}{N}$ and

$$s_1=\frac{1}{N}(\sigma_h^2(1+|\alpha|^2\sigma_h^2)\mathbb{E}\left[|X|^2\right]+\sigma_h^2\Big[\frac{2\rho_r}{1-\rho_r}(1-\frac{(1-\rho_r^N)}{N(1-\rho_r)}) + |\alpha|^2\sigma_h^2\frac{2\rho_t\rho_b}{1-\rho_t\rho_b}(1-\frac{(1-\rho_t^N\rho_b^N)}{N(1-\rho_t\rho_b)})\Big]|\mathbb{E}\left[X\right]|^2+\sigma_n^2).$$

The optimal decision rule for the direct OOK modulation is a function of the system parameters such as the SNR of ambient signal, the fading variance σ_h^2, the sample size N, and the correlation factors ρ_r, ρ_b and ρ_t [25]. Hence, this scheme considerably reduces the receiver complexity, and will most likely be preferred for the cases where optimizing the energy consumption of the device is a priority.

Even though the optimal decision rule is simplified with Manchester encoding, the asymptotic BER still suffers from an error floor. Therefore, the performance of the encoding scheme in the MA receiver needs to be evaluated to demonstrate its full potential. In the next section, we discuss the antenna gain, detection procedure and the BER performance of the MA receiver when Manchester encoding is employed at the backscatter transmitter.

4.4 Detection at the Multi-Antenna Receiver

The effective signal obtained after the DL cancellation, and proper weighting of the resultant signal vector in the MA receiver is given by [25]:

$$y_{\text{eff}}[n] = \mathbf{r}^*\tilde{\mathbf{a}}\alpha b\, h_b[n]h_t[n]x[n] + \mathbf{r}^*\tilde{\mathbf{w}}[n], \tag{4.9}$$

where $\mathbf{r} = \frac{\hat{\mathbf{K}}_{\tilde{\mathbf{W}}}^{-1}\tilde{\mathbf{a}}}{|\hat{\mathbf{K}}_{\tilde{\mathbf{W}}}^{-\frac{1}{2}}\tilde{\mathbf{a}}|}$ is the weight vector with the optimal MMSE detection. The antenna gain $G = \tilde{\mathbf{a}}^*\hat{\mathbf{K}}_{\tilde{\mathbf{W}}}^{-1}\tilde{\mathbf{a}}$ due to multiple antennas is given by [25]:

$$G = M_r - \frac{1}{M_r} - \frac{2}{M_r}\frac{\sin((M_r-1)\frac{\phi_2-\phi_1}{2})}{\sin(\frac{\phi_2-\phi_1}{2})}\cos(M_r\frac{\phi_2-\phi_1}{2}) - \frac{1}{M_r}\frac{\sin^2((M_r-1)\frac{\phi_2-\phi_1}{2})}{\sin^2(\frac{\phi_2-\phi_1}{2})},$$

and the expression can be further simplified as follows:

$$G = M_r - \frac{1}{M_r}\frac{\sin^2(M_r\frac{\phi_2-\phi_1}{2})}{\sin^2(\frac{\phi_2-\phi_1}{2})}. \tag{4.10}$$

Although the antenna gain is a function of the two phase offsets (and thereby the AoAs), it is represented as a single variable G without any arguments to simplify the notation.

The exact expression of the average BER is dependent on the joint distribution of the two variables θ_1 and θ_2. For further exposition, we consider two kinds of distributions: 1) *uniform spread of AoAs:* the two AoAs θ_1 and θ_2 are independent and uniformly distributed between $(-\pi, \pi]$, and 2) *uniform spread of AoAs:* the AoA θ_1 is uniformly distributed between $(-\pi, \pi]$ while θ_2 is uniformly distributed with mean equal to the value of θ_1 and some angular spread (considered to be 10°).

Theorem 4.4. *The average BER of Manchester encoding in the MA receiver with uniform spread of the two AoAs is given by:*

$$P_{\text{MA}}(e) = \int_{-\pi}^{\pi}\int_{-\pi}^{\pi}\frac{1}{2\pi}\times\frac{1}{2\pi}\frac{\sigma_n^2}{G|\alpha|^2\sigma_h^4\left\{\mathbb{E}[|X|^2]+\frac{2\rho_t\rho_b}{1-\rho_t\rho_b}\left(1-\frac{2(1-\rho_t^{\frac{N}{2}}\rho_b^{\frac{N}{2}})}{N(1-\rho_t\rho_b)}\right)|\mathbb{E}[X]|^2\right\}+2\sigma_n^2}\mathrm{d}\theta_1\mathrm{d}\theta_2. \tag{4.11}$$

Proof: See Appendix C.3. ∎

Asymptotic analysis

The ratio of the variances of the null and alternate hypotheses of the MA receiver is

$$K = 1+G|\alpha|^2\sigma_h^4\left\{1+\frac{2\rho_t\rho_b}{1-\rho_t\rho_b}\left(1-\frac{2(1-\rho_t^{N/2}\rho_b^{N/2})}{N(1-\rho_t\rho_b)}\right)\frac{|\mathbb{E}[X]|^2}{\mathbb{E}[|X|^2]}\right\}\text{SNR}.$$

The asymptotic conditional BER of the Manchester encoding in the MA receiver is given by:

$$P_{\text{MA}}^{\text{asym}}(e|\phi_1,\phi_2) = \lim_{\text{SNR}\to\infty}(1+K)^{-1} = \frac{\text{SNR}^{-1}}{G|\alpha|^2\sigma_h^4\left\{1+\frac{2\rho_t\rho_b}{1-\rho_t\rho_b}\left(1-\frac{2(1-\rho_t^{\frac{N}{2}}\rho_b^{\frac{N}{2}})}{N(1-\rho_t\rho_b)}\right)\frac{|\mathbb{E}[X]|^2}{\mathbb{E}[|X|^2]}\right\}+2\text{SNR}^{-1}} = 0.$$

4.5 Numerical Results and Discussion

We now compare the BER performance of Manchester encoding with the direct OOK modulation. In addition, the analytical results are compared with Monte-Carlo simulation to verify the accuracy of our analysis. The value of α is configured to result in a signal

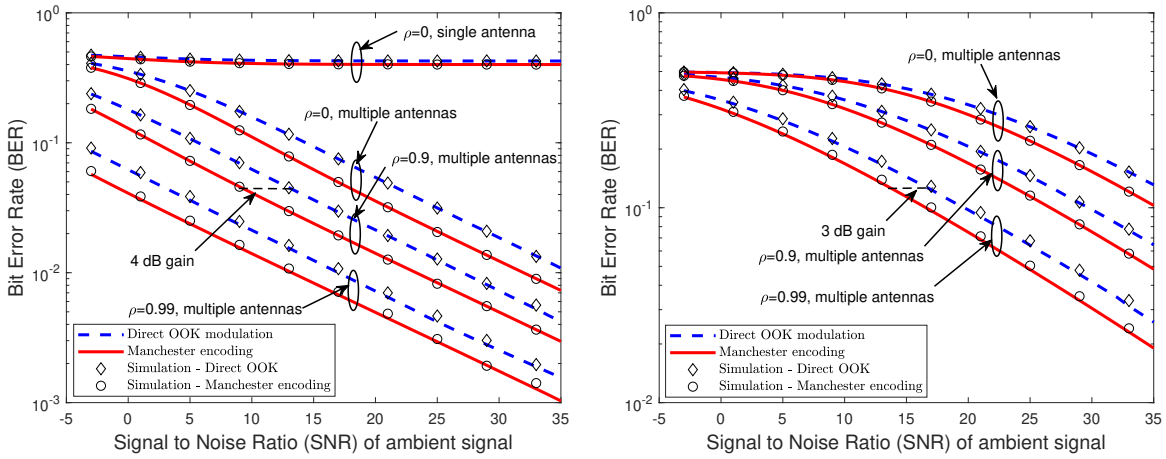

(a) (b)

Figure 4.2: BER vs SNR comparison of Manchester encoding and the direct OOK modulation for varying correlation factor ρ, $M_r = 4$ and $N = 2000$: (a) uniform spread of AoAs, (b) narrow spread of AoAs.

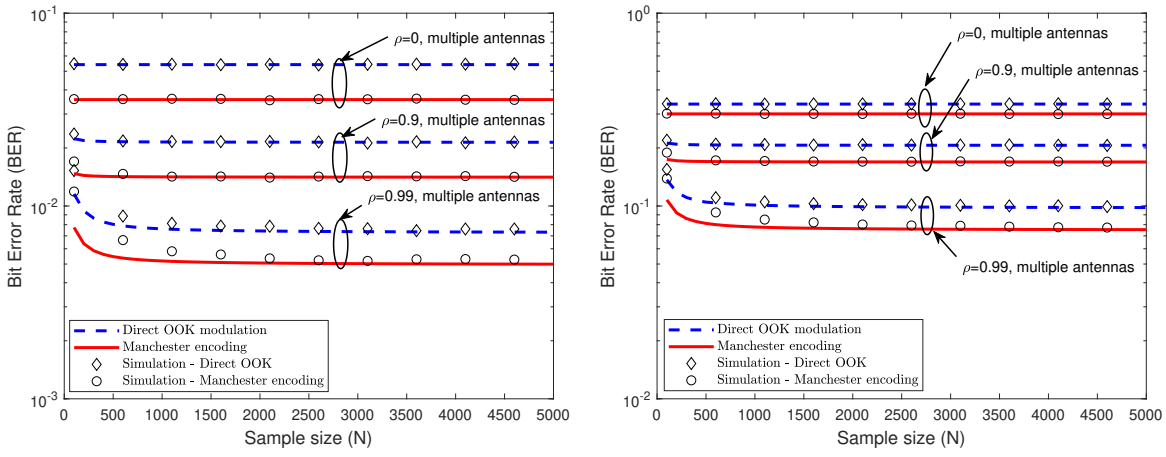

(a) (b)

Figure 4.3: BER vs N comparison of Manchester encoding and the direct OOK modulation for varying correlation factor ρ, $M_r = 4$, and SNR $= 20$ dB: (a) uniform spread of AoAs, (b) narrow spread of AoAs.

attenuation of 1.1 dB, while the variance of the channel gains σ_h^2 is set to 1. The values of all the correlation factors ρ_r, ρ_b and ρ_t are assumed to be the same, and are represented using another variable ρ. First, we discuss the average BER results for the uniformly spread AoAs before comparing with the performance under narrowly spread AoAs. The BER result of the uncoded and coded schemes of the SA receiver for the independent fading scenario ($\rho = 0$) is shown in Fig. 4.2a, and it can be verified from the plot that both of the schemes suffer from an error floor which can be attributed to the DL interference. In the same Fig. 4.2a, the BER results of the MA receiver for the two schemes with varying values of the correlation factor ρ are also plotted. The effect of the DL cancellation on the performance can be inferred from the improved BER of the two schemes. It can also be verified from the figure that Manchester encoding results in an SNR gain of around 4 dB over the uncoded direct OOK modulation for the uniformly spread AoAs. In comparison, the SNR gain of the Manchester encoding over the uncoded OOK modulation obtained for the narrowly spread AoAs is around 3 dB, as shown in Fig. 4.2b. As expected, the exact SNR gain with the Manchester encoding is dependent on the joint distribution of the two AoAs but remains constant for different values of ρ. In addition, the BER curves of the two schemes with increasing sample-size N for the uniformly spread and narrow spread AoAs are respectively plotted in Figs. 4.3a and 4.3b, which are flat beyond a threshold value of N. The mismatch between the theoretical and simulation results for small N is due to the requirement of minimum number of samples for the averaging operation to work properly, and larger number of samples are required with increasing value of the correlation factor ρ.

4.6 Summary

In this work, we have analyzed the impact of Manchester encoding on non-coherent transmission with respect to an ambient backscatter system under time-selective fading, where we have analytically and numerically shown the advantages of the scheme over the conventional direct OOK modulation used in the literature. The optimal decision rule for Manchester encoding is only dependent on the relative magnitude of the test statistic for the two symbols of the codeword, and hence the optimal detection threshold turns out to be independent of all the system parameters. In addition, the proposed encoding scheme also achieves an SNR gain over the direct OOK modulation with the MA receiver, the exact value of which will vary based on the joint distribution of the two AoAs. In our analysis, the SNR gain evaluated for the uniformly and narrowly spread AoAs came to be around 4 dB and 3 dB, respectively, which is a substantial improvement in the performance of the ambient backscatter system. Until now, our main focus is on characterizing the BER performance of ambient backscatter in a point-to-point link system. In the next and final technical chapter, we study the problem of determining the performance of ambient backscatter in a large-scale network by incorporating the effect of co-channel interferers using ideas from stochastic geometry.

Chapter 5

Bit Error Rate of Frequency-Shift Ambient Backscatter with Non-Coherent Detection in a Large-scale Network

5.1 Introduction

In this chapter, we consider the problem of characterizing the performance of ambient backscatter in a large-scale network. In particular, we analyze the performance of a technique known as frequency-shift backscatter in the presence of an interference field modeled as a Poisson point process (PPP). Frequency-shift backscatter is the preferred mechanism to overcome self-interference from the source signal since it has shown good potential in improving the performance with a weak signal of backscatter systems [9,28,90]. However, these systems have to deal with the interference from devices already occupying the new band which can also limit their performance. On the other hand, our earlier studies have shown that non-coherent detection can easily extend the deployment of the ambient backscatter systems to multiple use case scenarios including time varying channels [25, 26]. The non-coherent systems in ambient backscatter mainly suffer from bit error rate (BER) floor resulting from the high interference of the direct link coming from the power source. Motivated by our earlier studies which indicate that the performance of the ambient backscatter can be improved by spatially separating the signals of the backscatter nodes and the ambient source devices, we consider the problem of analyzing the performance of frequency-shift ambient backscatter in this particular work [25, 26]. In particular, we evaluate the BER of non-coherent based frequency-shift ambient backscatter under the two following network setups: 1) a single interfering signal coming from the ambient transmission occurring in the shifted frequency band, and 2) a large scale network with multiple interfering signals coming from the backscatter nodes and ambient source devices transmitting in the band of interest. Using tools from stochastic geometry, the interfering devices in the large-scale network are modeled as a two dimensional PPP and the sum-product functional properties of the PPP are used to evaluate the BER for the large-scale network. The wireless channel is assumed to be a slow fading channel with spatial correlation present at the receiver node.

5.1.1 Related Work

Most of the literature on ambient backscatter is related to coherent and semi-coherent detection techniques [1,12,14–16,18,20], which are however not always feasible to implement in practice. For example, consider the time selective channels where due to constant evolving of the fading gain with time the non-coherent detectors are preferred for their ease of implementation. On the other hand, the existing literature on non-coherent detection of ambient backscatter is very limited [15,25,26,62,63,65,91]. One of the earliest works to study non-coherent signal detection for ambient backscatter is [15]. Our earlier work has investigated the role of multiple antennas in improving the BER performance of a non-coherent system under a time-varying fading channel [25]. Coding schemes such as Manchester encoding to further improve the performance of the non-coherent detection are explored in [26,63]. On the same lines, non-coherent detection over ambient orthogonal frequency division multiplexing (OFDM) and cognitive radio network setups are investigated in [62] and [65], respectively. The frequency shifting method of the backscatter signal to a non-overlapping band to avoid the self interference is investigated in multiple studies [3,9,10,27–29]. Our work can be easily differentiated from the prior art on non-coherent detection as the main focus of the analysis is on the BER of the frequency-shift ambient backscatter in a large-scale network.

The error performance in a large-scale network can be studied by modeling the spatial distribution of devices as a random process and using tools from stochastic geometry to evaluate the BER metric [92,93]. However, the available literature on the stochastic geometry application to ambient backscatter is exclusively limited to the power outage and coverage analysis [30–41]. The analysis of a large-scale backscatter network was first considered in [30], where the backscatter nodes use devices known as power beacons (PBs) for both harvesting energy and transmitting the backscatter data. The spatial deployment of PBs is modeled using a homogeneous Poisson point process (PPP), while the backscatter nodes are clustered around the parent PBs using Poisson cluster process (PCP). The investigation into the dyadic channel of backscatter is considered in [31], where the coverage probability of a binomial point process (BPP) modeled network with physical layer mechanisms such as space division multiple access (SDMA), ultra-narrowband (UNB) transmissions, and successive interference cancellation (SIC) is analyzed. Similarly, [32] studied the coverage probability of the dyadic backscatter network modeled using a homogeneous PPP. In [33], the authors have analyzed the coverage probability of the primary network in the presence of a secondary backscatter network. The analysis for a hybrid harvest-then-transmit (HTT) and ambient backscatter node is presented in [34] by modeling the distribution of the two primary networks as independent α-Ginibre point processes (α-GPPs). Along the same lines, the coverage analysis for a hybrid node deployment modeled as a PCP is performed in [35]. In [38], the impact of time-switching/power-splitting architectures and non-linear harvesting model for the backscatter nodes on the outage probability is investigated. The coverage analysis of a hybrid relay node with backscatter mode is explored in [37]. In another work [36], the coverage probability of a drone assisted BPP backscatter network is investigated. A temporal-space PPP model is developed in [41] to study the outage probability of an

asynchronous backscatter network with sporadic transmissions. One limitation of all these studies is that none of them have considered the BER metric for characterizing the performance of ambient backscatter in a network. The work presented in this chapter is the first such study that comprehensively tackles the problem of BER characterization of ambient backscatter in a large-scale network.

5.1.2 Contributions

In this chapter, a comprehensive treatment of the frequency-shift ambient backscatter is presented by investigating the performance of the system under two types of network setups: 1) a single interference signal coming from the ambient transmission occuring in the shifted frequency band, and 2) a large scale network with multiple interference signals coming from the backscatter nodes and ambient source devices transmitting in the band of interest. The ambient backscatter communication is considered to be performed non-coherently, and two types of receivers are considered for the non-coherent setup: a) single antenna (SA) receiver and b) multi-antenna (MA) receiver. In the single interfering link system, we mainly look at the impact of small-scale fading on the backscatter performance whereas the effect of large-scale path loss on the performance is analyzed when analyzing the large-scale network. Tools from stochastic geometry are used to perform this analysis. The interfering devices are assumed to be modeled as a PPP, which endows tractability to this analysis while capturing the inherent irregularity in the placement of these devices.

Insights Our analysis for the single interference link system shows that the multi-antenna receiver can remove the BER floor observed in case of the single antenna receiver by tracking the angle-of-arrival (AoA) of the interference link, and use it to cancel the interference from the ambient device which drastically improves the performance. One important observation is that the BER improvement for block fading channel is found to be a bit larger compared to the improvement seen for time-selective fading [84]. In the process of deriving the conditional distributions for the null and alternate hypotheses, we come across a generalized sum sequence with correlation between the samples. For the sum sequence, we derive the asymptotic growth rate which is then applied to derive the concentration property of the function of this sum sequence. This contribution is central to the evaluation of asymptotic conditional distributions that are exact and also fundamental to the subsequent BER analysis. In addition, BER is observed to improve gradually with increasing sample-size for some specific scenario where the ambient data sequence has the property of non-zero expectation. It should be noted that the sum sequence is similar to the one encountered in [84], but the behavior of the sequence is different which necessitated separate handling. The difference in the analysis is mirrored in the different trends observed with respect to the behavior of the system i.e., the BER of the system is observed to gradually increase with the sample-size of the generated test statistic. A similar trend in the improvement of BER with the increasing number of antennas and sample size of the test statistic can be seen for a large-scale network. As expected, the BER performance of the system in the large-scale network is

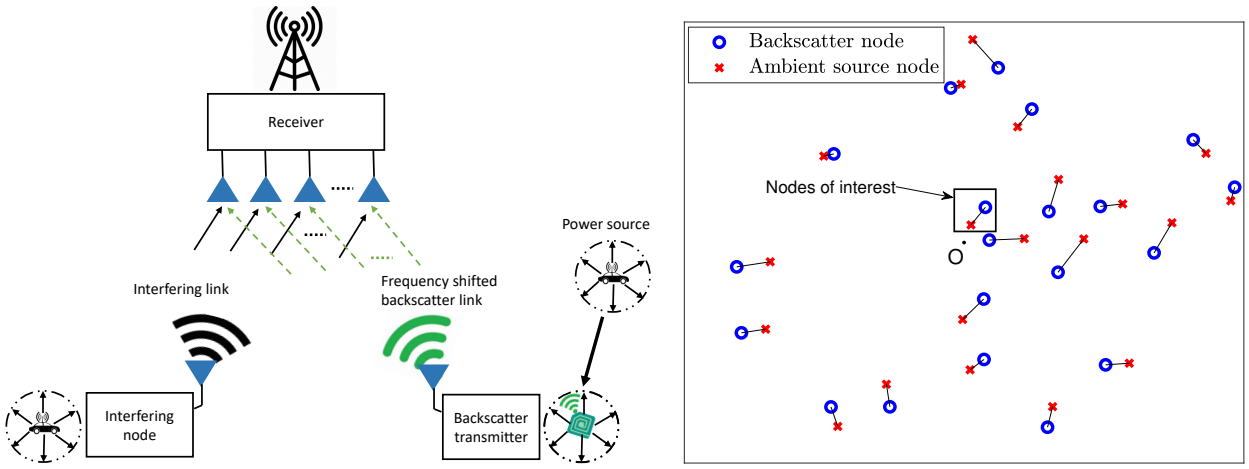

Figure 5.1: (a) System model of the single-link frequency shift ambient backscatter setup, (b) Realization of the Poisson Bipolar process containing the different backscatter nodes and their respective ambient power source nodes in the large scale network.

determined by the intensity of the point process of the interfering devices. The intensity of the interfering nodes is controlled by the size of the sub-bands available for the backscatter system. By increasing the number of sub-bands, the number of devices transmitting in the same sub-band as the backscatter node of interest within a finite region will be smaller which will bring down the interference and improve the BER of the system.

5.2 System Model

5.2.1 Single Interference Link Backscatter System

Signal and Channel Model The data rate required for the typical IoT applications is much lower compared to that of the data rate of the conventional wireless networks. Hence, the symbol duration of the backscatter data is configured such that it is N times the symbol duration of the ambient signal data. For the single interfering link system, there are four devices in the setup namely the ambient power source (PS), the backscatter transmitter (BTx), the interfering node (IN), and the receiver (Rx). The wireless channel in our setup is considered to be flat Rayleigh fading with spatial correlation present between the Rx antenna elements. This channel environment is similar to the uplink channel in a cellular network, with the BTx instead utilizing an external device for generating power in place of a dedicated power supply. The device IN is assumed to be spatially separated from the BTx but located at a distance similar to that of the distance of the backscatter node from the Rx. This kind of setup allows us to characterize the performance of the backscatter with respect to the small scale fading while keeping the channel pathloss out of the picture. The impact of channel pathloss is handled separately while analyzing the performance of the backscatter device in

a large-scale network. The rate of temporal evolution of the channel gain is assumed to be small which corresponds to the block fading scenario i.e., the channel coherence time is of the order of the duration of each backscatter symbol (that is equivalent to the duration of N ambient data symbols). The block fading model can be easily differentiated from the time-selective fading model considered in [25] by the non-varying nature of the channel gain. The spatial parameters of the channel such as angle-of-departure (AoD) and AoA in general change at a slower rate compared to the channel gains, and hence are also assumed to be constant over the coherence period. The channel model and the setup for the single interfering link system are both illustrated in Fig. 5.1a. The received signal samples at a multi-antenna Rx with uniform linear array (ULA) for the considered channel model can be represented as follows:

$$\mathbf{y}[n] = \begin{bmatrix} y_0[n] \\ y_1[n] \\ \vdots \\ y_{M_r-1}[n] \end{bmatrix} = h_r \begin{bmatrix} 1 \\ e^{j\phi_1} \\ \vdots \\ e^{j(M_r-1)\phi_1} \end{bmatrix} x_1[n] + \alpha b\, h_b h_t \begin{bmatrix} 1 \\ e^{j\phi_2} \\ \vdots \\ e^{j(M_r-1)\phi_2} \end{bmatrix} x_2[n] + \begin{bmatrix} w_0[n] \\ w_1[n] \\ \vdots \\ w_{M_r-1}[n] \end{bmatrix}, \quad (5.1)$$

where $x_1[n]$ and $x_2[n]$ are the symbols of the ambient interfering and power source devices, respectively, $w[n]$ is the additive complex Gaussian noise with mean zero and variance σ_n^2, the coefficients h_r, h_b and h_t are the channel gains of the different links in the setup assumed to be zero-mean complex Gaussian with variance σ_h^2, $b \in \{0, 1\}$ is the binary backscatter data, α is the parameter related to reflection coefficient of the BTx node, $\phi_i \equiv \frac{2\pi}{\lambda} d \cos\theta_i$ is the phase offset between the neighboring elements of the ULA for a link with AoA θ_i. Note that the channel gains h_r, h_b and h_t are not tracked by the receiver. Also the AoAs θ_1 and θ_2 of the interfering and backscatter links, respectively, are independent of each other. The received signal for a single antenna receiver can be derived from (5.1) by only considering the signal component of the first antenna. Since the data of backscatter is binary, the detection problem can be modeled as binary hypothesis testing. The notations for the null and alternate hypotheses are given by $\mathcal{H}_0$ and $\mathcal{H}_1$, respectively. The ambient data sequences $x_1[n]$ and $x_2[n]$ are assumed to be independent and identically distributed (i.i.d.), but the identical constraint can be ignored without any impact on the analysis. The received signal samples over each window are averaged directly to obtain the linear test statistic given by $Z = \frac{1}{N}\sum_{n=1}^{N} y[n]$. The binary backscatter data is transmitted using the direct on-off keying (OOK), which is the preferred modulation scheme for backscatter systems.

5.2.2 Large-Scale Backscatter Network

Spatial Distribution of Devices The channel model and the receiver (Rx) configuration for the large-scale network remain exactly the same as that of the single link interference system. In this part, we mainly deal with the effect of multiple interfering devices and large-scale path loss on the BER of the FS backscatter system. The backscatter nodes (BNs) in the network are spatially distributed according to a homogeneous Poisson point process (PPP) Φ_{BN} with intensity λ_{BN}. Suppose that the primary transmitters, also known as ambient power

sources (PSs), are distributed around the BNs independently according to a Poisson bipolar model. The distribution of the displacement between the PS and its respective BN is modeled as a bivariate Gaussian distribution with variance σ^2_{Th}. The overall bandwidth is divided into M_f bands with indices given by $\{0, 1, \cdots, M_f - 1\}$, and each ambient PS randomly selects one of these bands for transmission. It is a reasonable assumption in the case of ambient backscatter since the data requirement for most of the applications within the IoT paradigm is rather small, and thus only need narrow bandwidth for their transmissions. In addition, the backscatter devices randomly shift the backscatter link (BL) to a frequency band different from the one in which its corresponding ambient PS is transmitting. This results in a different angular profile for the BL compared to that of the link from the interfering device. The above observation comes from the interference cancellation technique that will be discussed for the single interfering-link system. By design, the frequency shift operation will result in the BL to have zero self-interference from the direct link (DL) of its corresponding ambient PS. The receivers (Rx) corresponding to the co-channel ambient backscatter transmissions in the network are clustered around their respective BN nodes, independent of the PS nodes. Due to the stationarity of all the involved point processes, the analysis can be performed for a typical Rx located at the origin. The BN node transmitting to the receiver of interest is assumed to be displaced independently modeled as a bivariate Gaussian distribution with variance σ^2_{Th} similar to the one used for displacement of PS from the BN node.

5.3 Detection and Error Analysis for a Single Link System

In this section, the BER analysis of a single interfering link backscatter system is performed. First, the asymptotic growth rate of a generalized sum sequence is derived. This result is essential to derive the conditional distributions of the test statistic, which themselves are necessary to evaluate the BER of the SA and MA receivers in our setup.

5.3.1 Growth Rate of a Generalized Sum Sequence

The understanding of the asymptotic behavior of the sequence $S_N = \sum_{n_1,n_2} x[n_1]x^*[n_2]$ is an important step in the BER analysis. Mainly, the asymptotic growth rate of the expectation and variance of the sequence $M_N = \frac{S_N}{N}$ are necessary to evaluate the conditional distributions of the test statistic. If the growth rate of these two statistical parameters are of the same order, then it is valid to conclude that the sequence M_N converges to its expectation as the sample size increases.

Lemma 5.1. *The asymptotic growth rate of the expectation and variance of the sum sequence S_N are of the order of N^2 and N^3 respectively, i.e., $\mathbb{E}[S_N] = \Theta(N^2)$ and $\text{Var}[S_N] = \Theta(N^3)$, where $f(x) = \Theta(g(x))$ means that $f(x)$ is asymptotically bounded both from above and below by $g(x)$. The sequence M_N as a result concentrates around the expectation $\mathbb{E}[M_N]$ for a large*

enough value of N, which is given as follows

$$\mathbb{E}\left[M_N\right] = \mathbb{E}\left[|X|^2\right] + (N-1)|\mathbb{E}[X]|^2. \tag{5.2}$$

Proof: See Appendix D.1. ■

Remark 5.2. The expectation of M_N in block fading grows of the order of N, unlike the constant value observed in case of time-selective fading [25]. This impacts the asymptotic BER trend with increasing N, which will be discussed later in the numerical results.

5.3.2 Conditional Distributions of the Test Statistic

The test statistic Z can be decomposed into two components: (a) the signal common to both $\mathcal{H}_0$ and $\mathcal{H}_1$, and (b) the signal unique to $\mathcal{H}_1$, as given below:

$$Z = \underbrace{h_r \frac{1}{N}\sum_{n=1}^{N} x_1[n] + \frac{1}{N}\sum_{n=1}^{N} w[n]}_{\text{(a)}} + \underbrace{\alpha b h_b h_t \frac{1}{N}\sum_{n=1}^{N} x_2[n]}_{\text{(b)}}. \tag{5.3}$$

When conditioned on $x_1[n]$, the component (a) can be characterized as a complex Gaussian due to which deriving the mean and variance is sufficient under $\mathcal{H}_0$. On the other hand, in case of $\mathcal{H}_1$ the statistic Z does not have such simple characterization since the component (b) when conditioned on $x_2[n]$ has a complex form. Using the individual distributions of (a) and (b), one can derive the joint conditional distribution of Z under the two hypotheses. From this, the conditional distribution under $\mathcal{H}_1$ can be derived by marginalizing over $\mathcal{H}_0$.

Lemma 5.3. *The probability density functions (PDFs) of the test statistic Z conditioned on $\mathcal{H}_0$ and $\mathcal{H}_1$, respectively are given by:*

$$f_{Z|\mathcal{H}_0}(z_1, z_2) = \frac{1}{\pi \mathrm{Var}_0^{\mathrm{SA}}} \exp\left(-\frac{z_1^2+z_2^2}{\mathrm{Var}_0^{\mathrm{SA}}}\right), \tag{5.4}$$

$$f_{Z|\mathcal{H}_1}(z_1, z_2) = \int_0^{\infty}\int_0^{\infty} \frac{1}{2\pi^2 \sigma_{\mathrm{SA}}^2 \mathrm{Var}_0^{\mathrm{SA}}} \exp\left(-\frac{v_1^2+v_2^2}{\mathrm{Var}_0^{\mathrm{SA}}}\right) K_0\left(\sqrt{\frac{(z_1-v_1)^2+(z_2-v_2)^2}{\sigma_{\mathrm{SA}}^2}}\right) \mathrm{d}v_1\, \mathrm{d}v_2, \tag{5.5}$$

where the parameters $\mathrm{Var}_0^{\mathrm{SA}} = \frac{\sigma_h^2 \mathbb{E}\left[|X|^2\right] + \sigma_h^2(N-1)|\mathbb{E}[X]|^2 + \sigma_n^2}{N}$ *is the variance under* $\mathcal{H}_0$, $\sigma_{\mathrm{SA}}^2 = \frac{|\alpha|^2\sigma_h^4}{4}\left(\frac{\mathbb{E}\left[|X|^2\right] + (N-1)|\mathbb{E}[X]|^2}{N}\right)$ *is a parameter related to* $\mathcal{H}_1$, *and* $K_0(.)$ *is the zeroth order modified Bessel function of the second kind.*

Proof: See Appendix D.2. ■

It is not possible to directly use the test statistic Z for detection since the distribution under $\mathcal{H}_1$ is non-isotropic. This necessitates the derivation of distributions of the squared magnitude R and phase Φ functions of the statistic Z, which are captured in the following Lemma.

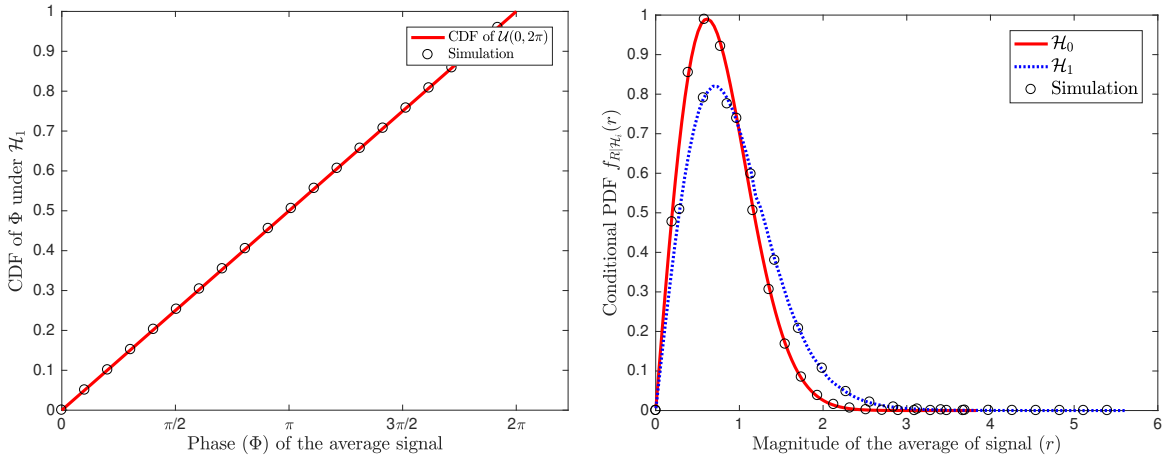

(a) (b)

Figure 5.2: (a) Conditional CDF of the phase Φ of Y under $\mathcal{H}_1$, (b) Conditional density functions of the magnitude square (R) of the average signal Y under $\mathcal{H}_0$ and $\mathcal{H}_1$ for $N = 5000$.

Lemma 5.4. *The PDFs of R conditioned on $\mathcal{H}_0$ and $\mathcal{H}_1$ are respectively given by:*

$$f_{R|\mathcal{H}_0}(r) = \frac{1}{\mathrm{Var}_0^{\mathrm{SA}}} \exp\left(-\frac{r}{\mathrm{Var}_0^{\mathrm{SA}}}\right),\ r \geq 0 \tag{5.6}$$

$$f_{R|\mathcal{H}_1}(r) = \int_0^{\infty}\int_0^{\pi} \frac{1}{2\pi\sigma_{\mathrm{SA}}^2 \mathrm{Var}_0^{\mathrm{SA}}} \exp\left(-\frac{a}{\mathrm{Var}_0^{\mathrm{SA}}}\right) K_0\left(\sqrt{\frac{r+a-2\sqrt{ra}\cos\beta}{\sigma_{\mathrm{SA}}^2}}\right) \mathrm{d}\beta\, \mathrm{d}a,\ r \geq 0, \tag{5.7}$$

and the corresponding PDFs of Φ are respectively given by:

$$f_{\Phi|\mathcal{H}_0}(\phi) = \frac{1}{2\pi}, \quad 0 \leq \phi < 2\pi \tag{5.8}$$

$$f_{\Phi|\mathcal{H}_1}(\phi) = \frac{1}{2\pi} \int_0^{2\pi}\int_0^{\infty}\int_0^{\infty} \frac{\exp\left(-\frac{a}{\mathrm{Var}_0^{\mathrm{SA}}}\right)}{\pi\sigma_{\mathrm{SA}}^2 \mathrm{Var}_0^{\mathrm{SA}}} K_0\left(\frac{\sqrt{a+b-2\sqrt{ab}\cos(\phi-\lambda)}}{\sigma_{\mathrm{SA}}}\right) \mathrm{d}a\, \mathrm{d}b\, \mathrm{d}\lambda,\ 0 \leq \phi < 2\pi. \tag{5.9}$$

Proof: See Appendix D.3. ∎

The distribution of phase Φ under $\mathcal{H}_0$ is simply given by a uniform distribution. However, as shown in (5.9), the phase distribution under $\mathcal{H}_1$ has a complicated form. We plotted the cumulative distribution function (CDF) plot of the phase Φ under $\mathcal{H}_1$ using Monte-Carlo simulations, and found that it matches closely with the uniform distribution as shown in Fig. 5.2a. From this, we can conclude that the phase distributions of the hypotheses do not carry any useful information, and the conditional distributions of the squared magnitude R are sufficient to perform detection. These distributions corresponding to the two hypotheses are compared in Fig. 5.2b for $N = 5000$.

5.3.3 Bit Error Rate

Although in theory, the optimal detection thresholds can be derived by comparing the marginal conditional distributions, the intractability of the encountered expressions makes it hard to derive the closed form expressions. For this reason, the optimal threshold is evaluated by making the Gaussian approximation for the conditional distribution of Z under $\mathcal{H}_1$. Now, the average BER expressions for both the SA and MA receivers are evaluated below.

Theorem 5.5. *The average BER of the SA receiver is given by:*

$$P_{\text{SA}}(e) = \frac{1}{2}\exp\left(-\frac{T_{\text{SA}}}{\text{Var}_0^{\text{SA}}}\right) + \int_0^{T_{\text{SA}}}\int_0^{\infty}\int_0^{\pi} \frac{\exp\left(-\frac{a}{\text{Var}_0^{\text{SA}}}\right)}{4\pi\sigma_{\text{SA}}^2\,\text{Var}_0^{\text{SA}}} K_0\left(\sqrt{\frac{r+a-2\sqrt{ra}\cos\phi}{\sigma_{\text{SA}}^2}}\right) \mathrm{d}\phi\,\mathrm{d}a\,\mathrm{d}r, \tag{5.10}$$

where $\text{Var}_1^{\text{SA}} = (\sigma_h^2 + |\alpha|^2\sigma_h^4)\left(\frac{\mathbb{E}\left[|X|^2\right]+(N-1)|\mathbb{E}[X]|^2}{N}\right) + \frac{\sigma_n^2}{N}$ *is the conditional variance under* $\mathcal{H}_1$ *and* $T_{\text{SA}} = \ln\left(\frac{\text{Var}_1^{\text{SA}}}{\text{Var}_0^{\text{SA}}}\right)\frac{\text{Var}_1^{\text{SA}}\text{Var}_0^{\text{SA}}}{\text{Var}_1^{\text{SA}}-\text{Var}_0^{\text{SA}}}$ *is the detection threshold.*

Proof: See Appendix D.4. ■

In time-selective fading, multiple receive antennas are used to cancel out the interference of the ambient signal component resulting in a dramatic improvement of the BER [25]. The same technique is applied here for block fading by multiplying the signal at the second antenna onward with appropriate phase offset, and subtracting from the signal at the first antenna to get:

$$\tilde{\mathbf{y}}[n] = \begin{bmatrix} e^{-j\phi_1}y_1[n] - y_0[n] \\ \vdots \\ e^{-j(M_r-1)\phi_1}y_{M_r-1}[n] - y_0[n] \end{bmatrix} = \tilde{\mathbf{a}}\,\alpha b\,h_b h_t x_2[n] + \tilde{\mathbf{w}}[n], \tag{5.11}$$

where the effective antenna array and noise vectors $\tilde{\mathbf{a}}$ and $\tilde{\mathbf{w}}[n]$, respectively, are given by:

$$\tilde{\mathbf{a}} = \begin{bmatrix} 2\sin\left(\frac{\phi_2-\phi_1}{2}\right)e^{j\left(\frac{\phi_2-\phi_1}{2}\right)} \\ \vdots \\ 2\sin(M_r-1)\left(\frac{\phi_2-\phi_1}{2}\right)e^{j(M_r-1)\left(\frac{\phi_2-\phi_1}{2}\right)} \end{bmatrix}, \tilde{\mathbf{w}}[n] \quad = \begin{bmatrix} e^{-j\phi_1}w_1[n] - w_0[n] \\ \vdots \\ e^{-j(M_r-1)\phi_1}w_{M_r-1}[n] - w_0[n] \end{bmatrix}. \tag{5.12}$$

The procedure to evaluate the phase inversion component $e^{-j\phi_1}$ in block fading differs from the method in time-selective fading, and one such method is provided in Appendix D.9. The optimal MMSE based weighting of the resultant signal vector after the DL cancellation will result in the following effective signal samples in the multi-antenna receiver [25]:

$$y_{\text{eff}}[n] = \mathbf{r}^*\tilde{\mathbf{a}}\alpha b\,h_b[n]h_t[n]x_2[n] + \mathbf{r}^*\tilde{\mathbf{w}}[n], \tag{5.13}$$

where $\mathbf{r} = \frac{\hat{\mathbf{K}}_{\tilde{\mathbf{W}}}^{-\mathbf{1}}\tilde{\mathbf{a}}}{|\hat{\mathbf{K}}_{\tilde{\mathbf{W}}}^{-\frac{\mathbf{1}}{\mathbf{2}}}\tilde{\mathbf{a}}|}$ is the weight vector, and the antenna gain $G = \tilde{\mathbf{a}}^* \hat{\mathbf{K}}_{\tilde{\mathbf{W}}}^{-\mathbf{1}} \tilde{\mathbf{a}}$ is given by [26]:

$$G = M_r - \frac{1}{M_r} \frac{\sin^2(M_r \frac{\phi_2 - \phi_1}{2})}{\sin^2(\frac{\phi_2 - \phi_1}{2})}. \tag{5.14}$$

As discussed earlier, the squared magnitude distributions are sufficient for detection, and the PDFs of R_{eff} of this signal conditioned on $\mathcal{H}_0$ and $\mathcal{H}_1$ are respectively given by:

$$f_{R_{\text{eff}}|\mathcal{H}_0}(r) = \frac{1}{\text{Var}_0^{\text{MA}}} \exp\left(-\frac{r}{\text{Var}_0^{\text{MA}}}\right),\ r \geq 0 \tag{5.15}$$

$$f_{R_{\text{eff}}|\mathcal{H}_1}(r) = \int_0^{\infty}\int_0^{\pi} \frac{1}{2\pi\sigma_{\text{MA}}^2 \text{Var}_0^{\text{MA}}} \exp\left(-\frac{a}{\text{Var}_0^{\text{MA}}}\right) K_0\left(\sqrt{\frac{r+a-2\sqrt{ra}\cos\beta}{\sigma_{\text{MA}}^2}}\right) \mathrm{d}\beta\, \mathrm{d}a,\ r \geq 0, \tag{5.16}$$

where $\text{Var}_0^{\text{MA}} = \frac{\sigma_n^2}{N}$ is the conditional variance under $\mathcal{H}_0$, $\sigma_{\text{MA}}^2 = \frac{G|\alpha|^2\sigma_h^4}{2}(\frac{\mathbb{E}\left[|X|^2\right]+(N-1)|\mathbb{E}[X]|^2}{N})$ is a parameter related to $\mathcal{H}_1$.

Theorem 5.6. *The average BER of the MA receiver is given by*

$$P_{\text{MA}}(e) = \int_{-\pi}^{\pi}\int_{-\pi}^{\pi} \frac{\exp(-\frac{T_{\text{MA}}}{\text{Var}_0^{\text{MA}}})}{8\pi^2} + \int_0^{T_{\text{MA}}}\int_0^{\infty} \frac{\exp(-\frac{a}{\text{Var}_0^{\text{MA}}})}{16\pi^3\sigma_{\text{MA}}^2 \text{Var}_0^{\text{MA}}} \int_0^{\pi} K_0\left(\sqrt{\frac{r+a-2\sqrt{ra}\cos\phi}{\sigma_{\text{MA}}^2}}\right) \mathrm{d}\phi\, \mathrm{d}a\, \mathrm{d}r\, \mathrm{d}\theta_1 \mathrm{d}\theta_2, \tag{5.17}$$

where $\text{Var}_1^{\text{MA}} = G|\alpha|^2\sigma_h^4(\frac{\mathbb{E}\left[|X|^2\right]+(N-1)|\mathbb{E}[X]|^2}{N}) + \frac{\sigma_n^2}{N}$ *is the conditional variance under* $\mathcal{H}_1$ *and* $T_{\text{MA}} = \ln(\frac{\text{Var}_1^{\text{MA}}}{\text{Var}_0^{\text{MA}}})\frac{\text{Var}_1^{\text{MA}}\text{Var}_0^{\text{MA}}}{\text{Var}_1^{\text{MA}}-\text{Var}_0^{\text{MA}}}$ *is the threshold.*

Proof: The conditional BER over the AoAs θ_1 and θ_2 can be evaluated directly by replacing the parameters $\text{Var}_0^{\text{SA}}, \text{Var}_1^{\text{SA}}$ and T_{SA} in the average BER of a SA receiver with the parameters $\text{Var}_0^{\text{MA}}, \text{Var}_1^{\text{MA}}$ and T_{MA} of a MA receiver, respectively. And, the average BER of the MA receiver is obtained by taking expectation over the AoAs θ_1 and θ_2. ■

5.4 Interference and Bit Error Rate in a Large Scale Network

5.4.1 Aggregate Interference from the Ambient PSs and BNs

Suppose that band 0 is the band of interest for our current transmission. Under the assumption of the Poisson bipolar model, the ambient PS nodes are independently displaced

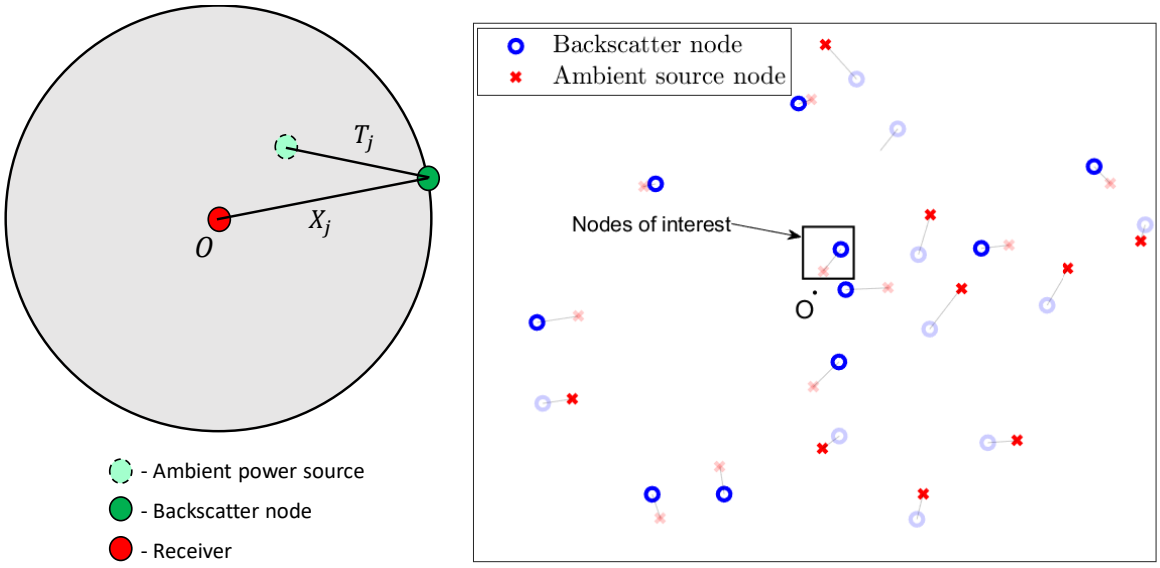

(a) (b)

Figure 5.3: (a) Displacement of the ambient power source from backscatter node, (b) Resultant interference pattern from the ambient backscatter and the power source nodes in the network.

from the BN nodes. Hence, by displacement theorem, the ambient PS nodes will form a PPP Φ_{PS} with intensity equal to λ_{BN}. Since, each ambient PS randomly select one of the M band for their transmission, by independent thinning, the interfering ambient PSs form a thinned process with respect to the original homogeneous PPP Φ_{PS}, and the intensity of the thinned PPP Φ_{PS_0} is given by $\frac{\lambda_{\text{BN}}}{M}$. The aggregate interference resulting from the thinned PPP Φ_{PS_0} is given by:

$$I_{\text{PS}} = \sum_{Y_i \in \Phi_{\text{PS}_0}} \sqrt{P_0\, L(||Y_i||)}\, h_i s_i[n], \tag{5.18}$$

where P_0 is the transmit power of the ambient PS assumed to be a constant, $L(.)$ is the path loss of the link and for a distance R it is given by $L(R) = \min(1, R^{-\gamma})$, Y_i is the co-ordinates of the ith ambient PS device, γ is the pathloss exponent, h_i is the fading gain of ith device which is assumed to be Rayleigh, and $s_i[n]$ is the ambient signal transmitted by ith device.

By design, the BN nodes around the interfering ambient PS nodes cannot be in the same band, and hence the possible interfering BNs located around the remaining points of the process Φ_{PS} form a thinned PPP Φ_{BN} with intensity $\frac{M-1}{M}\lambda_{\text{BN}}$. Once again, the interfering BN nodes are independently thinned from these BN nodes, with intensity of the resultant thinned process Φ_{BN_0} given by $\frac{M-1}{M}\frac{\lambda_{\text{BN}}}{M-1} = \frac{\lambda_{\text{BN}}}{M}$. The aggregate interference from the thinned

PPP Φ_{BN_0} is given by:

$$I_{\mathrm{BN}} = \sum_{X_j \in \Phi_{\mathrm{BN}_0}} \sqrt{P_0\, L(||T_j||) L(||X_j||)}\, \alpha_j g_j h_j b_j s_j[n], \tag{5.19}$$

where g_j is the fading gain of the link from the jth BN device to its ambient PS and assumed to be Rayleigh, T_j is the displacement of the jth PS from its BN device, X_j is the position of the corresponding jth BN device, γ is the pathloss exponent, α_j is a backscatter parameter related to the reflection coefficient Γ_i of the BN node, h_j is the fading gain of the jth BN device assumed to be Rayleigh, $s_j[n]$ is the ambient signal transmitted by the ambient PS of the jth BN device.

5.4.2 Bit Error Rate of the single antenna receiver

At the receiver node of interest, known as the typical Rx, the resultant signal for a single antenna receiver is composed of the signal from the associated backscatter node 0 and the aggregate interference, which is given by:

$$\begin{aligned} y[n] = \sqrt{P_0\, L(||T_0||) L(||X_0||)}\, \alpha_0 g_0 h_0 b_0 s_0[n] + \sum_{Y_i \in \Phi_{\mathrm{PS}_0}} \sqrt{P_0\, L(||Y_i||)}\, h_i s_i[n] \\ + \sum_{X_j \in \Phi_{\mathrm{BN}_0} \setminus \{0\}} \sqrt{P_0\, L(||T_j||) L(||X_j||)}\, \alpha_j g_j h_j b_j s_j[n] + w[n], \end{aligned} \tag{5.20}$$

where $w[n]$ is the is the zero-mean additive complex Gaussian noise of variance σ_n^2 at the receiver.

Since the BN nodes use OOK modulation for transmitting backscatter data, then each node will be transmitting $b_i \in \{0, 1\}$ equally likely and independent of one another. So, half of the interferers will be in OFF state which means that there won't be any interference from those nodes. Hence, the interfering BN nodes can be obtained by further thinning the process Φ_{BN_0}. The intensity of the thinned process Φ'_{BN_0} of the interfering BN nodes is given by $\frac{\lambda_{\mathrm{BN}}}{2M}$. The resultant signal at the typical Rx with single antenna is given by:

$$\begin{aligned} y[n] = \sqrt{P_0\, L(||T_0||) L(||X_0||)}\, \alpha_0 g_0 h_0 b_0 s_0[n] + \sum_{Y_i \in \Phi_{\mathrm{PS}_0}} \sqrt{P_0\, L(||Y_i||)}\, h_i s_i[n] \\ + \sum_{X_j \in \Phi'_{\mathrm{BN}_0} \setminus \{0\}} \sqrt{P_0\, L(||T_j||) L(||X_j||)}\, \alpha_j g_j h_j s_j[n] + w[n]. \end{aligned} \tag{5.21}$$

Likelihood Functions of Null and Alternate Hypotheses We need to evaluate signal under the individual hypotheses to proceed with the BER analysis. The signal samples $y[n]$

under null and alternate hypotheses can be expressed as:

$$\mathcal{H}_0 : y[n] = \sum_{Y_i \in \Phi_{\mathrm{PS}_0}} \sqrt{P_0\, L(||Y_i||)}\, h_i s_i[n] + \sum_{X_j \in \Phi'_{\mathrm{BN}_0} \setminus \{0\}} \sqrt{P_0\, L(||T_j||) L(||X_j||)}\, \alpha_j g_j h_j s_j[n] + w[n],$$

$$\mathcal{H}_1 : y[n] = \sqrt{P_0\, L(||T_0||) L(||X_0||)}\, \alpha_0 g_0 h_0 s_0[n] + \sum_{Y_i \in \Phi_{\mathrm{PS}_0}} \sqrt{P_0\, L(||Y_i||)}\, h_i s_i[n] + \sum_{X_j \in \Phi'_{\mathrm{BN}_0} \setminus \{0\}} \sqrt{P_0\, L(||T_j||) L(||X_j||)}\, \alpha_j g_j h_j s_j[n] + w[n]. \tag{5.22}$$

Since the channel gains of all the links are unknown at the receiver, they are considered to be zero mean complex Gaussian random variable with variance σ_h^2 equal to 1. By invoking the central limit theorem (CLT), the resultant signals under the two hypotheses can be shown to be complex Gaussian when conditioned on the ambient symbols $s_i[n]$. Therefore, evaluating the mean and variance under two hypotheses is enough to characterize the likelihood functions. Since the mean for Rayleigh fading is zero, the samples are also zero mean. Effectively, it means that we need to evaluate the variance of the aggregate signal under the two hypotheses over the different and independent point processes. The corresponding variances of the statistic $Z = \frac{1}{N}\sum y[n]$ under the two hypotheses can be expressed as follows:

$$\mathcal{H}_0 : \mathrm{Var}_0^{\mathrm{SA}} = \sum_{Y_i \in \Phi_{\mathrm{PS}_0}} P_0\, L(||Y_i||) \frac{\sigma_h^2 (\mathbb{E}\left[|s_i|^2\right] + (N-1)\left|\mathbb{E}\left[s_i\right]\right|^2)}{N} + \sum_{X_j \in \Phi'_{\mathrm{BN}_0} \setminus \{0\}} |\alpha_j|^2 \sigma_h^2 P_0\, L(||T_j||) L(||X_j||) \frac{\sigma_h^2 (\mathbb{E}\left[|s_j|^2\right] + (N-1)\left|\mathbb{E}\left[s_j\right]\right|^2)}{N} + \frac{\sigma_n^2}{N}, \tag{5.23}$$

$$\mathcal{H}_1 : \mathrm{Var}_1^{\mathrm{SA}} = \sum_{Y_i \in \Phi_{\mathrm{PS}_0}} P_0\, L(||Y_i||) \frac{\sigma_h^2 (\mathbb{E}\left[|s_i|^2\right] + (N-1)\left|\mathbb{E}\left[s_i\right]\right|^2)}{N} + \sum_{X_j \in \Phi'_{\mathrm{BN}_0} \cup \{0\}} |\alpha_j|^2 \sigma_h^2 P_0\, L(||T_j||) L(||X_j||) \frac{\sigma_h^2 (\mathbb{E}\left[|s_j|^2\right] + (N-1)\left|\mathbb{E}\left[s_j\right]\right|^2)}{N} + \frac{\sigma_n^2}{N}. \tag{5.24}$$

Conditional and average BER Assuming further that the modulation schemes used by different nodes in the network are similar, the modulation symbols can be assumed to be sampled from the distribution of an equivalent random variable S. Since the conditional distributions under the two hypotheses have already been characterized as complex Gaussian, the BER conditioned on the point processes can be expressed as follows [25, 84]:

$$P_{\mathrm{SA}}(e|\Phi) = \frac{1}{2}(1 - K^{\frac{-1}{K-1}} + K^{\frac{-K}{K-1}}),$$

where K is the ratio of the variances of $\mathcal{H}_0$ and $\mathcal{H}_1$ which can be simplified in terms of the equivalent SINR as follows:

$$K = 1 + \frac{|\alpha_0|^2 \sigma_h^2 P_0 L(||T_0||) L(||X_0||) \left(\sigma_h^2 (\mathbb{E}\left[|S|^2\right] + (N-1)\left|\mathbb{E}\left[S\right]\right|^2)\right)}{\sum\limits_{Y_i \in \Phi_{\mathrm{PS}_0}} P_0 L(||Y_i||) + \sum\limits_{X_j \in \Phi'_{\mathrm{BN}_0} \setminus \{0\}} |\alpha_i|^2 \sigma_h^2 P_0 L(||T_j||) L(||X_j||) \left(\sigma_h^2 (\mathbb{E}\left[|S|^2\right] + (N-1)\left|\mathbb{E}\left[S\right]\right|^2)\right) + \sigma_n^2}$$
$$= 1 + \mathrm{SINR}.$$

The conditional BER expression can be simplified in terms of the equivalent SINR as follows:

$$P_{\mathrm{SA}}(e|\Phi) = \frac{1}{2}\left(1 - (1+\mathrm{SINR})^{\frac{-1}{\mathrm{SINR}}} + (1+\mathrm{SINR})^{-(1+\frac{1}{\mathrm{SINR}})}\right), \tag{5.25}$$

Hence, characterizing the CDF of SINR for the considered network model is the main objective of our analysis. By configuring the parameters P_0 and σ_h^2, and considering the same reflection parameter α for all BN nodes in the network, the SINR can be modified to the following:

$$\mathrm{SINR} = \frac{|\alpha|^2 L(||T_0||) L(||X_0||)}{\sum\limits_{Y_i \in \Phi_{\mathrm{PS}_0}} L(||Y_i||) + |\alpha|^2 \sum\limits_{X_j \in \Phi'_{\mathrm{BN}_0} \setminus \{0\}} L(||T_j||) L(||X_j||) + \mathrm{SNR}^{-1}}, \tag{5.26}$$

where $\mathrm{SNR} = \frac{P_0(\mathbb{E}\left[|S|^2\right] + (N-1)|\mathbb{E}[S]|^2)}{\sigma_n^2}$ is the equivalent transmit SNR of the ambient PS.

Characteristic function of the aggregate interference To calculate the CDF of interference $I = \sum\limits_{Y_i \in \Phi_{\mathrm{PS}_0}} L(||Y_i||) + |\alpha|^2 \sum\limits_{X_j \in \Phi'_{\mathrm{BN}_0} \setminus \{0\}} L(||T_j||) L(||X_j||)$ of the PPP, we need to evaluate the characteristic function of the interference which can be simplified as follows:

$$\varphi_I(t) = E[e^{itI}] = E[e^{it(I_{\mathrm{PS}} + I_{\mathrm{BN}})}] \overset{(a)}{=} E[e^{itI_{\mathrm{PS}}}] E[e^{itI_{\mathrm{BN}}}] = \varphi_{I_{\mathrm{PS}}}(t) \varphi_{I_{\mathrm{BN}}}(t), \tag{5.27}$$

where $I_{\mathrm{PS}} = \sum\limits_{Y_i \in \Phi_{\mathrm{PS}_0}} L(||Y_i||)$, $I_{\mathrm{BN}} = |\alpha|^2 \sum\limits_{X_j \in \Phi'_{\mathrm{BN}_0} \setminus \{0\}} L(||T_j||) L(||X_j||)$, and (a) follows from the independence of the two terms. The distances distributions of $U_j = ||T_j||, U_0 = ||T_0||$ and $V_0 = ||X_0||$ dependent on the system model considered for the network. Some of the widely used models for these points are Gaussian and uniform distributions which are considered in our work. The characteristic function result of the following lemma is used to derive the BER of the single antenna receiver in the theorem immediately after that.

Lemma 5.7. *The characteristic functions of the interference terms I_{PS} and I_{BN} are respectively given as follows:*

$$\varphi_{I_{\mathrm{PS}}}(t) = \exp\left(-2\pi \frac{\lambda_{BN}}{M} \int_0^\infty (1 - e^{itL(x)}) x \, \mathrm{d}x\right), \tag{5.28}$$

$$\varphi_{I_{\mathrm{BN}}}(t) = \exp\left(-2\pi\frac{\lambda_{BN}}{2M}\int_0^\infty\left(1-\int_0^\infty f_R(r)e^{it|\alpha|^2L(r)L(p)}\,\mathrm{d}r\right)p\,\mathrm{d}p\right), \tag{5.29}$$

where $f_R(r)$ is the distance distribution of the separation between PS and its respective BN node.

Proof: See Appendix D.5. ■

Theorem 5.8. *The average BER of the single antenna receiver for the scheme $\mathcal{M}_1$ can be expressed as follows:*

$$P_{\mathrm{SA}}(e) = \frac{1}{4} - \frac{1}{\pi}\int_0^\infty\int_0^\infty\int_0^\infty\int_0^\infty \mathrm{Im}\left[\frac{e^{-it(\frac{|\alpha|^2L(u_0)L(v_0)}{x}-\mathrm{SNR}^{-1})}\varphi_I(t)}{t}\right] f_{U_0,V_0}(u_0,v_0)g'_{\mathcal{M}_1}(x)\,\mathrm{d}t\,\mathrm{d}u_0\,\mathrm{d}v_0\,\mathrm{d}x, \tag{5.30}$$

where $f_{U_0,V_0}(u_0,v_0)$ is the joint distance distribution of the separation between the typical Rx-BN nodes and the typical BN-PS nodes.

Proof: See Appendix D.6. ■

5.4.3 Bit Error Rate of the multi-antenna receiver

Cancellation of the dominant interferer and the resultant SINR analysis

Since the interfering devices belong to two different independent point processes, the selection of the dominant interferer will require the evaluation of the probability with which the node belongs to a certain point process, and then evaluate the interference field by removing the dominant interferer, which is tedious. Instead, a simpler mechanism is to superpose the two point processes and obtain a single point process. In doing that, one should also make sure that sufficient conditions are met before the simplification to a single point process, in addition to deriving the intensity of the superimposed PPP. First, the BN point process Φ'_{BN_0} can be simplified to another homogeneous PPP by invoking the displacement theorem over the additional pathloss resulting from the distance to the power source of the BN node. Assuming an unbounded pathloss model, the distance U_j can be enveloped into the distance $||X_j||$, where the effective distance can be taken as a random displacement of the original distance $||X_j||$ with a variable U_j. Applying the displacement theorem [94, Lemma 1], the homogeneous PPP Φ'_{BN_0} with intensity $\frac{\lambda_{BN}}{2M}$, each point $X_j \in \Phi'_{\mathrm{BN}_0}$ transformed to $Y_j = |\alpha|^{\frac{2}{\gamma}}U_jX_j$, where U_j are i.i.d. such that $\mathbb{E}[|\alpha|^{\frac{4}{\gamma}}U_j^{-2}] < \infty$, the new point process Φ''_{BN_0} formed by the points Y_j is also a homogeneous PPP with intensity given by $\frac{\lambda_{BN}}{2M}|\alpha|^{\frac{4}{\gamma}}\mathbb{E}[U_j^{-2}]$. However, the expectation $\mathbb{E}[U_j^{-2}]$ unfortunately would not be finite, and the problem is circumvented by the bounded pathloss model $L(U_j) = \min(1, U_j)$ for the backscatter nodes. And, the two point processes Φ_{PS_0} and Φ''_{BN_0} are independent, and hence by invoking the

superposition theorem a single point process Φ_{int} for the interference field can be obtained. Since the two superimposed point processes are PPP, the resultant point process Φ_{int} is again a PPP whose intensity can be determined as $\frac{\lambda_{BN}}{M} + \frac{\lambda_{BN}}{2M}|\alpha|^{\frac{4}{\gamma}}\mathbb{E}[L(U_j)^{\frac{2}{\gamma}}]$.

The dominant interferer belonging to the PPP Φ_{int} is removed using the interference cancellation approach described in the single interference link system. Since non-coherent detection is performed at the receiver, the dominant interferer is considered to be the nearest interfering device. Hence, the interference field will lie outside the disc with radius to the dominant interferer. The distance distribution to the dominant interferer can be evaluated for the homogeneous PPP as the Rayleigh distribution which is given by:

$$f_{P_1}(p_1) = 2\pi\left(\frac{\lambda_{BN}}{M} + \frac{\lambda_{BN}}{2M}|\alpha|^{\frac{4}{\gamma}}\mathbb{E}[L(U_j)^{\frac{2}{\gamma}}]\right) p_1 e^{-\left(\frac{\lambda_{BN}}{M} + \frac{\lambda_{BN}}{2M}|\alpha|^{\frac{4}{\gamma}}\mathbb{E}[L(U_j)^{\frac{2}{\gamma}}]\right)\pi p_1^2}. \tag{5.31}$$

The antenna gain $G(\theta_0, \theta_1)$ of the BN of interest is given by [26]:

$$G(\theta_0,\theta_1) = \tilde{\mathbf{a}}^*(\theta_0,\theta_1)\hat{\mathbf{K}}_{\tilde{\mathbf{W}}}^{-\mathbf{1}}\tilde{\mathbf{a}}(\theta_0,\theta_1) = M_r - \frac{1}{M_r}\frac{\sin^2\left(\pi\frac{d}{\lambda}M_r(\cos\theta_0 - \cos\theta_1)\right)}{\sin^2\left(\pi\frac{d}{\lambda}(\cos\theta_0 - \cos\theta_1)\right)}, \tag{5.32}$$

while the antenna gain of the interfering nodes $G(\theta_i, \theta_1; \theta_0)$ is given by:

$$G(\theta_i,\theta_1;\theta_0) = \frac{|\tilde{\mathbf{a}}^*(\theta_0,\theta_1)\hat{\mathbf{K}}_{\tilde{\mathbf{W}}}^{-\mathbf{1}}\tilde{\mathbf{a}}(\theta_i,\theta_1)|^2}{G(\theta_0,\theta_1)}, \tag{5.33}$$

where $G(\theta_0, \theta_1)$ is given in (5.32) and $\tilde{\mathbf{a}}^*(\theta_0,\theta_1)\hat{\mathbf{K}}_{\tilde{\mathbf{W}}}^{-\mathbf{1}}\tilde{\mathbf{a}}(\theta_i,\theta_1) =$

$$\begin{aligned}
&(M_r^2 - 2M_r + \frac{1}{M_r}) - \frac{e^{j\pi\frac{d}{\lambda}M_r(\cos\theta_i - \cos\theta_0)}}{M_r}\frac{\sin\left(\pi\frac{d}{\lambda}(M_r-1)(\cos\theta_i - \cos\theta_0)\right)}{\sin\left(\pi\frac{d}{\lambda}(\cos\theta_i - \cos\theta_0)\right)} \\
&- (M_r - 1 - \frac{1}{M_r})e^{-j\pi\frac{d}{\lambda}M_r(\cos\theta_0 - \cos\theta_1)}\frac{\sin\left(\pi\frac{d}{\lambda}(M_r-1)(\cos\theta_0 - \cos\theta_1)\right)}{\sin\left(\pi\frac{d}{\lambda}(\cos\theta_0 - \cos\theta_1)\right)} \\
&- (M_r - 1 - \frac{1}{M_r})e^{j\pi\frac{d}{\lambda}M_r(\cos\theta_i - \cos\theta_1)}\frac{\sin\left(\pi\frac{d}{\lambda}(M_r-1)(\cos\theta_i - \cos\theta_1)\right)}{\sin\left(\pi\frac{d}{\lambda}(\cos\theta_i - \cos\theta_1)\right)} \\
&- e^{j\pi\frac{d}{\lambda}M_r(\cos\theta_i - \cos\theta_0)}\frac{\sin\left(\pi\frac{d}{\lambda}(M_r-1)(\cos\theta_0 - \cos\theta_1)\right)}{\sin\left(\pi\frac{d}{\lambda}(\cos\theta_0 - \cos\theta_1)\right)}\frac{\sin\left(\pi\frac{d}{\lambda}(M_r-1)(\cos\theta_i - \cos\theta_1)\right)}{\sin\left(\pi\frac{d}{\lambda}(\cos\theta_i - \cos\theta_1)\right)}.
\end{aligned} \tag{5.34}$$

The modified SINR expression for the multi-antenna receiver after interference cancellation is given by:

$$\text{SINR} = \frac{|\alpha|^2 G(\theta_0,\theta_1)L(U_0)L(V_0)}{\sum\limits_{Y_i\in\Phi_{\text{int}}\setminus\{Y_1\}} G(\theta_i,\theta_1;\theta_0)L(||Y_i||) + \text{SNR}^{-1}}. \tag{5.35}$$

Lemma 5.9. *The characteristic function of the interference I present in the multi-antenna receiver is given as follows:*

$$\varphi_I(t) = E_{P_1}\left[\exp\left(-2\pi\left(\frac{\lambda_{BN}}{M}+\frac{\lambda_{BN}}{2M}|\alpha|^{\frac{4}{\gamma}}\mathbb{E}[L(U_j)^{\frac{2}{\gamma}}]\right)\int_{p_1}^{\infty}(1-E_{\Theta_i,\Theta_1}\left[e^{itG(\Theta_i,\Theta_1)L(v)}\right])v\,\mathrm{d}v\right)\right]. \tag{5.36}$$

where the expectation operator is over the random variables Θ_i that are uniformly distributed over $[0, 2\pi)$.

Proof: See Appendix D.7. ■

Theorem 5.10. *The average BER of the multi-antenna receiver can be expressed as follows:*

$$P_{\mathrm{MA}}(e) = \frac{1}{4}-\frac{1}{\pi}\int_0^{\infty}\int_{-\pi}^{\pi}\int_{-\pi}^{\pi}\int_0^{\infty}\int_0^{\infty}\int_0^{\infty}\mathrm{Im}\left[\frac{e^{-it(\frac{|\alpha|^2G(\theta_0,\theta_1)L(u_0)L(v_0)}{x}-\mathrm{SNR}^{-1})}\varphi_I(t)}{t}\right] \times f_{U_0,V_0}(u_0,v_0)f_{\Theta_0,\Theta_1}(\theta_0,\theta_1)g'_{\mathcal{M}_1}(x)\,\mathrm{d}t\,\mathrm{d}u_0\,\mathrm{d}v_0\,\mathrm{d}\theta_0\,\mathrm{d}\theta_1\,\mathrm{d}x, \tag{5.37}$$

where $f_{\Theta_0,\Theta_1}(\theta_0,\theta_1)$ is the joint distribution of the AoAs of the BN of interest and the strongest interfering node.

Proof: See Appendix D.8. ■

5.5 Numerical Results and Discussion

In this section, the numerical results accuracy from the Monte-Carlo simulations are compared with the analytical results to verify the accuracy of our analysis. The variance of the fading gain σ_h^2 and the intensity of the PPP of interfering devices are both configured to 1. Our results correspond to the BER performance of the system both in a single interfering link system and a large-scale network. The BER performance of the OOK modulation with increasing SNR and $N = 2000$ for the MA receiver is shown in Fig. 5.4a. The MA receiver does not suffer from the BER floor as shown in the figure. Additionally, the BER performance of the OOK scheme with increasing N for the MA receiver is plotted in Fig. 5.4b. The BER in block fading decays inversely with N resulting in an asymptotic BER of zero, unlike the non-zero asymptotic BER observed in time-selective fading due to saturation [25]. In the same Figs. 5.4a and 5.4b, the performance of the MA receiver with increasing number of antennas are also shown. It can be observed that with the doubling of antennas there is an SNR gain of 8 dB, showing a very good performance improvement. The performance of the frequency-shift backscatter in a large-scale system are discussed now. The performance of the SA receiver with varying sub-band size are shown in Figs. 5.5a and 5.5b. The increasing size of sub-bands means that the intensity of the interfering devices modeled as a PPP will

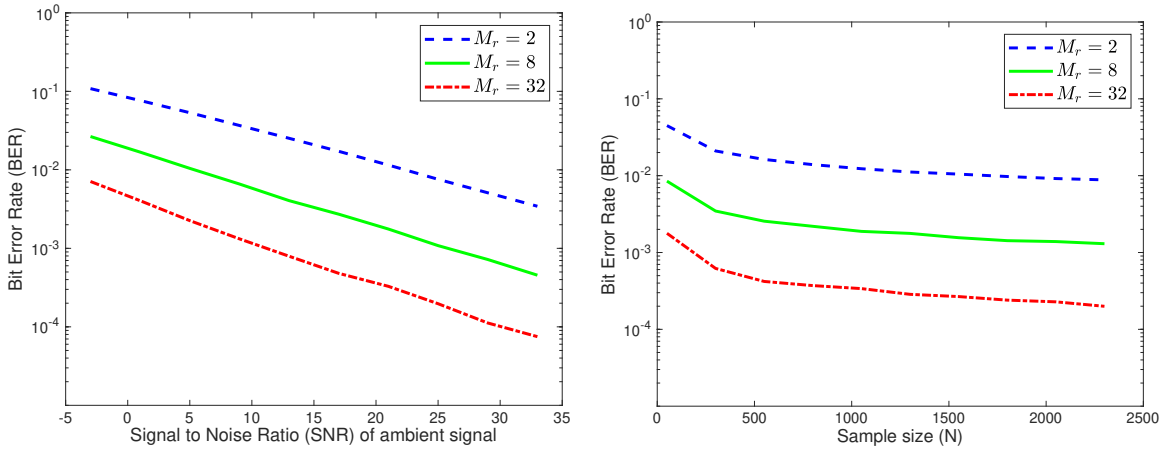

(a) (b)

Figure 5.4: (a) BER vs SNR comparison for increasing receive antenna size M_r in scheme $\mathcal{M}_1$ with $N = 2000$, (b) BER vs N comparison for increasing receive antenna size M_r in scheme $\mathcal{M}_1$ with SNR = 20 dB.

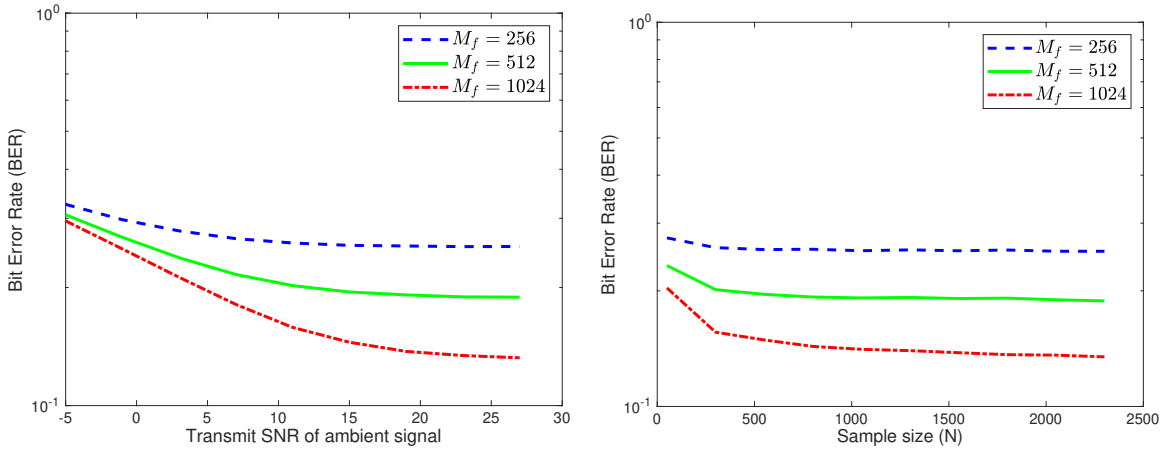

(a) (b)

Figure 5.5: (a) BER vs SNR comparison for single-antenna receiver with changing sub-band size M_f and $N = 2000$, (b) BER vs N comparison for single-antenna receiver with changing sub-band size M_f and SNR = 20 dB.

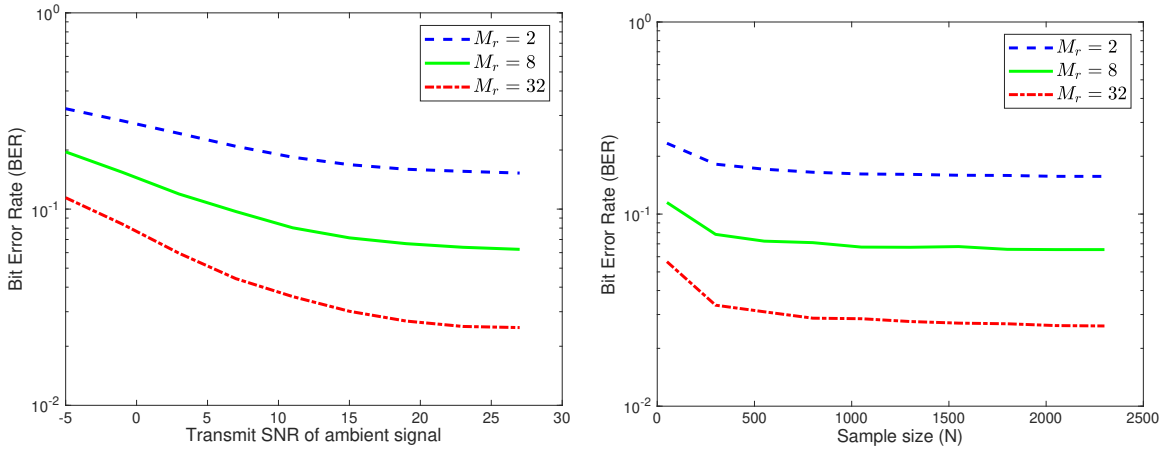

(a) (b)

Figure 5.6: (a) BER vs SNR comparison for varying number of antennas at the receiver with sub-band size $M_f = 512$ and $N = 2000$, (b) BER vs N comparison comparison for varying number of antennas at the receiver with sub-band size $M_f = 512$ and SNR = 20 dB.

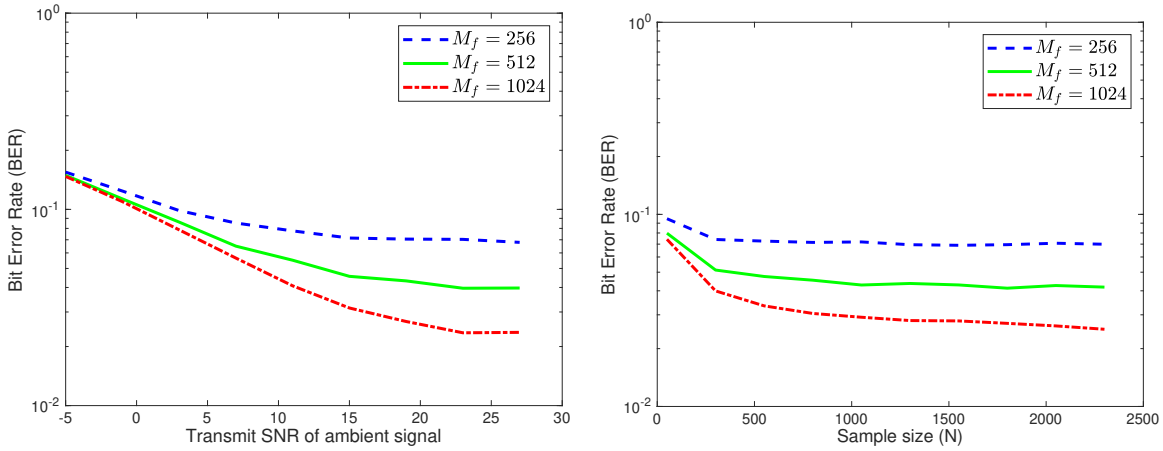

(a) (b)

Figure 5.7: (a) BER vs SNR comparison for single-antenna receiver with changing sub-band size M_f, $M_r = 16$ and $N = 2000$, (b) BER vs N comparison for single-antenna receiver with changing sub-band size M_f, $M_r = 16$ and SNR = 20 dB.

come down resulting in smaller interference and thereby result in improvement of the BER. The effect of the path loss and multiple interfering devices in the large-scale system can be drawn from the smaller BER values in comparison to the single-link system. There is a similar trend in the BER with increasing sample size but the decaying rate is dependent on the sub-band size. In Figs. 5.7a and 5.7b, we show the similar plots for the MA receiver in a large-scale network. The BER performance of the MA receiver is better compared to the SA receiver but the general behavior with respect to the sub-band size is similar.

5.6 Summary

In this chapter, the BER performance characterization of the frequency-shift ambient backscatter system under a single-interfering device and a large scale network has been investigated. A non-coherent detection technique is deployed for the backscatter system and the performance under a block fading channel has been analyzed. Our results related to the single interference link system suggest that the BER performance can be improved drastically using multiple antennas at the receiver. Similar to the time-selective fading, we have shown in block fading that multiple antennas can be used to remove the BER floor observed for the single-antenna receiver in non-coherent ambient backscatter. In addition, the BER improvement in block fading is observed to be larger compared to the improvement seen for time-selective fading in [25]. The increase in the number of antennas at the receiver resulted in considerable gain, and the increase in the size of the samples of the test statistic will similarly result in decreased BER of the system. Coming to the large scale network, the BER performance is observed to improve with decreasing intensity of the interfering point process. This can be achieved by increasing the sub-band size which can result in smaller of number of devices transmitting simultaneously in the same frequency sub-band.

Chapter 6

Conclusion

In this chapter, we summarize the main contributions of the dissertation work and briefly discuss the potential future problems and research directions of ambient backscatter.

6.1 Summary

Ambient backscatter technology is expected to play an important role in enabling *self-sustainability* and communication capability in a new class of physical devices deployed at an unprecedented scale as part of the Internet-of-Things (IoT) paradigm. However, due to the asymmetric operation of these systems the direct link from the source to the receiver will act as an interference. They also suffer from the *two-way* propagation loss resulting in a limited communication range. In addition to that, any receiver in ambient backscatter has to detect the backscatter data in the presence of some randomness from the unknown ambient data of the radio frequency (RF) source signal. For a quick and wider adoption of the ambient backscatter technology, it is highly important to overcome these challenges and limitations of the ambient backscatter. In this dissertation, we have addressed these challenges by developing a good theoretical understanding of the ambient backscatter systems. The work has thoroughly investigated some new transmitter/receiver designs and signal detection procedures while analyzing the bit error rate (BER) performance of the proposed techniques.

In Chapter 2, the main focus is on the system design of coherent and semi-coherent detection and the exact BER analysis of the ambient backscatter system in a flat Rayleigh fading channel. The analysis is performed for a block fading channel by first characterizing the exact conditional distributions of the average energy of the received signal in terms of the noncentral chi-squared distribution. Then, the exact analytical expressions of the conditional BER are derived from the conditional distributions both for the receivers with and without channel state information (CSI). The average BER analysis requires careful treatment of the joint distribution of correlated fading components that appear in the two hypotheses of the problem. In addition, we explore the evaluation of maximum likelihood threshold, and provide two alternate detection threshold techniques due to the complexity of maximum likelihood (ML) detection. Several key insights are drawn from the aforementioned analysis. First, the optimal BER of the ambient backscatter system is dependent on the energies of the signal and noise through signal-to-noise ratio (SNR) and not separately on the individual energies. Second, increasing the sample length N provides diminishing returns in terms of

BER improvement.

In Chapter 3, we have considered the problem of signal detection in a time-selective fading channel. Ambient backscatter systems have mainly been studied for low mobility scenarios that are modeled using a block fading channel. While the block fading model is sufficient for stationary environments like home and office, a time-selective fading model is more suitable for non-stationary environments, such as roads and campuses. In this work, we have investigated the performance of an ambient backscatter system by studying the design and BER of a non-coherent detector under time-selective fading channels. A new receiver architecture based on the direct average of the signal samples is proposed which departs from the conventional energy averaging-based receivers used in the literature. The new architecture is simpler to implement, robust to timing errors, and lends tractability to the asymptotic analysis. A key intermediate step in the BER analysis is the derivation of a new concentration result for a general sum sequence which is encountered while deriving the conditional distributions of the received signal. In the analysis, it is demonstrated that a BER floor exists for the single antenna (SA) receiver due to the direct link (DL) interference of the ambient power source, thereby resulting in poor performance. The BER floor is removed using a multi-antenna (MA) receiver which eliminates the interference by tracking the angle-of-arrival (AoA) of the DL and drastically improving the performance. Further, increasing the number receive antennas improves the angular resolution which can support applications where the AoAs of the DL and backscatter link (BL) are very close. The BER of the system in time-selective fading improves with the increasing number of signal samples for the test statistic, but saturates asymptotically. The BER is also observed to improve with increasing temporal-correlation of the fading channel.

In Chapter 4, we have looked at the advantages of implementing coding in an ambient backscatter system by analyzing the impact of Manchester encoding on the performance of non-coherent detection. Once again considering a time-selective channel, we have analytically and numerically shown the advantages of the encoding scheme over the conventional direct on-off keying (OOK) modulation. The optimal decision rule for Manchester encoding is shown to be dependent only on the relative magnitude of the test statistic for the two symbols of the codeword, making the optimal detection threshold independent of all the system parameters. In addition, the proposed encoding scheme also achieves an SNR gain over the direct OOK modulation with the MA receiver, the exact value of which will vary based on the joint distribution of the AoAs of the DL and BL links. In our analysis, the SNR gain evaluated for the uniformly and narrowly spread AoAs came to be around 4 dB and 3 dB, respectively, which is a substantial improvement in the performance of the ambient backscatter system.

In Chapter 5, we shift our focus to the characterization of BER performance of the frequency-shift ambient backscatter system under a large-scale network. First, the performance of the system in a single interfering-link system is presented whose performance is compared to the one obtained in a large-scale network. A non-coherent detection technique is deployed for the backscatter system and the performance under a block fading channel

has been analyzed. The interfering devices in the large-scale network are modeled as a homogeneous Poisson point process (PPP) which lends tractability to the BER analysis. Our results related to the single interference link system suggest that the BER performance can be improved drastically using multiple antennas at the receiver. Similar to the time-selective fading, we have shown in block fading that multiple antennas can be used to remove the BER floor observed for the single-antenna receiver in non-coherent ambient backscatter. In addition, the BER improvement in block fading is observed to be larger compared to the improvement seen for time-selective fading. The increase in the number of antennas at the receiver resulted in considerable SNR gain, and the increase in the size of the samples of the test statistic will result in decreased BER of the system. Similarly, with encoding we also achieve an SNR gain that is reflected in the improvement of the system BER. Coming to the large-scale network, the BER performance is observed to improve with decreasing intensity of the interfering point process. This can be achieved by increasing the sub-band size which can result in lesser of number of devices transmitting in the same frequency sub-band.

6.2 Future Work

The problems studied in this dissertation have addressed some of the important challenges faced by ambient backscatter systems, and the proposed mechanisms can result in a faster adoption of the technology. However, there are still many open and unsolved problems in ambient backscatter that require novel solutions. From the solid foundation laid by our work, we have outlined below some of the most promising problems that are worth solving in the future.

Frequency Domain Analysis of Ambient Backscatter. An ambient backscatter system can be considered as the secondary user within a cognitive radio setup where the primary user is given by the ambient power source. Therefore, it is important to design the ambient backscatter system such that the bandwidth occupied by the backscatter signal is within the allowed bandwidth of the primary user. Otherwise, unintentional interfering signals come into the system model that will have to be taken into consideration when analyzing the system performance. In fact, many ideas are proposed in the ambient backscatter literature disregarding this essential point, which promise outstanding results that are not achievable in practice. For example, consider the scenario where the symbol duration of the ambient and backscatter data symbols are equal, and that the waveforms are assumed to be rectangular in the frequency domain. The bandwidth occupied by the backscatter signal will be twice the bandwidth of the independent waveforms since the convolution of two rectangular waveforms will result in a triangular waveform. The additional bandwidth requirement due to the convolution operation in the frequency domain is generally ignored in the literature. Although the performance promised by these studies are superior it is not practically possible to achieve them since the additional interference signals are ignored in their system model. To properly design these systems, it is important to determine the frequency domain

representation of the ambient backscatter signal. We believe that this analysis will act as a guideline when proposing new system designs for the ambient backscatter in future.

Wideband Ambient Backscatter. Our initial analysis found some similarities between the narrowband version of ambient backscatter and the spread spectrum signals [95–97]. Using this connection, advanced techniques that combine the two techniques can be designed which we call wideband (WB) ambient backscatter. The main objective of this work would be to determine the frequency domain representation of the WB ambient backscatter, and then come up with system designs that can result in good performance even with the imperfections of the wireless channel. The proposed research will involve the study and design of long range (LoRa) backscatter communication while simultaneously investigating the problem of multiple access for the different ambient backscatter devices.

Single side band (SSB) Ambient Backscatter. Single-side band (SSB) modulation in the communication systems exploits the symmetry of the pulse amplitude modulation (PAM) scheme to reduce the signal bandwidth of the transmitted SSB signal by half. However, the complexity of generating SSB modulation signals and receiver detection in initial communication systems have prohibited their widespread implementation. Instead, quadrature amplitude modulation (QAM) which achieves similar spectral efficiency by transmitting two orthogonal signals in the overall bandwidth is preferred due to the ease of generating the QAM signal. The technological progress in the receiver detection techniques, such as turbo equalization and decoding [98], over the past two decades has spurred research efforts into the joint treatment of the SSB and QAM modulation schemes [99–101]. In the ambient backscatter system, the joint SSB and QAM design can be achieved in a slightly different but subtle way by limiting the backscatter signal transmission to either the upper or lower side-band in the bandwith occupied by the ambient RF signal. At the receiver side, iterative decoding techniques can be applied to efficiently decode both the ambient and backscatter data. This approach can result in tremendous improvement in the throughput of the ambient backscatter data in comparison to the current transmission techniques, where the backscatter data is transmitted at a much lower rate compared to that of the ambient RF data. A thorough investigation into the SSB transmission of the backscatter data (which we call SSB backscatter) over the ambient RF signal is required to achieve the targeted performance.

Appendices

Appendix A

A.1 Proof of Lemma 2.7

The conditional PDF of Y under $\mathcal{H}_0$ can be obtained from the conditional PDF of a scaled version given by $Z = \frac{Y}{c}$, where $c = \frac{\sigma^2}{2N}$. The expression of Z can be written as follows:

$$Z = \frac{2}{\sigma^2} \sum_{n=1}^{N} |h_0 x(n) + w(n)|^2. \tag{A.1}$$

Expanding $h_0 = h_{0r} + \mathrm{j} h_{0i}$, $x(n) = x_r(n) + \mathrm{j} x_i(n)$ and $w(n) = w_r(n) + \mathrm{j} w_i(n)$, where $\mathrm{j} = \sqrt{-1}$, results in the form:

$$Z = \frac{2}{\sigma^2} \sum_{n=1}^{N} |(h_{0r} + \mathrm{j} h_{0i})(x_r(n) + \mathrm{j} x_i(n)) + w_r(n) + \mathrm{j} w_i(n)|^2 \tag{A.2}$$

$$= \sum_{n=1}^{N} \frac{2}{\sigma^2} \left(h_{0r} x_r(n) - h_{0i} x_i(n) + w_r(n)\right)^2 + \sum_{n=1}^{N} \frac{2}{\sigma^2} \left(h_{0i} x_r(n) + h_{0r} x_i(n) + w_i(n)\right)^2, \tag{A.3}$$

where each term in the two summations is a square of an independent non-zero mean Gaussian RV with unit variance when conditioned on fading and $x(n)$. Also, notice that there are a total of $2N$ independent real-valued RVs.

The density function of this sum is given by noncentral chi-squared distribution [102]. This distribution is associated with a non-centrality parameter λ which is equal to the sum of the squared means of each Gaussian RV. The value of λ corresponding to Z can be evaluated as:

$$\lambda = \frac{2 \sum_{n=1}^{N} \left(h_{0r} x_r(n) - h_{0i} x_i(n)\right)^2}{\sigma^2} + \frac{2 \sum_{n=1}^{N} \left(h_{0i} x_r(n) + h_{0r} x_i(n)\right)^2}{\sigma^2} \tag{A.4}$$

$$= \frac{2 \sum_{n=1}^{N} |x(n)|^2 |h_0|^2}{\sigma^2} = \frac{2 \sum_{n=1}^{N} |x(n)|^2 \mu}{\sigma^2} \overset{(b)}{=} \frac{2N\bar{E}\mu}{\sigma^2}, \tag{A.5}$$

where (b) follows from the average energy given by (2.2).

Notice that the distribution of Z is independent of $x(n)$ since the parameter λ approaches a constant value because of (2.2). Therefore, the PDF of Z conditioned on $\mathcal{H}_0$ and μ is given

by the noncentral chi-squared distribution with parameter λ calculated above:

$$f_{Z|\mathcal{H}_0,\mu}(z) = \sum_{i=0}^{\infty} \frac{\exp(-\frac{\lambda}{2})(\frac{\lambda}{2})^i}{i!} f_{\chi^2}(z; 2N+2i) = \sum_{i=0}^{\infty} \frac{\exp(-\frac{\mu N\bar{E}}{\sigma^2})(\frac{\mu N\bar{E}}{\sigma^2})^i}{i!} f_{\chi^2}(z; 2N+2i), \tag{A.6}$$

where $f_{\chi^2}(z; 2N+2i)$ is the PDF of central chi-squared distribution with degree $2N+2i$.

The conditional PDF $f_{Y|\mathcal{H}_0,\mu}(t)$ follows from the distribution of scaled transformation of a RV. The conditional PDF of Y under $\mathcal{H}_1$ is derived using similar procedure.

A.2 Proof of Lemma 2.9

The distribution of a noncentral chi-square RV with degree $2v$ can be alternatively represented as a function of the modified Bessel function of the first kind $I_v(z)$ where v represents order of the function. Hence, the conditional PDFs of average signal energy Y whose distribution is characterized as noncentral chi-square with degree $2N$ can also be expressed as follows:

$$\begin{aligned} f_{Y|\mathcal{H}_0,\mu}(t) &= \frac{N}{\sigma^2} e^{-\left(\frac{N}{\sigma^2}t + \frac{N\mu\bar{E}}{\sigma^2}\right)} \left(\frac{4t}{\mu\bar{E}}\right)^{\frac{N-1}{2}} I_{N-1}\left(\frac{2N}{\sigma^2}\sqrt{\mu\bar{E}t}\right) \\ &\overset{(c)}{=} \frac{N}{\pi\sigma^2} e^{-\left(\frac{N}{\sigma^2}t + \frac{N\mu\bar{E}}{\sigma^2}\right)} \left(\frac{4t}{\mu\bar{E}}\right)^{\frac{N-1}{2}} \int_0^{\pi} e^{\frac{2N}{\sigma^2}\sqrt{\mu\bar{E}t}\cos\theta} \cos(N-1)\theta \, \mathrm{d}\theta, \end{aligned} \tag{A.7}$$

$$\begin{aligned} f_{Y|\mathcal{H}_1,\nu}(t) &= \frac{N}{\sigma^2} e^{-\left(\frac{N}{\sigma^2}t + \frac{N\nu\bar{E}}{\sigma^2}\right)} \left(\frac{4t}{\nu\bar{E}}\right)^{\frac{N-1}{2}} I_{N-1}\left(\frac{2N}{\sigma^2}\sqrt{\nu\bar{E}t}\right) \\ &\overset{(d)}{=} \frac{N}{\pi\sigma^2} e^{-\left(\frac{N}{\sigma^2}t + \frac{N\nu\bar{E}}{\sigma^2}\right)} \left(\frac{4t}{\nu\bar{E}}\right)^{\frac{N-1}{2}} \int_0^{\pi} e^{\frac{2N}{\sigma^2}\sqrt{\nu\bar{E}t}\cos\theta} \cos(N-1)\theta \, \mathrm{d}\theta, \end{aligned} \tag{A.8}$$

where (c) and (d) follow from the integral form of the modified Bessel function of the first kind with integer order given for reference in definition 2.4.

By the ML rule, the threshold value T_{mlt} is chosen as the point where the two conditional distributions are equal and the simplified expression is given by the following equation:

$$e^{\frac{N}{\sigma^2}\bar{E}(\nu-\mu)} \left(\frac{\nu}{\mu}\right)^{\frac{N-1}{2}} \int_0^{\pi} e^{\frac{2N}{\sigma^2}\sqrt{\mu\bar{E}\,T_{\text{mlt}}}\cos\theta} \cos(N-1)\theta \, \mathrm{d}\theta = \int_0^{\pi} e^{\frac{2N}{\sigma^2}\sqrt{\nu\bar{E}\,T_{\text{mlt}}}\cos\theta} \cos(N-1)\theta \, \mathrm{d}\theta. \tag{A.9}$$

A.3 Proof of Lemma 2.10

The approximations to the conditional PDFs can be derived from (2.19) which again is provided below for reference:

$$Y = \underbrace{|h_r + \alpha h_b h_t b|^2 \bar{E}}_{Y_0\text{: constant}} + \underbrace{\frac{2}{N} \mathrm{Re}\left\{ (h_r + \alpha h_b h_t b) \sum_{n=1}^{N} x(n) w^*(n) \right\}}_{Y_1\text{: Gaussian RV}} + \underbrace{\frac{1}{N} \sum_{n=1}^{N} |w(n)|^2}_{Y_2\text{: Central-}\chi^2\text{ RV}} .$$

The conditional mean and variance of the Gaussian component Y_1 in the above equation is given by:

$$\mathcal{H}_0 : \mathbb{E}[Y_1|\mathcal{H}_0] = \mu\bar{E}, \mathrm{VAR}[Y_1|\mathcal{H}_0] = \frac{2}{N}\mu\bar{E}\sigma^2, \tag{A.10}$$

$$\mathcal{H}_1 : \mathbb{E}[Y_1|\mathcal{H}_1] = \nu\bar{E}, \mathrm{VAR}[Y_1|\mathcal{H}_1] = \frac{2}{N}\nu\bar{E}\sigma^2. \tag{A.11}$$

The Central-χ^2 component Y_2 will be approximated either as a constant or a Gaussian. In the first case (first Gaussian approximation), Y_2 can be simply approximated as the conditional mean of Central-χ^2 RV which is σ^2. For the second case (second Gaussian approximation), Y_2 will be approximated as a Gaussian RV with conditional mean and variance equal to that of Y_2, as given below:

$$\mathcal{H}_0 : \mathbb{E}[Y_2|\mathcal{H}_0] = \sigma^2, \mathrm{VAR}[Y_2|\mathcal{H}_0] = \frac{1}{N}\sigma^4, \tag{A.12}$$

$$\mathcal{H}_1 : \mathbb{E}[Y_2|\mathcal{H}_1] = \sigma^2, \mathrm{VAR}[Y_2|\mathcal{H}_1] = \frac{1}{N}\sigma^4. \tag{A.13}$$

It is easy to see that Y is Gaussian distributed under both approximations. For the first Gaussian approximation, the conditional distributions of Y under the two hypotheses are given by:

$$f_{Y|\mathcal{H}_0,\mu}(t) = \frac{1}{\sqrt{2\pi\frac{2}{N}\mu\bar{E}\sigma^2}} \exp\left(-\frac{\left(t - \mu\bar{E} - \sigma^2\right)^2}{2\frac{2}{N}\mu\bar{E}\sigma^2} \right), \tag{A.14}$$

$$f_{Y|\mathcal{H}_1,\nu}(t) = \frac{1}{\sqrt{2\pi\frac{2}{N}\nu\bar{E}\sigma^2}} \exp\left(-\frac{\left(t - \nu\bar{E} - \sigma^2\right)^2}{2\frac{2}{N}\nu\bar{E}\sigma^2} \right). \tag{A.15}$$

Similarly, the conditional distributions of Y under the two hypotheses for the second Gaussian approximation are given by:

$$f_{Y|\mathcal{H}_0,\mu}(t) = \frac{1}{\sqrt{2\pi\left(\frac{2}{N}\mu\bar{E}\sigma^2 + \frac{1}{N}\sigma^4\right)}} \exp\left(-\frac{\left(t - \mu\bar{E} - \sigma^2\right)^2}{2\left(\frac{2}{N}\mu\bar{E}\sigma^2 + \frac{1}{N}\sigma^4\right)} \right), \tag{A.16}$$

$$f_{Y|\mathcal{H}_1,\nu}(t) = \frac{1}{\sqrt{2\pi\left(\frac{2}{N}\nu\bar{E}\sigma^2 + \frac{1}{N}\sigma^4\right)}} \exp\left(-\frac{\left(t - \nu\bar{E} - \sigma^2\right)^2}{2\left(\frac{2}{N}\nu\bar{E}\sigma^2 + \frac{1}{N}\sigma^4\right)}\right). \tag{A.17}$$

After equating the conditional distributions under the two hypotheses (separately for each of the approximations) and rearranging the terms, we get the final expressions of the threshold values.

A.4 Proof of Lemma 2.12

We note that [103] has derived the marginal distribution of h_1 and its magnitude squared parameter ν in the context of outage analysis for ambient backscatter systems. However, our derivation here is different since our focus is on the joint distribution of h_0 and h_1, and their magnitude squared parameters μ and ν for the bit error rate analysis.

The distribution of fading terms of direct links h_r and h_t are given by $\mathcal{CN}(0, \sigma_{h_1}^2)$ and backscatter link is given by $\mathcal{CN}(0, \sigma_{h_2}^2)$. The distribution of $\alpha h_b \sim \mathcal{CN}(0, |\alpha|^2\sigma_{h_2}^2)$, formed by combining α and h_b, follows from the scalar multiplication property of circularly symmetric Gaussian random vectors [104, Sec. 7.8.1].

The joint distribution of the real and imaginary parts of fading component h_0 is Gaussian. Similarly, the joint distribution of the real and imaginary parts of double Gaussian term $U = \alpha h_b h_t$ of the fading component h_1 is given in [105, 106]. For completeness, the expressions are provided below:

$$f_{h_{0R},h_{0I}}(h_{0r}, h_{0i}) = \frac{1}{\pi\sigma_{h_1}^2} \exp\left(-\frac{h_{0r}^2 + h_{0i}^2}{\sigma_{h_1}^2}\right), \tag{A.18}$$

$$f_{U_R,U_I}(u_r, u_i) = \frac{1}{2\pi\left(\frac{|\alpha|\sigma_{h_1}\sigma_{h_2}}{2}\right)^2} K_0\left(\frac{\sqrt{u_r^2 + u_i^2}}{\frac{|\alpha|\sigma_{h_1}\sigma_{h_2}}{2}}\right), \tag{A.19}$$

where K_0 is the zeroth order modified Bessel function of second kind.

The joint distribution of the real and imaginary parts of h_1 conditioned on h_0 is related to the joint distribution of U by the shift transformation property of a RV:

$$f_{h_{1R},h_{1I}|h_{0R},h_{0I}}(h_{1r}, h_{1i}) = f_{U_R,U_I}(h_{1r} - h_{0r}, h_{1i} - h_{0i}). \tag{A.20}$$

The joint distribution of the polar coordinates of h_0 and h_1 is derived from rectangular coordinates using the transformation property of RVs as follows:

$$\begin{aligned} f_{R_{h_0},\Theta_{h_0},R_{h_1},\Theta_{h_1}}(r_{h_0}, \theta_{h_0}, r_{h_1}, \theta_{h_1}) &\overset{(e)}{=} f_{R_{h_0},\Theta_{h_0}}(r_{h_0}, \theta_{h_0})\ f_{R_{h_1},\Theta_{h1}|R_{h_0},\Theta_{h_0}}(r_{h_1}, \theta_{h_1}|r_{h_0}, \theta_{h_0}) \\ &\overset{(f)}{=} r_{h_0} f_{h_{0R},h_{0I}}(r_{h_0}\cos\theta_{h_0}, r_{h_0}\sin\theta_{h_0}) r_{h_1} f_{U_R,U_I}(r_{h_1}\cos\theta_{h_1} - r_{h_0}\cos\theta_{h_0}, r_{h_1}\sin\theta_{h_1} - r_{h_0}\sin\theta_{h_0}) \end{aligned}$$

$$= r_{h_0} \frac{1}{\pi\sigma_{h_1}^2} e^{-\frac{r_{h_0}^2}{\sigma_{h_1}^2}} r_{h_1} \frac{1}{2\pi\left(\frac{|\alpha|\sigma_{h_1}\sigma_{h_2}}{2}\right)^2} K_0\left(\frac{\sqrt{r_{h_1}^2 + r_{h_0}^2 - 2r_{h_1}r_{h_0}\cos(\theta_{h_1} - \theta_{h_0})}}{\frac{|\alpha|\sigma_{h_1}\sigma_{h_2}}{2}}\right), \quad \text{(A.21)}$$

where (e) follows from de-conditioning of RVs through chain rule, and (f) follows from the relationship between the joint distribution functions of polar and rectangular coordinates. Since the joint distribution is only a function of the difference $\theta_{h_1} - \theta_{h_0}$, we can further simplify it by replacing θ_{h_1} with $\theta = \theta_{h_1} - \theta_{h_0}$. The modified joint distribution is obtained by the transformation of RVs and is given by:

$$f_{R_{h_0},\Theta_{h_0},R_{h_1},\Theta}(r_{h_0},\theta_{h_0},r_{h_1},\theta) = \frac{r_{h_0}}{\pi\sigma_{h_1}^2} e^{-\frac{r_{h_0}^2}{\sigma_{h_1}^2}} \frac{r_{h_1}}{2\pi\left(\frac{|\alpha|\sigma_{h_1}\sigma_{h_2}}{2}\right)^2} K_0\left(\frac{\sqrt{r_{h_1}^2 + r_{h_0}^2 - 2r_{h_1}r_{h_0}\cos\theta}}{\frac{|\alpha|\sigma_{h_1}\sigma_{h_2}}{2}}\right), \quad \text{(A.22)}$$

where $0 \leq \theta_{h_0} \leq 2\pi$ and $-\theta_{h_0} \leq \theta \leq 2\pi - \theta_{h_0}$. The joint marginal distribution of R_{h_1}, R_{h_0}, obtained by integrating over the ranges of Θ_{h_0} and Θ, is given by:

$$f_{R_{h_0},R_{h_1}}(r_{h_0},r_{h_1})$$

$$= \int_0^{2\pi}\int_{-\theta_{h_0}}^{2\pi-\theta_{h_0}} \frac{r_{h_0}}{\pi\sigma_{h_1}^2} e^{-\frac{r_{h_0}^2}{\sigma_{h_1}^2}} \frac{r_{h_1}}{2\pi\left(\frac{|\alpha|\sigma_{h_1}\sigma_{h_2}}{2}\right)^2} K_0\left(\frac{\sqrt{r_{h_1}^2 + r_{h_0}^2 - 2r_{h_1}r_{h_0}\cos\theta}}{\frac{|\alpha|\sigma_{h_1}\sigma_{h_2}}{2}}\right) \mathrm{d}\theta\mathrm{d}\theta_{h_0} \quad \text{(A.23)}$$

$$\overset{(g)}{=} \int_0^{2\pi}\int_0^{2\pi} \frac{r_{h_0}}{\pi\sigma_{h_1}^2} e^{-\frac{r_{h_0}^2}{\sigma_{h_1}^2}} \frac{r_{h_1}}{2\pi\left(\frac{|\alpha|\sigma_{h_1}\sigma_{h_2}}{2}\right)^2} K_0\left(\frac{\sqrt{r_{h_1}^2 + r_{h_0}^2 - 2r_{h_1}r_{h_0}\cos\theta}}{\frac{|\alpha|\sigma_{h_1}\sigma_{h_2}}{2}}\right) \mathrm{d}\theta\mathrm{d}\theta_{h_0} \quad \text{(A.24)}$$

$$\overset{(h)}{=} \int_0^{\pi} \frac{2r_{h_0}}{\pi\sigma_{h_1}^2} e^{-\frac{r_{h_0}^2}{\sigma_{h_1}^2}} \frac{r_{h_1}}{\left(\frac{|\alpha|\sigma_{h_1}\sigma_{h_2}}{2}\right)^2} K_0\left(\frac{\sqrt{r_{h_1}^2 + r_{h_0}^2 - 2r_{h_1}r_{h_0}\cos\theta}}{\frac{|\alpha|\sigma_{h_1}\sigma_{h_2}}{2}}\right) \mathrm{d}\theta \quad \text{(A.25)}$$

where (g) follows from the periodicity of $\cos\theta$ which is 2π, and (h) follows from marginalizing the PDF over the range of θ_{h_0} and the symmetry of $\cos\theta$ around $\theta = \pi$.

Finally, the joint distribution of μ and ν is given by:

$$f_{\mu,\nu}(\mu,\nu) \overset{(i)}{=} \frac{1}{4\sqrt{\mu\nu}} f_{R_{h_0},R_{h_1}}(\sqrt{\mu},\sqrt{\nu}) \quad \text{(A.26)}$$

$$= \frac{2}{\pi\sigma_{h_1}^2} e^{-\frac{\mu}{\sigma_{h_1}^2}} \frac{1}{|\alpha|^2\sigma_{h_1}^2\sigma_{h_2}^2} \int_0^{\pi} K_0\left(\frac{\sqrt{\mu + \nu - 2\sqrt{\mu\nu}\cos\theta}}{\frac{|\alpha|\sigma_{h_1}\sigma_{h_2}}{2}}\right) \mathrm{d}\theta, \quad \text{(A.27)}$$

where (i) follows from the relation between the joint PDFs of modulus of RVs given by R_{h_0} and R_{h_1}, and the square of modulus of the same RVs given by μ and ν, respectively. ■

Appendix B

B.1 Proof of Lemma 3.3

The value of the summation $\sum_{n_1 \neq n_2} \rho^{|n_1-n_2|}$, which is used in the subsequent steps is given by:

$$\sum_{n_1 \neq n_2} \rho^{|n_1-n_2|} = \frac{2\rho}{1-\rho}(N - \frac{1-\rho^N}{1-\rho}), \qquad 0 \leq \rho < 1. \tag{B.1}$$

The expectation of the sum sequence S_N can be evaluated easily as follows:

$$\mathbb{E}\left[S_N\right] = \mathbb{E}\left[\sum_{n_1,n_2} \rho^{|n_1-n_2|}\, x[n_1]x_m^*[n_2]\right] = \sum_n \mathbb{E}\left[|x[n]|^2\right] + \sum_{n_1 \neq n_2} \rho^{|n_1-n_2|}\, \mathbb{E}\left[x[n_1]\right] \mathbb{E}\left[x_m^*[n_2]\right]$$

$$\overset{(a)}{=} \sum_n \mathbb{E}\left[|X|^2\right] + \sum_{n_1 \neq n_2} \rho^{|n_1-n_2|}\, |\mathbb{E}\left[X\right]|^2 \overset{(b)}{=} N\mathbb{E}\left[|X|^2\right] + \frac{2\rho}{1-\rho}(N - \frac{1-\rho^N}{1-\rho})|\mathbb{E}\left[X\right]|^2, \tag{B.2}$$

where (a) and (b) follow from the assumption that the ambient sequence $x[n]$ is i.i.d., and the value of summation given in (B.1), respectively. It can be easily observed that the expectation of this sum grows asymptotically of the order of N, meaning $\mathbb{E}\left[S_N\right] = \Theta[n]$. Using this, the expectation of $M_N = \frac{S_N}{N}$ can be shown to be a constant, whose value is given in (3.11).

The variance of the sum sequence S_N can first be simplified as given below:

$$\mathrm{Var}\left[S_N\right] = \mathbb{E}\left[\left(\sum_{i_1,j_1} \rho^{|i_1-j_1|}\, x[i_1]x_m^*[j_1]\right)\left(\sum_{i_2,j_2} \rho^{|i_2-j_2|}\, x_m^*[i_2]x[j_2]\right)\right] - \mathbb{E}\left[S_N\right]^2$$

$$= \mathbb{E}\Bigg[\sum_{i_1}\sum_{i_2} |x[i_1]|^2|x[i_2]|^2 + 2\sum_{i_1}\sum_{i_2 \neq j_2} \rho^{|i_2-j_2|}\, |x[i_1]|^2 x_m^*[i_2]x[j_2]$$

$$+ \sum_{i_1 \neq j_1}\sum_{i_2 \neq j_2} \rho^{|i_1-j_1|+|i_2-j_2|}\, x[i_1]x_m^*[j_1]x_m^*[i_2]x[j_2]\Bigg] - \mathbb{E}\left[S_N\right]^2$$

$$\overset{(c)}{=} \sum_{i_1=i_2} \mathbb{E}\left[|X|^4\right] + \left\{\sum_{i_1 \neq i_2} 1 + \sum_{i_1 \neq j_1} \rho^{2|i_1-j_1|} - (\sum_i 1)^2\right\}\left(\mathbb{E}\left[|X|^2\right]\right)^2$$

$$+ 2\sum_{i_1 \neq j_2} \rho^{|i_1-j_2|}\mathbb{E}\left[X(X^*)^2\right]\mathbb{E}\left[X\right] + 2\sum_{i_1 \neq i_2} \rho^{|i_1-i_2|}\mathbb{E}\left[(X)^2X^*\right]\mathbb{E}\left[X^*\right] + \sum_{i_1 \neq j_1} \rho^{2|i_1-j_1|}\left|\mathbb{E}\left[X^2\right]\right|^2$$

$$+2\left\{\sum_{i_1\neq i_2\neq j_2}\rho^{|i_2-j_2|}+\sum_{i_1\neq j_1\neq j_2}\rho^{|i_1-j_1|+|i_1-j_2|}-\sum_{i,i_1\neq i_2}\rho^{|i_1-i_2|}\right\}\mathbb{E}\left[|X|^2\right]|\mathbb{E}\left[X\right]|^2$$
$$+\sum_{i_1\neq i_2\neq j_1}\rho^{|i_1-j_1|+|i_2-j_1|}\mathbb{E}\left[X^2\right](\mathbb{E}\left[X^*\right])^2+\sum_{i_1\neq j_1\neq j_2}\rho^{|i_1-j_1|+|j_1-j_2|}\left(\mathbb{E}\left[X^2\right]\right)^*(\mathbb{E}\left[X\right])^2$$
$$+\left\{\sum_{i_1\neq j_1\neq i_2\neq j_2}\rho^{|i_1-j_1|+|i_2-j_2|}-(\sum_{n_1\neq n_2}\rho^{|n_1-n_2|})^2\right\}|\mathbb{E}\left[X\right]|^4, \tag{B.3}$$

where (c) follows from the piece-wise separation of different summations by permuting the indices i_1, i_2, j_1 and j_2 of the first term, and the expansion of the second term $\mathbb{E}\left[S_N\right]$.

The main objective here is to show that the variance also grows asymptotically of the order of N. The complete derivation of the variance expression is conceptually simple but tedious to present in a limited space. For this reason, we only provide a sketch of the proof, which is sufficient to understand the approach. Recall the assumption that the higher order moments of the sequences $x[n]$ upto the highest order present in (B.3) are finite. With this assumption, it is sufficient to prove that the coefficient of each moment increases of the order of N. The coefficient of $\mathbb{E}\left[|X|^4\right]$ is straightforward to obtain and is given by N. Using (B.1), it is again straightforward to show that $\sum_{i_1\neq j_1}\rho^{2|i_1-j_1|}$ is a function N, and the summations $\sum_{i_1\neq i_2}1$ and $(\sum_{i}1)^2$ are respectively given by N^2 and $N(N-1)$. Hence, the coefficient of $\left(\mathbb{E}\left[|X|^2\right]\right)^2$ is proportional to N and increases asymptotically of the order of N. Then, the coefficients of $\mathbb{E}\left[X(X^*)^2\right]\mathbb{E}\left[X\right], \mathbb{E}\left[(X)^2X^*\right]\mathbb{E}\left[X^*\right]$ and $\left|\mathbb{E}\left[X^2\right]\right|^2$, given by either $\sum_{i_1\neq j_1}\rho^{|i_1-j_1|}$ or $\sum_{i_1\neq j_1}\rho^{2|i_1-j_1|}$, are already shown to be proportional to N. Similarly, the summation $\sum_{i_1\neq j_1\neq j_2}\rho^{|i_1-j_1|+|i_1-j_2|}$ can be evaluated by piece-wise categorization into different subsets and be shown to grow of the order of N. In addition, the summations $\sum_{i_1\neq i_2\neq j_2}\rho^{|i_2-j_2|}$ and $\sum_{i,i_1\neq i_2}\rho^{|i_1-i_2|}$ can both be shown to have the same factor for N^2, and hence the coefficients of $\left|\mathbb{E}\left[X^2\right]\right|^2, \mathbb{E}\left[X^2\right](\mathbb{E}\left[X^*\right])^2$ and $(\mathbb{E}\left[X^2\right])^*(\mathbb{E}\left[X\right])^2$ all increase at the order of N. Finally, it can also be shown that $\sum_{i_1\neq j_1\neq i_2\neq j_2}\rho^{|i_1-j_1|+|i_2-j_2|}$ and $(\sum_{n_1\neq n_2}\rho^{|n_1-n_2|})^2$ are both proportional to $N(N-1)$ with the same factor, which also means that $|\mathbb{E}\left[X\right]|^4$ grows of the order of N. From this, we can conclude that $\mathrm{Var}\left[S_N\right]=\Theta(N)$. As a consequence, the variance of $M_N=\frac{S_N}{N}$ will be decreasing at the rate of $1/N$ asymptotically. This completes the proof.

B.2 Proof of Lemma 3.4

When conditioned on $x[n]$, a sample of the received signal under $\mathcal{H}_0$, as given in (3.12), is a complex Gaussian RV. As a result, the mean of the received samples can also be characterized as a complex Gaussian, *albeit* the samples correlated with one another. Since the

complex Gaussian RV is completely defined by its mean and variance, we are just required to derive them. First, the conditional expectation and variance of an individual sample $y[n]$ can be derived as:

$$\begin{aligned}
\mathbb{E}\left[y[n]\right] &= \mathbb{E}\left[\left(\rho_r^{n-1}h_r[1] + \sqrt{1-\rho_r^2}\left\{\sum_{k=1}^{n-1}\rho_r^{n-k-1}g_r[k]\right\}\right)x[n] + w[n]\right] \\
&= \left(\rho_r^{n-1}\mathbb{E}\left[h_r[1]\right] + \sqrt{1-\rho_r^2}\left\{\sum_{k=1}^{n-1}\rho_r^{n-k-1}\mathbb{E}\left[g_r[k]\right]\right\}\right)x[n] + \mathbb{E}\left[w[n]\right] = 0, \\
\mathrm{Var}\left[y[n]\right] &= \mathrm{Var}\left[\rho_r^{n-1}h_r[1]x[n]\right] + \sum_{k=1}^{n-1}\mathrm{Var}\left[\sqrt{1-\rho_r^2}\left\{\rho_r^{n-k-1}g_r[k]x[n]\right\}\right] + \mathrm{Var}\left[w[n]\right] \\
&= (\rho_r^{2n-2} + \sum_{k=1}^{n-1}(1-\rho_r^2)\rho^{2n-2k-2})\sigma_h^2|x[n]|^2 + \sigma_n^2 = \sigma_h^2|x[n]|^2 + \sigma_n^2.
\end{aligned}$$

Similarly, the conditional covariance of any two distinct samples $y[i]$ and $y[j]$ is given by:

$$\begin{aligned}
&\mathrm{Cov}\left[y[i], y[j]\right] \overset{(a)}{=} \mathbb{E}\left[y[i]y^*[j]\right] \\
&= \mathbb{E}\Bigg[(\rho_r^{i+j-2}|h_r[1]|^2 + \sqrt{1-\rho_r^2}\sum_{k_2=1}^{j-1}\rho_r^{i+j-k_2-2}h_r[1]g_r^*[k_2])x[i]x^*[j] + \rho_r^{i-1}h_r[1]x[i]w^*[j] \\
&+ (\sqrt{1-\rho_r^2}\sum_{k_1=1}^{i-1}\rho_r^{i+j-k_1-2}h_r^*[1]g_r[k_1] + (1-\rho_r^2)\sum_{k_1=1}^{i-1}\sum_{k_2=1}^{j-1}\rho_r^{i+j-k_1-k_2-2}g_r[k_1]g_r^*[k_2])x[i]x^*[j] \\
&+ \sqrt{1-\rho_r^2}\sum_{k_1=1}^{i-1}\rho_r^{i-k_1-1}w^*[j]g_r[k_1]x[i] + \rho_r^{j-1}h_r[1]x^*[j]w[i] \\
&+ \sqrt{1-\rho_r^2}\sum_{k_2=1}^{j-1}\rho_r^{j-k_2-1}w[i]g_r^*[k_2]x^*[j] + w[i]w^*[j]\Bigg] \\
&= \sigma_h^2(\rho_r^{i+j-2} + (1-\rho_r^2)\sum_{k=1}^{\min(i,j)-1}\rho_r^{i+j-2k-2})x[i]x^*[j] = \sigma_h^2\rho_r^{|j-i|}x[i]x^*[j],
\end{aligned}$$

where (a) follows from zero valued conditional expectation of the signal samples. Using the above derivations, the conditional expectation and variance of Z can be evaluated as follows:

$$\begin{aligned}
\mathbb{E}\left[Z\right] &= \mathbb{E}\left[\frac{1}{N}\sum_{n=1}^{N}y[n]\right] = \frac{1}{N^2}\left(\mathbb{E}\left[\sum_{n=1}^{N}y[n]\right]\right) = \frac{1}{N^2}\left(\sum_{n=1}^{N}\mathbb{E}\left[y[n]\right]\right) = 0, \\
\mathrm{Var}\left[Z\right] &= \mathrm{Var}\left[\frac{1}{N}\sum_{n=1}^{N}y[n]\right] = \frac{1}{N^2}\left(\sum_{n=1}^{N}\mathrm{Var}\left[y[n]\right] + \sum_{n_1\neq n_2}\mathrm{Cov}\left[y[n_1], y[n_2]\right]\right)
\end{aligned}$$

$$= \frac{1}{N^2}(\sigma_h^2 \sum_{n=1}^{N} |x[n]|^2 + N\sigma_n^2 + \sigma_h^2 \sum_{n_1 \neq n_2} \rho_r^{|n_1-n_2|}\, x[n_1]x^*[n_2]) = \frac{1}{N}\left(\sigma_h^2 M_N + \sigma_n^2\right)$$

$$\overset{(b)}{\approx} \frac{1}{N}\left(\sigma_h^2 \mathbb{E}\left[M_N\right] + \sigma_n^2\right) = \frac{1}{N}(\sigma_h^2 \mathbb{E}\left[|X|^2\right] + \frac{2\rho_r}{1-\rho_r}(1 - \frac{1-\rho_r^N}{N(1-\rho_r)})|\mathbb{E}\left[X\right]|^2 + \sigma_n^2), \quad \text{(B.4)}$$

where (b) results from the approximation of M_N by its expectation, given in Lemma 3.3.

B.3 Proof of Lemma 3.5

Observe that when conditioned on the ambient signal $x[n]$, the three signal components of the received signal under the alternate hypothesis $\mathcal{H}_1$: (i) direct signal from ambient source, (ii) backscatter signal, and (iii) receiver noise, are independent of each other.

$$y[n] = h_r[n]x[n] + \underbrace{\alpha h_b[n]h_t[n]x[n]}_{y_b[n]} + w[n] \quad \text{(B.5)}$$

This means that the expectation and variance of the sum can be derived using just the expectation and variance of each component. Since, we have already computed the expectation and variance of the direct signal and the receiver noise combination (in Lemma 3.5 for $\mathcal{H}_0$), it is now enough to compute the expectation and variance of the backscatter component $y_b[n]$.

To derive that, we further condition the signal on $h_b[n]$ since it will preserve and allow us to use the additive property of the Gaussian RVs. The conditional expectation and variance of an individual sample of the backscatter signal $y_b[n]$ and the conditional covariance of any two distinct samples $y[i]$ and $y[j]$ can be evaluated as:

$$\begin{aligned}
\mathbb{E}\left[y_b[n]\right] &= \mathbb{E}\left[\alpha h_b[n]h_t[n]x[n]\right] = \alpha h_b[n]x[n]\mathbb{E}\left[h_t[n]\right] = 0,\\
\text{Var}\left[y_b[n]\right] &= \text{Var}\left[\alpha h_b[n]h_t[n]x[n]\right] = |\alpha|^2|h_b[n]x[n]|^2\text{Var}\left[h_t[n]\right] = |\alpha|^2\sigma_h^2|h_b[n]x[n]|^2,\\
\text{Cov}\left[y_b[i], y_b[j]\right] &= |\alpha|^2 h_b[i]h_b^*[j]x[i]x^*[j]\text{Cov}\left[h_t[i], h_t[j]\right] = |\alpha|^2\sigma_h^2\rho_t^{|j-i|}h_b[i]h_b^*[j]x[i]x^*[j].
\end{aligned}$$

The conditional expectation and variance of the mean of signal samples $y_b[n]$ can be determined from their corresponding expectation and variance of the individual samples as follows:

$$\begin{aligned}
\mathbb{E}\left[\frac{1}{N}\sum_{n=1}^{N} y_b[n]\right] &= \frac{1}{N}\left(\mathbb{E}\left[\sum_{n=1}^{N} y_b[n]\right]\right) = \frac{1}{N}\left(\sum_{n=1}^{N}\mathbb{E}\left[y_b[n]\right]\right) = 0,\\
\text{Var}\left[\frac{1}{N}\sum_{n=1}^{N} y_b[n]\right] &= \frac{1}{N^2}\left(\sum_{n=1}^{N}\text{Var}\left[y_b[n]\right] + \sum_{n_1\neq n_2}\text{Cov}\left[y_b[n_1], y_b[n_2]\right]\right)
\end{aligned}$$

$$= \frac{1}{N^2}(|\alpha|^2\sigma_h^2\sum_{n=1}^{N}|h_b[n]x[n]|^2 + |\alpha|^2\sigma_h^2\sum_{n_1\neq n_2}\rho_t^{|n_1-n_2|}\,h_b[n_1]h_b^*[n_2]x[n_1]x^*[n_2])$$
$$= \frac{1}{N}|\alpha|^2\sigma_h^2\underbrace{\frac{1}{N}\sum_{1\leq n_1,n_2\leq N}\rho_t^{|n_1-n_2|}\,h_b[n_1]h_b^*[n_2]x[n_1]x^*[n_2]}_{M_N^b}. \tag{B.6}$$

The sequence M_N^b, similar to M_N, is a function of the sum variable of the ambient sequence $x[n]$ and can be shown to asymptotically converge to its expectation. This expected value of M_N^b can be evaluated as follows:

$$\mathbb{E}\left[M_N^b\right] = \mathbb{E}\left[\frac{1}{N}\sum_{1\leq n_1,n_2\leq N}\rho_t^{|n_1-n_2|}\,h_b[n_1]h_b^*[n_2]x[n_1]x^*[n_2]\right]$$
$$= \frac{1}{N}\mathbb{E}\left[\sum_{1\leq n\leq N}|h_b[n]x[n]|^2 + \sum_{n_1\neq n_2}\rho_t^{|n_1-n_2|}\,h_b[n_1]h_b^*[n_2]x[n_1]x^*[n_2]\right]$$
$$= \frac{1}{N}(\sum_{1\leq n\leq N}\mathbb{E}\left[|h_b[n]|^2\right]\mathbb{E}\left[|x[n]|^2\right] + \sum_{n_1\neq n_2}\rho_t^{|n_1-n_2|}\,\mathbb{E}\left[h_b[n_1]h_b^*[n_2]\right]\mathbb{E}\left[x[n_1]\right]\mathbb{E}\left[x^*[n_1]\right])$$
$$\overset{(b)}{=}\sigma_h^2\sum_{1\leq n\leq N}\frac{\mathbb{E}[|X|^2]}{N} + \sigma_h^2\sum_{n_1\neq n_2}(\rho_t\rho_b)^{|n_1-n_2|}\frac{|\mathbb{E}[X]|^2}{N}\overset{(c)}{=}\sigma_h^2\mathbb{E}\left[|X|^2\right] + \sigma_h^2\frac{2\rho_t\rho_b}{1-\rho_t\rho_b}\left(1-\frac{1-\rho_t^N\rho_b^N}{N(1-\rho_t\rho_b)}\right)|\mathbb{E}[X]|^2,$$

where (b) follows from the assumption that the ambient sequence $x[n]$ is i.i.d. and the expectation of $h_b[n_1]h_b^*[n_2]$ which is given by $\sigma_h^2\rho^{|n_1-n_2|}$, and (c) follows from the value of summation $\sum_{n_1\neq n_2}\rho^{2|n_1-n_2|}$ that can be derived using (B.1) in Lemma 3.3.

The conditional variance of the mean of $y_b[n]$ can thus be approximated using $\mathbb{E}\left[M_N^b\right]$ as:

$$\text{Var}\left[\frac{1}{N}\sum_{n=1}^{N}y_b[n]\right] \approx \frac{1}{N}\left(|\alpha|^2\sigma_h^2\mathbb{E}\left[M_N^b\right]\right)$$
$$= \frac{1}{N}\left(|\alpha|^2\sigma_h^4\mathbb{E}\left[|X|^2\right] + |\alpha|^2\sigma_h^4\frac{2\rho_t\rho_b}{1-\rho_t\rho_b}\left(1-\frac{1-\rho_t^N\rho_b^N}{N(1-\rho_t\rho_b)}\right)|\mathbb{E}\left[X\right]|^2\right). \tag{B.7}$$

The final step is to obtain the variance of mean Z of the signal samples under $\mathcal{H}_1$ by adding the individual variances in (B.4) and (B.7) respectively. This completes the proof.

B.4 Proof of Theorem 3.6

The optimal decision rule for the receiver is evaluated through the comparison of the conditional PDFs of the null and alternate hypotheses $\mathcal{H}_0$ and $\mathcal{H}_1$ derived in Lemmas 3.4

and 3.5, which is given by [84]:

$$\ln\left[f_{Z|\mathcal{H}_0}(z)\right] \gtrless_1^0 \ln\left[f_{Z|\mathcal{H}_1}(z)\right]$$
$$-\ln\left(\text{Var}_0^{\text{SA}}\right) - \frac{|z|^2}{\text{Var}_0^{\text{SA}}} \gtrless_1^0 -\ln\left(\text{Var}_1^{\text{SA}}\right) - \frac{|z|^2}{\text{Var}_1^{\text{SA}}} \implies |z|^2 \gtrless_0^1 \ln\left(\frac{\text{Var}_1^{\text{SA}}}{\text{Var}_0^{\text{SA}}}\right)\frac{\text{Var}_1^{\text{SA}}\text{Var}_0^{\text{SA}}}{\text{Var}_1^{\text{SA}} - \text{Var}_0^{\text{SA}}},$$

where z is the mean of signal samples. The value of the optimal detection threshold T_{SA} is given by the decision rule.

The decision rule of the optimal detection is only dependent on $|Z|^2$. The variable $|Z|^2$ is an exponential distributed RV, whose mean parameter equals the variance of the complex Gaussian. Assuming that the prior probabilities of the two hypotheses are equal, the conditional BER can be derived as:

$$\begin{aligned}
P_{\text{SA}}(e) &= P(\mathcal{H}_0)P_{\text{SA}}(e|\mathcal{H}_0) + P(\mathcal{H}_1)P_{\text{SA}}(e|\mathcal{H}_1) \\
&= \frac{1}{2}\left(Pr\left\{|Z|^2 > T_{\text{SA}}|\mathcal{H}_0\right\} + Pr\left\{|Z|^2 < T_{\text{SA}}|\mathcal{H}_1\right\}\right) \\
&= \frac{1}{2}\left(1 - F_{\text{exp}}\left(T_{\text{SA}}, \text{Var}_0^{\text{SA}}\right) + F_{\text{exp}}\left(T_{\text{SA}}, \text{Var}_1^{\text{SA}}\right)\right) = \frac{1}{2} - \frac{1}{2}e^{-\frac{T_{\text{SA}}}{\text{Var}_1^{\text{SA}}}} + \frac{1}{2}e^{-\frac{T_{\text{SA}}}{\text{Var}_0^{\text{SA}}}},
\end{aligned}$$

where $F_{\text{Exp}}(x, \lambda)$ is the cumulative distribution function of the exponential RV $|Z|^2$.

B.5 Proof of Lemma 3.8

The antenna gain $\tilde{\mathbf{a}}^*\hat{\mathbf{K}}_{\tilde{\mathbf{W}}}^{-\mathbf{1}}\tilde{\mathbf{a}}$ of the receiver is dependent on the inverse of $\hat{\mathbf{K}}_{\tilde{\mathbf{W}}}$, for which closed-form expression can be obtained. The matrix $\hat{\mathbf{K}}_{\tilde{\mathbf{W}}}$ can be re-written as $\hat{\mathbf{K}}_{\tilde{\mathbf{W}}} = \mathbf{I}_{M_r-1} + \mathbf{J}_{M_r-1}$, where $\mathbf{I}_{M_r-1}$ is an identity matrix and $\mathbf{J}_{M_r-1}$ is an all-ones matrix whose rank will be one. Therefore, $\mathbf{J}_{M_r-1}$ can be simplified using singular value decomposition (SVD) as $\mathbf{u}_1\sigma_1\mathbf{v}_1^T$, where the unitary matrices are given by $\mathbf{u}_1 = \mathbf{v}_1 = \frac{-1}{\sqrt{M_r-1}}\begin{bmatrix}1 & 1 & \dots & 1\end{bmatrix}^T$, and the non-zero singular value $\sigma_1 = M_r - 1$. Due to the symmetry, this can be re-written in the form $\mathbf{J}_{M_r-1} = \mathbf{u}\mathbf{u}^T$, where $\mathbf{u} = \begin{bmatrix}1 & 1 & \dots & 1\end{bmatrix}^T$. Now, according to the Sherman-Morrison formula [107], inverse of the sum of a invertible matrix $\mathbf{A}$ and the outer product $\mathbf{u}\mathbf{v}^T$ is given by $\left(\mathbf{A} + \mathbf{u}\mathbf{v}^T\right)^{-1} = \mathbf{A}^{-1} - \frac{\mathbf{A}^{-1}\mathbf{u}\mathbf{v}^T\mathbf{A}^{-1}}{1 + \mathbf{v}^T\mathbf{A}^{-1}\mathbf{u}}$. The Sherman-Morrison formula is considered as a special case of the Woodbury matrix identity [107]. Using this, the inverse of $\hat{\mathbf{K}}_{\tilde{\mathbf{W}}}$ can be derived as:

$$\hat{\mathbf{K}}_{\tilde{\mathbf{W}}}^{-\mathbf{1}} = \mathbf{I}_{M_r-1} - \frac{\mathbf{u}\mathbf{u}^T}{1 + \mathbf{u}^T\mathbf{u}} = \mathbf{I}_{M_r-1} - \frac{\mathbf{J}_{M_r-1}}{M_r}. \tag{B.8}$$

The expression of the SNR gain $\tilde{\mathbf{a}}^*\hat{\mathbf{K}}_{\tilde{\mathbf{W}}}^{-\mathbf{1}}\tilde{\mathbf{a}}$ can be simplified as follows:

$$\tilde{\mathbf{a}}^*\hat{\mathbf{K}}_{\tilde{\mathbf{W}}}^{-\mathbf{1}}\tilde{\mathbf{a}} = \begin{bmatrix} e^{-j(\phi_2-\phi_1)} - 1 \\ \vdots \\ e^{-j(M_r-1)(\phi_2-\phi_1)} - 1 \end{bmatrix}^T \begin{bmatrix} \frac{M_r-1}{M_r} & \frac{-1}{M_r} & \dots & \frac{-1}{M_r} \\ \vdots & \vdots & \ddots & \vdots \\ \frac{-1}{M_r} & \frac{-1}{M_r} & \dots & \frac{M_r-1}{M_r} \end{bmatrix} \begin{bmatrix} e^{j(\phi_2-\phi_1)} - 1 \\ \vdots \\ e^{j(M_r-1)(\phi_2-\phi_1)} - 1 \end{bmatrix}$$

$$= \sum_{i=1}^{M_r-1} \left[e^{ji(\phi_2-\phi_1)} - 1\right]\left[e^{-ji(\phi_2-\phi_1)} - 1\right] - \frac{S_{M_r-1}S^*_{M_r-1}}{M_r} = -S_{M_r-1} - S^*_{M_r-1} - \frac{S_{M_r-1}S^*_{M_r-1}}{M_r},$$

where $S_{M_r-1} = \sum_{i=1}^{M_r-1} \left[e^{ji(\phi_2-\phi_1)} - 1\right]$ is the summation of all the elements in the weight vector. Since, S_{M_r-1} is a geometric sum it can be simplified, and the sum $S_{M_r-1}+S^*_{M_r-1}$ and product $S_{M_r-1}S^*_{M_r-1}$ can be derived as following:

$$\begin{aligned} S_{M_r-1} + S^*_{M_r-1} &= 2\frac{\sin\left((M_r-1)\frac{\phi_2-\phi_1}{2}\right)}{\sin\left(\frac{\phi_2-\phi_1}{2}\right)}\cos\left(\frac{M_r}{2}(\phi_2-\phi_1)\right) - 2(M_r-1) \\ S_{M_r-1}S^*_{M_r-1} &= \frac{\sin^2\left((M_r-1)\frac{\phi_2-\phi_1}{2}\right)}{\sin^2\left(\frac{\phi_2-\phi_1}{2}\right)} + (M_r-1)^2 \\ &\quad - 2(M_r-1)\frac{\sin\left((M_r-1)\frac{\phi_2-\phi_1}{2}\right)}{\sin\left(\frac{\phi_2-\phi_1}{2}\right)}\cos\left(\frac{M_r}{2}(\phi_2-\phi_1)\right). \end{aligned}$$

Using these simplifications, the final expression for the SNR gain can be determined as follows:

$$\tilde{\mathbf{a}}^*\hat{\mathbf{K}}^{-1}_{\tilde{\mathbf{w}}}\tilde{\mathbf{a}} = M_r - \frac{1}{M_r} - \frac{2}{M_r}\frac{\sin\left((M_r-1)\frac{\phi_2-\phi_1}{2}\right)}{\sin\left(\frac{\phi_2-\phi_1}{2}\right)}\cos\left(\frac{M_r}{2}(\phi_2-\phi_1)\right) - \frac{1}{M_r}\frac{\sin^2\left((M_r-1)\frac{\phi_2-\phi_1}{2}\right)}{\sin^2\left(\frac{\phi_2-\phi_1}{2}\right)}.$$

B.6 Proof of Lemma 3.10

The effective signal $y_{\text{eff}}[n]$, given in (3.22), under $\mathcal{H}_0$ is a complex Gaussian RV with variance σ_n^2. Hence, the mean Z of the received samples under $\mathcal{H}_0$ is a complex Gaussian RV with variance $\text{Var}_0^{\text{MA}} = \frac{\sigma_n^2}{N}$. On the other hand, $y_{\text{eff}}[n]$ under $\mathcal{H}_1$ is the sum of a scaled version of the backscatter signal $y_b[n]$ in Lemma 3.5 with the same receiver noise variance. Using the procedure similar to the ones in Lemmas 3.4 and 3.5, the mean Z of the received samples under $\mathcal{H}_1$ can also be shown to follow a complex Gaussian distribution, the variance of which is given by

$$\text{Var}_1^{\text{MA}} = \frac{G|\alpha|^2\sigma_h^4\left\{\mathbb{E}\left[|X|^2\right] + \frac{2\rho_t\rho_b}{1-\rho_t\rho_b}\left(1 - \frac{1-\rho_t^N\rho_b^N}{N(1-\rho_t\rho_b)}\right)|\mathbb{E}\left[X\right]|^2\right\} + \sigma_n^2}{N}.$$

B.7 Proof of Theorem 3.11

By comparing the conditional PDFs of the two hypotheses given in (3.24), the optimal detection threshold T_{MA} can be obtained. The conditional BER, evaluated using a procedure similar to the one used in the case of SA receiver, is a function of the phase-offsets of the DL and BL links, and the average BER is obtained by marginalizing the conditional BER over the

variables θ_1 and θ_2. The assumption here is that θ_1 and θ_2 are i.i.d. and uniformly distributed over $(-\pi, \pi]$, and the final expression in the result can be obtained by marginalizing over this range of θ_1 and θ_2. One can choose more complex distributions of AoAs to model different scenarios.

Appendix C

C.1 Proof of Lemma 4.1

The test statistics Z_0 and Z_1 are correlated due to the common signal component from the DL present in the two codeword symbols. And, since they are jointly Gaussian, deriving covariance for the two symbols in addition to their individual variances is sufficient. The joint distribution of the bivariate Gaussian random variables is given by:

$$f_{Z_0,Z_1}(z_0, z_1) = \frac{1}{\pi^2 |C_z|^{1/2}} e^{-\frac{1}{2}(z-m)^H C_z^{-1}(z-m)}, \tag{C.1}$$

where the mean in this case is $m = E[Z_0 Z_1] = \bar{0}$ since the channel is Rayleigh faded, and from this the covariance matrix also simplifies as follows:

$$C_z = \begin{bmatrix} \mathrm{Var}[Z_0] & \bar{\mathrm{Cov}}[Z_0, Z_1] \\ \mathrm{Cov}[Z_0, Z_1] & \mathrm{Var}[Z_1] \end{bmatrix}.$$

The covariance is non-zero as a result of the DL present in the two consecutive symbols, and it can be easily verified that $\mathrm{Cov}[Z_0, Z_1] = \bar{\mathrm{Cov}}[Z_0, Z_1]$ from the symmetry of the problem (and therefore real). Due to this symmetry, it is enough to evaluate $\mathrm{Cov}[Z_0, Z_1]$ under null hypothesis $\mathcal{H}_0$. The conditional covariance of any two samples $y[i]$ and $y[j]$, for $j > i$, is given by:

$$\begin{aligned}
&\mathrm{Cov}\left[y[i], y[j]\right] \overset{(a)}{=} \mathbb{E}\left[y[i] y^*[j]\right] \\
&= \mathbb{E}\Bigg[(\rho_r^{i+j-2}|h_r[1]|^2 + \sqrt{1-\rho_r^2}\sum_{k_2=1}^{j-1}\rho_r^{i+j-k_2-2} h_r[1] g_r^*[k_2]) x[i] x^*[j] + \rho_r^{i-1} h_r[1] x[i] w^*[j] \\
&+ \sqrt{1-\rho_r^2}\sum_{k_1=1}^{i-1}\rho_r^{i+j-k_1-2} h_r^*[1] g_r[k_1] + (1-\rho_r^2)\sum_{k_1=1}^{i-1}\sum_{k_2=1}^{j-1}\rho_r^{i+j-k_1-k_2-2} g_r[k_1] g_r^*[k_2]) x[i] x^*[j] \\
&+ \sqrt{1-\rho_r^2}\sum_{k_1=1}^{i-1}\rho_r^{i-k_1-1} w^*[j] g_r[k_1] x[i] + \rho_r^{j-1} h_r[1] x^*[j] w[i] \\
&+ \sqrt{1-\rho_r^2}\sum_{k_2=1}^{j-1}\rho_r^{j-k_2-1} w[i] g_r^*[k_2] x^*[j] + w[i] w^*[j]\Bigg] \\
&= \sigma_h^2 \rho_r^{i+j-2} + (1-\rho_r^2)\sum_{k=1}^{i-1}\rho_r^{i+j-2k-2}) x[i] x^*[j] = \sigma_h^2 \rho_r^{j-i} x[i] x^*[j],
\end{aligned}$$

where (a) follows from the fact that the conditional expectation of the samples is zero. The covariance $\mathrm{Cov}^{\mathrm{SA}}$ can be evaluated as:

$$\mathrm{Cov}^{\mathrm{SA}} = \mathrm{Cov}[Z_0, Z_1] = \frac{4}{N^2}\Big(\sum_{n_1,n_2} \mathrm{Cov}\left[y[n_1], y[n_2]\right]\Big)$$
$$= \frac{4\sigma_h^2}{N^2}\sum_{n_1=1}^{N/2}\sum_{n_2=N/2+1}^{N}\rho_r^{n_2-n_1}x[n_1]x^*[n_2] = \frac{4\rho_r(1-\rho_r^{N/2})^2}{N^2(1-\rho_r)^2}|\mathbb{E}[X]|^2.$$

For the null hypothesis $\mathcal{H}_0$, the variances $\mathrm{Var}[Z_0]$ and $\mathrm{Var}[Z_1]$ are given by $\mathrm{Var}_0^{\mathrm{SA}}$ and $\mathrm{Var}_1^{\mathrm{SA}}$, respectively, whose derivations follow a procedure similar to the one used for $\mathrm{Cov}^{\mathrm{SA}}$. These derivations are, therefore, skipped here due to space constraints, and interested readers can refer to [25, Lemmas 2 and 3] for the details. The variances of $\mathcal{H}_0$ are simply exchanged to get the respective variances of Z_0 and Z_1 under the alternate hypothesis $\mathcal{H}_1$.

C.2 Proof of Theorem 4.2

Comparing the joint conditional PDFs derived in Lemma 4.1, the optimal decision rule can be obtained as:

$$\begin{aligned}
&\ln\left[f_{Z_0,Z_1|\mathcal{H}_0}(z_0,z_1)\right] \gtrless_1^0 \ln\left[f_{Z_0,Z_1|\mathcal{H}_1}(z_0,z_1)\right] \\
&\implies -|z_0|^2\,\mathrm{Var}_1^{\mathrm{SA}} - |z_1|^2\,\mathrm{Var}_0^{\mathrm{SA}} + (z_0z_1^* + z_0^*z_1)\mathrm{Cov}^{\mathrm{SA}} \\
&\gtrless_1^0 -|z_0|^2\,\mathrm{Var}_0^{\mathrm{SA}} - |z_1|^2\,\mathrm{Var}_1^{\mathrm{SA}} + (z_0z_1^* + z_0^*z_1)\mathrm{Cov}^{\mathrm{SA}} \\
&\implies |z_0|^2 \gtrless_0^1 |z_1|^2.
\end{aligned} \tag{C.2}$$

Since the two hypotheses are symmetric, it is sufficient to evaluate the average BER for the null hypothesis $\mathcal{H}_0$, which is evaluated using the joint PDF as follows:

$$P_{\mathrm{SA}}(e) = Pr\left\{|Z_0|^2 > |Z_1|^2 \,|\, \mathcal{H}_0\right\} = \int_0^\infty\int_v^\infty f_{|Z_0|^2,|Z_1|^2}(u,v)\,\mathrm{d}u\,\mathrm{d}v$$
$$\overset{(a)}{=} \int_0^\infty\int_v^\infty \frac{\exp\left\{-\left(\frac{u}{(1-\rho^2)\mathrm{Var}[Z_0]} + \frac{v}{(1-\rho^2)\mathrm{Var}[Z_1]}\right)\right\}}{\pi(1-\rho^2)\mathrm{Var}[Z_0]\mathrm{Var}[Z_1]} I_0\Big(\frac{\rho\sqrt{uv}}{(1-\rho^2)\sqrt{\mathrm{Var}[Z_0]\mathrm{Var}[Z_1]}}\Big)\,\mathrm{d}u\,\mathrm{d}v,$$

where (a) results from the fact that the joint distribution of magnitude squares of the bi-variate Gaussian random variables is characterized as a bi-variate Rayleigh [108].

From the expressions given for $\mathrm{Var}_0^{\mathrm{SA}}$, $\mathrm{Var}_1^{\mathrm{SA}}$ and $\mathrm{Cov}^{\mathrm{SA}}$ in Lemma 4.1, one can conclude that the covariance $\mathrm{Cov}^{\mathrm{SA}}$ decays faster compared to the variances $\mathrm{Var}_0^{\mathrm{SA}}$ and $\mathrm{Var}_1^{\mathrm{SA}}$. Hence, for a sufficiently large value of the sample-size N, the random variables $|Z_0|^2$ and $|Z_1|^2$ can be approximated as independent. Consequently, the joint distribution of $|Z_0|^2$ and $|Z_1|^2$ simplifies to the product of their marginal distributions. Note that the marginal PDFs of

$|Z_0|^2$ and $|Z_1|^2$ are exponential. Due to the symmetry present in the two hypotheses of the problem, we only need to derive the error probability for $\mathcal{H}_0$. The derivation for the theoretical average BER of the SA receiver is given as follows:

$$\begin{aligned}P_{\mathrm{SA}}(e) &= Pr\left\{|Z_0|^2 > |Z_1|^2 \,|\, \mathcal{H}_0\right\} = Pr\left\{|Z_0|^2 > t \,|\, |Z_1|^2 = t, \mathcal{H}_0\right\} \\ &= \int_0^\infty \left[1 - F_{\mathrm{Exp}}\left(t, \mathrm{Var}_0^{\mathrm{SA}}\right)\right] f_{\mathrm{Exp}}\left(t, \mathrm{Var}_1^{\mathrm{SA}}\right)\, \mathrm{d}t \\ &= \int_0^\infty e^{-\frac{t}{\mathrm{Var}_0^{\mathrm{SA}}}} \frac{e^{-\frac{t}{\mathrm{Var}_1^{\mathrm{SA}}}}}{\mathrm{Var}_1^{\mathrm{SA}}}\, \mathrm{d}t = \int_0^\infty \frac{e^{-t\left(\frac{1}{\mathrm{Var}_0^{\mathrm{SA}}} + \frac{1}{\mathrm{Var}_1^{\mathrm{SA}}}\right)}}{\mathrm{Var}_1^{\mathrm{SA}}}\, \mathrm{d}t = \left(1 + \frac{\mathrm{Var}_1^{\mathrm{SA}}}{\mathrm{Var}_0^{\mathrm{SA}}}\right)^{-1},\end{aligned}$$

where $F_{\mathrm{Exp}}(x, \lambda)$ and $f_{\mathrm{Exp}}(x, \lambda)$ are the cumulative distribution function and the PDF of an exponential RV with mean λ, respectively.

C.3 Proof of Theorem 4.4

Since the DL is canceled in the MA receiver, no correlation exists between the two variables Z_0 and Z_1 of the codeword. Hence, the conditional joint PDFs of Z_0 and Z_1 are given by:

$$\mathcal{H}_0 \begin{cases} Z_0 \sim \mathcal{CN}\left(0, \mathrm{Var}_0^{\mathrm{MA}}\right) \\ Z_1 \sim \mathcal{CN}\left(0, \mathrm{Var}_1^{\mathrm{MA}}\right), \end{cases} \quad \mathcal{H}_1 \begin{cases} Z_0 \sim \mathcal{CN}\left(0, \mathrm{Var}_1^{\mathrm{MA}}\right) \\ Z_1 \sim \mathcal{CN}\left(0, \mathrm{Var}_0^{\mathrm{MA}}\right), \end{cases}$$

where $\mathrm{Var}_1^{\mathrm{MA}} = \frac{G|\alpha|^2\sigma_h^4\left\{\mathbb{E}\left[|X|^2\right] + \frac{2\rho_t\rho_b}{1-\rho_t\rho_b}\left(1 - \frac{1-\rho_t^N\rho_b^N}{N(1-\rho_t\rho_b)}\right)|\mathbb{E}[X]|^2\right\} + \sigma_n^2}{N}$ and $\mathrm{Var}_0^{\mathrm{MA}} = \frac{\sigma_n^2}{N}$ are the variances of the MA receiver as derived in [25] for the direct OOK modulation. The optimal decision rule once again turns out to be (C.2), from which the conditional BER can be derived as:

$$P(e|\phi_1, \phi_2) = \left(1 + \frac{\mathrm{Var}_1^{\mathrm{MA}}}{\mathrm{Var}_0^{\mathrm{MA}}}\right)^{-1} = \frac{\sigma_n^2}{G|\alpha|^2\sigma_h^4\left\{\mathbb{E}[|X|^2] + \frac{2\rho_t\rho_b}{1-\rho_t\rho_b}\left(1 - \frac{2(1-\rho_t^{\frac{N}{2}}\rho_b^{\frac{N}{2}})}{N(1-\rho_t\rho_b)}\right)|\mathbb{E}[X]|^2\right\} + 2\sigma_n^2}.$$

Since the antenna gain depends on the phase offsets of the two links (and thereby their AoAs), the average BER is derived by marginalizing over the range $(-\pi, \pi]$ of the AoAs θ_1 and θ_2.

Appendix D

D.1 Proof of Lemma 5.1

Since expectation is a linear operator, the evaluation of the expectation of the sum sequence S_N is straight-forward and is given by:

$$\mathbb{E}\left[S_N\right] = \mathbb{E}\left[\sum_{n_1,n_2} x[n_1]x^*[n_2]\right] = \sum_{n}\mathbb{E}\left[|x[n]|^2\right] + \sum_{n_1\neq n_2}\mathbb{E}\left[x[n_1]\right]\mathbb{E}\left[x^*[n_2]\right]$$
$$\overset{(a)}{=}\sum_{n}\mathbb{E}\big[|X|^2\big]+\sum_{n_1\neq n_2}|\mathbb{E}[X]|^2 = N\mathbb{E}\big[|X|^2\big]+N(N-1)|\mathbb{E}[X]|^2,$$

where (a) follows from the i.i.d. assumption of the sequence $x[n]$. Hence, the asymptotic growth rate of the expectation is of the order of N^2, i.e., $\mathbb{E}\left[S_N\right] = \Theta(N^2)$. From this, the expectation of $M_N = \frac{S_N}{N}$ can be easily derived as given in (3.11), for which the asymptotic growth rate is $\Theta[N]$. Now coming to the variance of S_N, it can be first simplified as follows:

$$\mathrm{Var}\left[S_N\right] = \mathbb{E}\left[\Big(\sum_{i_1,j_1} x[i_1]x^*[j_1]\Big)\Big(\sum_{i_2,j_2} x^*[i_2]x[j_2]\Big)\right] - \mathbb{E}\left[S_N\right]^2$$
$$= \mathbb{E}\left[\sum_{i_1}\sum_{i_2}|x[i_1]|^2|x[i_2]|^2 + 2\sum_{i_1}\sum_{i_2\neq j_2}|x[i_1]|^2x^*[i_2]x[j_2] + \sum_{i_1\neq j_1}\sum_{i_2\neq j_2}x[i_1]x^*[j_1]x^*[i_2]x[j_2]\right] - \mathbb{E}[S_N]^2$$
$$\overset{(b)}{=} \sum_{i_1=i_2}\mathbb{E}\left[|X|^4\right] + \left\{\sum_{i_1\neq i_2}1 + \sum_{i_1\neq j_1}1 - \big(\sum_{i}1\big)^2\right\}\left(\mathbb{E}\left[|X|^2\right]\right)^2 + 2\sum_{i_1\neq j_2}\mathbb{E}\left[X(X^*)^2\right]\mathbb{E}\left[X\right]$$
$$+2\sum_{i_1\neq i_2}\mathbb{E}\left[(X)^2X^*\right]\mathbb{E}\left[X^*\right] + 2\left\{\sum_{i_1\neq i_2\neq j_2}1 + \sum_{i_1\neq j_1\neq j_2}1 - \sum_{i,i_1\neq i_2}1\right\}\mathbb{E}\big[|X|^2\big]\left|\mathbb{E}\left[X\right]\right|^2 + \sum_{i_1\neq i_2\neq j_1}\mathbb{E}\left[X^2\right]\left(\mathbb{E}\left[X^*\right]\right)^2$$
$$+\sum_{i_1\neq j_1\neq j_2}\left(\mathbb{E}\left[X^2\right]\right)^*\left(\mathbb{E}\left[X\right]\right)^2 + \sum_{i_1\neq j_1}\left|\mathbb{E}\left[X^2\right]\right|^2 + \left\{\sum_{i_1\neq j_1\neq i_2\neq j_2}1 - \big(\sum_{i_1\neq i_2}1\big)^2\right\}\left|\mathbb{E}\left[X\right]\right|^4, \tag{D.1}$$

where (b) follows from the piece-wise separation of the independent summation terms by permuting the indices i_1, i_2, j_1 and j_2 of each term and the expansion of $\mathbb{E}\left[S_N\right]$. The coefficient of each of the term in (D.1) can be shown to be proportional to either N^2 or N^3. As a result, the growth rate of the variance of S_N and M_N can be shown as $\Theta[N^3]$ and $\Theta[N]$, respectively. The result in (3.11) follows from the fact that both the expectation and variance grow at the same order.

D.2 Proof of Lemma 5.3

Since the distribution of Z when conditioned on $x_1[n]$ is a complex Gaussian under null hypothesis $\mathcal{H}_0$, the expectation and variance of Z are sufficient to completely characterize its distribution which are given by:

$$\mathbb{E}[Z] = \mathbb{E}[h_r]\frac{\sum_{n=1}^{N} x_1[n]}{N} + \frac{\sum_{n=1}^{N}\mathbb{E}[w[n]]}{N} = 0,$$

$$\begin{aligned}\mathrm{Var}[Z] &= \frac{1}{N^2}\left(\mathrm{Var}\left[h_r\sum_{n=1}^{N}x_1[n]\right] + \mathrm{Var}\left[\sum_{n=1}^{N}w[n]\right]\right) = \frac{1}{N^2}\left(\sigma_h^2\sum_{1\le n_1,n_2\le N}x_1[n_1]x_1^*[n_2] + N\sigma_n^2\right)\\ &= \frac{1}{N}\left(\sigma_h^2\underbrace{\frac{\sum_{1\le n_1,n_2\le N}x_1[n_1]x_1^*[n_2]}{N}}_{M_N} + \sigma_n^2\right) \overset{(a)}{\approx} \frac{\sigma_h^2\left(\mathbb{E}[|X|^2] + (N-1)|\mathbb{E}[X]|^2\right) + \sigma_n^2}{N},\end{aligned}$$

where (a) is a consequence of approximating M_N with its expectation given by Lemma 5.1.

An approach similar to the one taken for time-selective fading in [25] is used to derive the distribution of Z under $\mathcal{H}_1$. There the statistic Z is divided into two components (a) and (b) given in (5.3), where the first one is common to both $\mathcal{H}_0$ and $\mathcal{H}_1$ while the second one is specific to $\mathcal{H}_1$. When conditioned on $x_2[n]$, the PDF of the second component is given by [106]:

$$f_U(u_1,u_2) = \frac{1}{2\pi\sigma_{\mathrm{SA}}^2}K_0\left(\sqrt{\tfrac{u_1^2+u_2^2}{\sigma_{\mathrm{SA}}^2}}\right), \text{ where } \sigma_{\mathrm{SA}}^2 = \frac{|\alpha|^2\sigma_h^4}{4}\left(\frac{\mathbb{E}[|X|^2] + (N-1)|\mathbb{E}[X]|^2}{N}\right).$$

The next steps follow the procedure of [20, Lemma 4] with minor variations, and are repeated here for completeness. The joint distribution of the real and imaginary components of (b) conditioned on (a) can be expressed in terms of the joint distribution of U as:

$$f_{(b)|(a)}(y_1,y_2) = f_U(y_1-v_1, y_2-v_2). \tag{D.2}$$

The joint distribution of the components (a) and (b) in (5.3) can be derived as follows:

$$\begin{aligned}f_{(a),(b)}(v_1,v_2,y_1,y_2) &\overset{(b)}{=} f_{(a)}(v_1,v_2)f_{(b)|(a)}(y_1,y_2|v_1,v_2) = f_{Y_{\mathcal{M}_1}|\mathcal{H}_0}(v_1,v_2)f_U(y_1-v_1,y_2-v_2)\\ &= \frac{1}{2\pi^2\sigma_{\mathrm{SA}}^2\mathrm{Var}_0^{\mathrm{SA}}}\exp(-\frac{v_1^2+v_2^2}{\mathrm{Var}_0^{\mathrm{SA}}})K_0\left(\sqrt{\tfrac{(y_1-v_1)^2+(y_2-v_2)^2}{\sigma_{\mathrm{SA}}^2}}\right),\end{aligned}$$

where (b) follows from de-conditioning of RVs through chain rule. By marginalizing the joint distribution over the domain of v_1 and v_2, we get the result in (5.5).

D.3 Proof of Lemma 5.4

The conditional PDFs of R and Φ under $\mathcal{H}_0$ can be directly inferred from the complex Gaussian distribution of Z. The derivation of the same conditional PDFs under $\mathcal{H}_1$ follows the same procedure as in [20, Lemma 4] with few modifications. The joint distribution of A_0 and Φ_0 of $\mathcal{H}_0$ and A_1 and Φ_1 of $\mathcal{H}_1$ can be derived using the relation between the polar RVs and their corresponding rectangular form RVs as:

$$\begin{aligned}
&f_{A_0,\Phi_0,A_1,\Phi_1}(a_0,\phi_0,a_1,\phi_1) = f_{A_0,\Phi_0}\left(a_0,\phi_0\right) f_{A_1,\Phi_1|A_0,\Phi_0}\left(a_1,\phi_1|a_0,\phi_0\right)\\
&\overset{(a)}{=} a_0\, f_{Y_{\mathcal{M}_1}|\mathcal{H}_0}\left(a_0\cos\phi_0, a_0\sin\phi_0\right) a_1 f_U\left(a_1\cos\phi_1 - a_0\cos\phi_0 a_1\sin\phi_1 - a_0\sin\phi_0\right)\\
&= \frac{a_0 a_1}{2\pi^2\sigma_{\text{SA}}^2\text{Var}_0^{\text{SA}}}\exp(-\frac{a_0^2}{\text{Var}_0^{\text{SA}}})K_0\left(\frac{\sqrt{a_1^2+a_0^2-2a_1a_0\cos(\phi_1-\phi_0)}}{\sigma_{\text{SA}}}\right),
\end{aligned} \tag{D.3}$$

where (a) follows from the relationship between the joint distribution functions of polar and rectangular RVs. We can obtain the joint marginal distribution of A_1 and A_0 by integrating over the domain of Φ_1 and Φ_0 but another simplification can be made to decrease the number of integrals. The joint distribution is just a function of the difference $\phi_1-\phi_0$, and thus we can further simplify it by replacing ϕ_1 with $\phi=\phi_1-\phi_0$. The modified joint distribution is given by:

$$f_{A_0,\Phi_0,A_1,\Phi}\left(a_0,\phi_0,a_1,\phi\right) = \frac{a_0 a_1\exp(-\frac{a_0^2}{\text{Var}_0^{\text{SA}}})}{2\pi^2\sigma_{\text{SA}}^2\text{Var}_0^{\text{SA}}}K_0\left(\frac{\sqrt{a_1^2+a_0^2-2a_1a_0\cos\phi}}{\sigma_{\text{SA}}^2}\right),$$

where $0\le\phi_0\le 2\pi$ and $-\phi_0\le\phi\le 2\pi-\phi_0$. The joint marginal distribution of A_1 and A_0, obtained by integrating over the domain of ϕ_1 and ϕ, is given by:

$$\begin{aligned}
f_{A_0,A_1}\left(a_0,a_1\right) &= \int_0^{2\pi}\int_{-\theta_{h_0}}^{2\pi-\theta_{h_0}} \frac{a_0 a_1\exp(-\frac{a_0^2}{\text{Var}_0^{\text{SA}}})}{2\pi^2\sigma_{\text{SA}}^2\text{Var}_0^{\text{SA}}}K_0\left(\frac{\sqrt{a_1^2+a_0^2-2a_1a_0\cos\phi}}{\sigma_{\text{SA}}^2}\right)\mathrm{d}\phi\,\mathrm{d}\phi_0\\
&\overset{(b)}{=} \int_0^{2\pi}\int_0^{2\pi}\frac{a_0 a_1\exp(-\frac{a_0^2}{\text{Var}_0^{\text{SA}}})}{2\pi^2\sigma_{\text{SA}}^2\text{Var}_0^{\text{SA}}}K_0\left(\frac{\sqrt{a_1^2+a_0^2-2a_1a_0\cos\phi}}{\sigma_{\text{SA}}^2}\right)\mathrm{d}\phi\,\mathrm{d}\phi_0\\
&\overset{(c)}{=} \int_0^{\pi}\frac{2a_0 a_1\exp(-\frac{a_0^2}{\text{Var}_0^{\text{SA}}})}{\pi\sigma_{\text{SA}}^2\text{Var}_0^{\text{SA}}}K_0\left(\frac{\sqrt{a_1^2+a_0^2-2a_1a_0\cos\phi}}{\sigma_{\text{SA}}^2}\right)\mathrm{d}\phi,
\end{aligned}$$

where (b) follows from the periodicity of $\cos\theta$ which is 2π, and (c) follows from marginalizing the PDF over the range of ϕ_0 and the symmetry of $\cos\phi$ around $\phi=\pi$.

Finally, the joint distribution of magnitude squares of A_1 and A_0, given by R_1 and R_0 respectively, can be derived as:

$$f_{R_0,R_1}(r_0,r_1)\overset{(d)}{=}\frac{1}{4\sqrt{r_0r_1}}f_{A_0,A_1}(\sqrt{r_0},\sqrt{r_1}) = \frac{\exp(-\frac{r_0}{\text{Var}_0^{\text{SA}}})}{2\pi\sigma_{\text{SA}}^2\text{Var}_0^{\text{SA}}}\int_0^{\pi}K_0\left(\sqrt{\frac{r_1+r_0-2\sqrt{r_1r_0}\cos\phi}{\sigma_{\text{SA}}^2}}\right)\mathrm{d}\phi,$$

where (d) follows from the relation between the joint PDFs of the modulus and the square of modulus of the RVs.

The marginal distribution of magnitude square of Z can be obtained by integrating over R_0, and by substituting $R|\mathcal{H}_1, r$ and a in place of R_1, r_1 and r_0, respectively:

$$f_{R|\mathcal{H}_1}(r) = \int_0^{\infty}\int_0^{\pi} \frac{\exp(-\frac{a}{\mathrm{Var}_0^{\mathrm{SA}}})}{2\pi\sigma_{\mathrm{SA}}^2 \mathrm{Var}_0^{\mathrm{SA}}} K_0\left(\sqrt{\frac{r+a-2\sqrt{ra}\cos\phi}{\sigma_{\mathrm{SA}}^2}}\right) \mathrm{d}\phi \mathrm{d}a.$$

On the other hand, the marginal distribution of Φ_1 can be obtained similarly by integrating over the domain of A_1, A_0 and Φ_0 of (D.3), and by substituting $\Phi|\mathcal{H}_1, \phi$ and λ in place of Φ_1, ϕ_1 and ϕ_0, respectively:

$$\begin{aligned} f_{\Phi|\mathcal{H}_1}(\phi) &= \int_0^{2\pi}\int_0^{\infty}\int_0^{\infty} \frac{a_0 a_1 \exp(-\frac{a_0^2}{\mathrm{Var}_0^{\mathrm{SA}}})}{2\pi^2\sigma_{\mathrm{SA}}^2 \mathrm{Var}_0^{\mathrm{SA}}} K_0\left(\frac{\sqrt{a_1^2+a_0^2-2a_1a_0\cos(\phi-\lambda)}}{\sigma_{\mathrm{SA}}^2}\right) \mathrm{d}a_1\, \mathrm{d}a_0\, \mathrm{d}\lambda \\ &\overset{(e)}{=} \int_0^{2\pi}\int_0^{\infty}\int_0^{\infty} \frac{\exp(-\frac{a}{\mathrm{Var}_0^{\mathrm{SA}}})}{2\pi^2\sigma_{\mathrm{SA}}^2 \mathrm{Var}_0^{\mathrm{SA}}} K_0\left(\frac{\sqrt{a+b-2\sqrt{ab}\cos(\phi-\lambda)}}{\sigma_{\mathrm{SA}}^2}\right) \mathrm{d}a\, \mathrm{d}b\, \mathrm{d}\lambda, \end{aligned}$$

where (e) follows from changing the integrals of a_0 and a_1 to $a = a_0^2$ and $b = a_1^2$ respectively.

D.4 Proof of Theorem 5.5

The derivation follows the approach used in the time-selective fading model [26]. Similar to that, equal prior probabilities are assumed for the two hypotheses. The equation for the average BER of $\mathcal{M}_1$ in block fading is given by:

$$\begin{aligned} P_{\mathrm{SA}}(e) &= P(\mathcal{H}_0)P_{\mathrm{SA}}(e|\mathcal{H}_0) + P(\mathcal{H}_1)P_{\mathrm{SA}}(e|\mathcal{H}_1) = \frac{1}{2}(\Pr\{R > T_{\mathrm{SA}}|\mathcal{H}_0\} + \Pr\{R < T_{\mathrm{SA}}|\mathcal{H}_1\}) \\ &= \frac{1}{2}\left(1 - F_{\exp}\left(T_{\mathrm{SA}}, \mathrm{Var}_0^{\mathrm{SA}}\right) + \int_0^{T_{\mathrm{SA}}} f_{R|\mathcal{H}_1}(r)\, \mathrm{d}r\right), \end{aligned}$$

where $F_{\exp}(x, \lambda) = 1 - e^{-\frac{x}{\lambda}}$ is the CDF value of an exponential RV with mean λ at point x. Substituting the distributions with their expressions will result in (5.10).

D.5 Proof of Lemma 5.7

The characteristic function of the interference term I_{PS} can be evaluated as follows:

$$\varphi_{I_{\mathrm{PS}}}(t) = E[e^{itI_{\mathrm{PS}}}] = E[e^{it\sum\limits_{X_i\in\Phi_{\mathrm{PS}_0}} L(||X_i||)}] = E\left[\prod_{X_i\in\Phi_{\mathrm{PS}_0}} e^{itL(||X_i||)}\right]$$

$$\overset{(a)}{=} \exp\left(-\frac{\lambda_{BN}}{M}\int_{R^2}(1-e^{itL(||X_i||)})\,\mathrm{d}||x_i||\right) \overset{(b)}{=} \exp\left(-2\pi\frac{\lambda_{PS}}{M}\int_0^\infty (1-e^{itL(v)})v\,\mathrm{d}v\right) \quad \text{(D.4)}$$

where (a) follows from the PGFL of the homogeneous PPP, and (b) follows from the transformation of coordinates from Cartesian to polar domain. Similarly, the characteristic function of I_{BN} can be determined as follows:

$$\varphi_{I_{\mathrm{BN}}}(t) = E[e^{itI_{\mathrm{BN}}}] = E_{X_j,T_j}\left[e^{it|\alpha|^2\sum\limits_{X_j\in\Phi'_{\mathrm{BN}_0}\setminus\{0\}} L(||T_j||)L(||X_j||)}\right] = E_{X_j,T_j}\left[\prod_{X_j\in\Phi'_{\mathrm{BN}_0}\setminus\{0\}} e^{it|\alpha|^2L(||T_j||)L(||X_j||)}\right]$$

$$\overset{(c)}{=} E_{X_j}\left[\prod_{X_j\in\Phi'_{\mathrm{BN}_0}\setminus\{0\}} E_{T_j}\left[e^{it|\alpha|^2L(||T_j||)L(||X_j||)}\right]\right] \overset{(d)}{=} \exp\left(-\frac{\lambda_{BN}}{2M}\int_{\mathbb{R}^2}\left(1-E_{T_j}\left[e^{it|\alpha|^2L(||T_j||)L(||x||)}\right]\right)\,\mathrm{d}||x||\right)$$

$$\overset{(e)}{=} \exp\left(-2\pi\frac{\lambda_{BN}}{2M}\int_0^\infty\left(1-E_{U_j}\left[e^{it|\alpha|^2L(U_j)L(v)}\right]\right)v\,\mathrm{d}v\right)$$

$$= \exp\left(-2\pi\frac{\lambda_{BN}}{2M}\int_0^\infty\left(1-\int_0^\infty f_U(u)e^{it|\alpha|^2L(u)L(v)}\,\mathrm{d}u\right)v\,\mathrm{d}v\right), \quad \text{(D.5)}$$

where (c) follows from moving the expansion of the expectation with respect to N, and the independence and identical nature of X_j and T_j, (d) follows from the property of the PPP and Slivnyak's theorem, and (e) follows from the expansion of the expectation with respect to X_j and T_j.

D.6 Proof of Theorem 5.8

Suppose that the distance from the BN-Rx pair of interest and the distance of the BN to its ambient PS are represented as $V_0 = ||X_0||$ and $U_0 = ||T_0||$, respectively. Then, conditioning on the distances V_0 and U_0, the CCDF of SINR in (5.26) can be evaluated as follows:

$$\bar{F}_{\mathrm{SINR}}(x) = P\left[\mathrm{SINR} > x\right] = P\left[\frac{|\alpha|^2L(U_0)L(V_0)}{I+\mathrm{SNR}^{-1}} > x\right] = P\left[I < \frac{|\alpha|^2L(U_0)L(V_0)}{T} - \mathrm{SNR}^{-1}\right]$$

$$= E_{U_0,V_0}\left[P\left[I < \frac{|\alpha|^2L(U_0)L(V_0)}{x} - \mathrm{SNR}^{-1}|U_0=u_0,V_0=v_0\right]\right]$$

$$= \int_0^\infty\int_0^\infty F_I\left(\frac{|\alpha|^2L(u_0)L(v_0)}{x} - \mathrm{SNR}^{-1}\right)f_{U_0,V_0}(u_0,v_0)\,\mathrm{d}u_0\,\mathrm{d}v_0. \quad \text{(D.6)}$$

The CDF F_I of the interference can be evaluated from its characteristic function using the Gil-Pelaz theorem as follows:

$$F_I(x) = \frac{1}{2} + \frac{1}{2\pi}\int_0^\infty \frac{e^{itx}\varphi_I(-t) - e^{-itx}\varphi_I(t)}{it}\mathrm{d}t = \frac{1}{2} - \frac{1}{\pi}\int_0^\infty \mathrm{Im}\left(\frac{e^{-itx}\varphi_I(t)}{t}\right)\mathrm{d}t. \quad \text{(D.7)}$$

For averaging, the expectation of the conditional BER can be evaluated using the following relation for the complementary cumulative distribution function (CCDF) $\bar{F}_X(x)$ of the function of a random variable X with non-zero support as follows:

$$P(e) = E_{\text{SINR}}[g(\text{SINR})] = -g(x)\bar{F}_{\text{SINR}}(x)\Big|_0^\infty + \int_0^\infty \bar{F}_{\text{SINR}}(x)g'(x)\,\mathrm{d}x$$
$$= \frac{1}{2} + \int_0^\infty \bar{F}_{\text{SINR}}(x)g'(x)\,\mathrm{d}x, \tag{D.8}$$

where $g(x) = 0|_{x=\infty}$ and $g(x) = 0.5|_{x=0}$ since the conditional BER in (5.25) converge to same values at ∞ and 0. The derivative of $g(x)$ for the uncoded scheme OOK modulation scheme is given by:

$$g'(x) = -(1+x)^{-1-\frac{1}{x}}\frac{\ln(1+x)}{2x}. \tag{D.9}$$

After substituting the individual components in (D.8) and simplifying further, the expression given in the result is obtained.

D.7 Proof of Lemma 5.9

The characteristic function of the interference I can be evaluated as follows:

$$\varphi_I(t) = E[e^{itI}] = E[e^{it\sum\limits_{Y_i\in\Phi_{\text{int}}\setminus\{Y_1\}} G(\Theta_i,\Theta_1)L(||Y_i||)}] = E_{\Phi_{\text{int}},\Theta_i,\Theta_1,P_1}\left[\prod_{Y_i\in\Phi_{\text{int}}\setminus\{Y_1\}} e^{itG(\Theta_i,\Theta_1)L(||Y_i||)}\right]$$
$$= E_{\Phi_{\text{int}},P_1}\left[\prod_{Y_i\in\Phi_{\text{int}}\setminus\{Y_1\}} E_{\Theta_i,\Theta_1}\left[e^{itG(\Theta_i,\Theta_1)L(||Y_i||)}\right]\right]$$
$$\overset{(a)}{=} E_{P_1}\left[\exp\left(-2\pi\left(\frac{\lambda_{BN}}{M} + \frac{\lambda_{BN}}{2M}|\alpha|^{\frac{4}{\gamma}}\mathbb{E}[L(U_j)^{\frac{2}{\gamma}}]\right)\int_{p_1}^\infty (1 - E_{\Theta_i,\Theta_1}\left[e^{itG(\Theta_i,\Theta_1)L(v)}\right])v\,\mathrm{d}v\right)\right] \tag{D.10}$$

where (a) follows from the PGFL of the homogeneous PPP outside a disc of radius p_1.

D.8 Proof of Theorem 5.10

Similar to the single antenna receiver, the CCDF of SINR for the multi-antenna receiver can be evaluated as follows:

$$\bar{F}_{\text{SINR}}(x) = P\left[\text{SINR} > x\right] = P\left[\frac{|\alpha|^2 G(\Theta_0,\Theta_1)L(U_0)L(V_0)}{I + \text{SNR}^{-1}} > x\right]$$
$$= P\left[I < \frac{|\alpha|^2 G(\Theta_0,\Theta_1)L(U_0)L(V_0)}{x} - \text{SNR}^{-1}\right]$$

$$= E_{U_0,V_0,\Theta_0,\Theta_1}\left[P\left[I < \frac{|\alpha|^2 G(\theta_0,\theta_1)L(u_0)L(v_0)}{x} - \mathrm{SNR}^{-1} | U_0 = u_0, V_0 = v_0, \Theta_0 = \theta_0, \Theta_1 = \theta_1\right]\right]$$

$$= \int_{-\pi}^{\pi}\int_{-\pi}^{\pi}\int_{0}^{\infty}\int_{0}^{\infty} F_I\left(\frac{|\alpha|^2 G(\theta_0,\theta_1)L(u_0)L(v_0)}{x} - \mathrm{SNR}^{-1}\right) f_{U_0,V_0}(u_0,v_0) f_{\Theta_0,\Theta_1}(\theta_0,\theta_1)\,\mathrm{d}u_0\,\mathrm{d}v_0\,\mathrm{d}\theta_0\,\mathrm{d}\theta_1,$$

where $I = \sum_{Y_i \in \Phi_{\mathrm{int}} \setminus \{Y_1\}} G(\Theta_i, \Theta_1) L(||Y_i||)$ is the interference at the multi-antenna receiver. The average BER given in the result is obtained by substituting the individual components in (D.8) and simplifying further.

D.9 Estimation of phase offset of the direct link

The phase offset of the direct ambient RF link at the receiver can be approximated in slow fading channel using the following approach. The received signal when a stream of bits valued 0 are transmitted in a preamble sequence is given by:

$$\mathbf{y}[n] = \begin{bmatrix} y_0[n] \\ y_1[n] \end{bmatrix} = h_r \begin{bmatrix} 1 \\ e^{j\phi_1} \end{bmatrix} x[n] + \begin{bmatrix} w_0[n] \\ w_1[n] \end{bmatrix},$$

Taking cross-product of the signals at the two antenna elements, we get the following result:

$$y_0[n] y_1^*[n] = |h_r|^2 e^{-j\phi_1} |x[n]|^2 + h_r x[n] w_1^*[n] + h_r^* x^*[n] w_0[n] + w_0[n] w_1^*[n]$$

Taking summation of this over a sample length N will result as follows:

$$\begin{aligned}\sum y_0[n] y_1^*[n] &= |h_r|^2 e^{-j\phi_1} \sum |x[n]|^2 + h_r \sum x[n] w_1^*[n] + h_r^* \sum x^*[n] w_0[n] + \sum w_0[n] w_1^*[n] \\ &= |h_r|^2 e^{-j\phi_1} N\bar{E} + h_r \sum x[n] w_1^*[n] + h_r^* \sum x^*[n] w_0[n] + \sum w_0[n] w_1^*[n]\end{aligned}$$

Taking expectation over the above signal will result in the following equation:

$$\begin{aligned}\mathbb{E}\left[\sum y_0[n] y_1^*[n]\right] &= \mathbb{E}\left[|h_r|^2 e^{-j\phi_1} N\bar{E}\right] + h_r \mathbb{E}\left[\sum x[n] w_1^*[n]\right] \\ &\quad + h_r^* \mathbb{E}\left[\sum x^*[n] w_0[n]\right] + \mathbb{E}\left[\sum w_0[n] w_1^*[n]\right] \\ &= N\bar{E}\mathbb{E}\left[|h_r|^2\right] e^{-j\phi_1} \implies e^{-j\phi_1} = \frac{\mathbb{E}\left[\sum y_0[n] y_1^*[n]\right]}{N\bar{E}\sigma_h^2}\end{aligned}$$

Bibliography

[1] G. Wang, F. Gao, R. Fan, and C. Tellambura, "Ambient backscatter communication systems: Detection and performance analysis," *IEEE Trans. Commun.*, vol. 64, no. 11, pp. 4836 – 4846, Nov. 2016.

[2] V. Liu, A. Parks, V. Talla, S. Gollakota, D. Wetherall, and J. R. Smith, "Ambient backscatter: Wireless communication out of thin air," *Proc., ACM SIGCOMM*, Aug. 2013.

[3] B. Kellogg, V. Talla, S. Gollakota, and J. R. Smith, "Passive Wi-Fi: Bringing low power to Wi-Fi transmissions," *Symposium on NSDI*, vol. 16, pp. 151–164, Mar. 2016.

[4] P. V. Nikitin, K. V. S. Rao, S. F. Lam, V. Pillai, R. Martinez, and H. Heinrich, "Power reflection coefficient analysis for complex impedances in RFID tag design," *IEEE Trans. Microw. Theory and Tech.*, vol. 53, no. 9, Sep. 2005.

[5] K. Kurokawa, "Power waves and the scattering matrix," *IEEE Trans. Microw. Theory and Tech.*, vol. MTT-13, no. 3, Mar. 1965.

[6] F. Fuschini, C. Piersanti, F. Paolazzi, and G. Falciasecca, "Analytical approach to the backscattering from UHF RFID transponder," *IEEE Antennas and Wireless Propagation Letters*, vol. 7, pp. 33–35, 2008.

[7] C. A. Balanis, "Antenna theory: analysis and design, john wiley & sons," *New York*, 1997.

[8] A. Bletsas, A. G. Dimitriou, and J. N. Sahalos, "Improving backscatter radio tag efficiency," *IEEE Trans. Microwave Theory Tech*, vol. 58, no. 6, pp. 1502–1509, 2010.

[9] A. Varshney, O. Harms, C. Perez-Penichet, C. Rohner, F. Hermans, and T. Voigt, "Lorea: A backscatter architecture that achieves a long communication range," *Proc., ACM on Embedded Network Sensor Systems (SenSys 17)*, no. 50, Nov. 2017.

[10] V. Talla, M. Hessar, B. Kellogg, A. Najafi, J. R. Smith, and S. Gollakota, "Lora backscatter: Enabling the vision of ubiquitous connectivity," *Proc., ACM on Interactive, Mobile, Wearable and Ubiquitous Technologies*, pp. 1–24, Sep. 2017.

[11] M. U. Sheikh, R. Duan, and R. Jantti, "Validation of backscatter link budget simulations with measurements at 915 mhz and 2.4 ghz," in *2019 IEEE 89th Vehicular Technology Conference (VTC2019-Spring)*. IEEE, 2019, pp. 1–5.

[12] K. Lu, G. Wang, F. Qu, and Z. Zhong, "Signal detection and BER analysis for RF-powered devices utilizing ambient backscatter," *Proc., Intl. Conf. on Wireless Commun. & Sig. Proc. (WCSP)*, Oct. 2015.

[13] G. Wang, F. Gao, Z. Dou, and C. Tellambura, "Uplink detection and BER analysis for ambient backscatter communication systems," *Proc., IEEE Globecom*, Dec. 2015.

[14] J. Qian, F. Gao, G. Wang, S. Jin, and H. Zhu, "Semi-coherent detection and performance analysis for ambient backscatter system," *IEEE Trans. Commun.*, vol. 65, no. 12, pp. 5266–5279, Dec. 2017.

[15] ——, "Noncoherent detections for ambient backscatter system," *IEEE Trans. Wireless Commun.*, vol. 16, no. 3, pp. 1412–1422, Mar. 2017.

[16] Y. Liu, Z. Zhong, G. Wang, and D. Hu, "Uplink detection and BER performance for wireless communication systems with ambient backscatter and multiple receiving antennas," *Proc., Intl. Conf. on Commun. and Networking in China (ChinaCom)*, pp. 79 – 84, Aug. 2015.

[17] Y. Liu, G. Wang, Z. Dou, and Z. Zhong, "New Coding and Detection Schemes for Ambient Backscatter Communication Systems," *IEEE Access*, Mar. 2017.

[18] T. Zeng, G. Wang, Y. Wang, Z. Zhong, and C. Tellambura, "Statistical Covariance Based Signal Detection for Ambient Backscatter Communication Systems," *Proc., IEEE Veh. Technology Conf. (VTC)*, Sep. 2016.

[19] G. Yang, Y.-C. Liang, R. Zhang, and Y. Pei, "Modulation in the air: Backscatter communication over ambient OFDM carrier," *IEEE Trans. Commun.*, vol. 66, no. 3, Mar. 2018.

[20] J. K. Devineni and H. S. Dhillon, "Ambient backscatter systems: Exact average bit error rate under fading channels," *IEEE Trans. Green Commun. and Networking*, vol. 3, no. 1, pp. 11–25, Mar. 2019.

[21] A. N. Parks, A. Liu, S. Gollakota, and J. R. Smith, "Turbocharging ambient backscatter communication," *ACM SIGCOMM Computer Communication Review*, vol. 44, no. 4, pp. 619–630, 2015.

[22] D. Bharadia, K. R. Joshi, M. Kotaru, and S. Katti, "Backfi: High throughput wifi backscatter," *ACM SIGCOMM Computer Communication Review*, vol. 45, no. 4, pp. 283–296, 2015.

[23] G. Yang, Y.-C. Liang, R. Zhang, and Y. Pei, "Modulation in the air: Backscatter communication over ambient ofdm carrier," *IEEE Trans. Commun.*, vol. 66, no. 3, pp. 1219–1233, 2017.

[24] G. Yang, Q. Zhang, and Y.-C. Liang, "Cooperative ambient backscatter communications for green internet-of-things," *IEEE Internet of Things Journal*, vol. 5, no. 2, pp. 1116–1130, 2018.

[25] J. K. Devineni and H. S. Dhillon, "Non-coherent detection and bit error rate for an ambient backscatter link in time-selective fading," *IEEE Trans. Commun.*, vol. 69, no. 1, pp. 602–618, Jan. 2021.

[26] ——, "Manchester encoding for non-coherent detection of ambient backscatter in time-selective fading," *IEEE Trans. on Veh. Technology*, 2021.

[27] V. Iyer, V. Talla, B. Kellogg, S. Gollakota, and J. R. Smith, "Inter-technology backscatter: towards internet connectivity for implanted devices," *Proc., ACM SIGCOMM*, pp. 1–14, Aug. 2016.

[28] P. Zhang, M. Rostami, P. Hu, and D. Ganesan, "Enabling practical backscatter communication for on-body sensors," in *Proc., ACM SIGCOMM*. ACM, 2016, pp. 370–383.

[29] A. Wang, V. Iyer, V. Talla, J. R. Smith, and S. Gollakota, "FM backscatter: Enabling connected cities and smart fabrics," in *Symposium on Networked Systems Design and Implementation (NSDI 17)*, 2017, pp. 243–258.

[30] K. Han and K. Huang, "Wirelessly powered backscatter communication networks: Modeling, coverage, and capacity," *IEEE Trans. Wireless Commun.*, vol. 16, no. 4, pp. 2548–2561, 2017.

[31] C. Psomas and I. Krikidis, "Collision avoidance in wireless powered sensor networks with backscatter communications," in *Proc., Intl. Workshop on SPAWC*. IEEE, 2017, pp. 1–5.

[32] M. Bacha and B. Clerckx, "Backscatter communications for the internet of things: A stochastic geometry approach," *arXiv preprint arXiv:1711.07277*, 2017.

[33] X. Lu, H. Jiang, D. Niyato, D. I. Kim, and Z. Han, "Wireless-powered device-to-device communications with ambient backscattering: Performance modeling and analysis," *IEEE Trans. Wireless Commun.*, vol. 17, no. 3, pp. 1528–1544, 2017.

[34] L. Xu, K. Zhu, R. Wang, and S. Gong, "Performance analysis of ambient backscatter communications in RF-powered cognitive radio networks," in *Proc., IEEE Wireless Commun. and Networking Conf. (WCNC)*. IEEE, 2018, pp. 1–6.

[35] D. Han and H. Minn, "Coverage probability analysis under clustered ambient backscatter nodes," *IEEE Wireless Commun. Letters*, vol. 8, no. 6, pp. 1713–1717, 2019.

[36] A. Hayajneh, S. A. R. Zaidi, M. Hafeez, D. McLernon, and M. Win, "Coverage analysis of drone-assisted backscatter communication for IoT sensor network," in *2019 15th Intl. Conf. on Distributed Computing in Sensor Systems (DCOSS)*. IEEE, 2019, pp. 584–590.

[37] X. Lu, D. Niyato, H. Jiang, E. Hossain, and P. Wang, "Ambient backscatter-assisted wireless-powered relaying," *IEEE Trans. on Green Commun. and Networking*, vol. 3, no. 4, pp. 1087–1105, 2019.

[38] L. Shi, R. Q. Hu, Y. Ye, and H. Zhang, "Modeling and performance analysis for ambient backscattering underlaying cellular networks," *IEEE Trans. on Veh. Technology*, vol. 69, no. 6, pp. 6563–6577, 2020.

[39] J. Guo, X. Zhou, S. Durrani, and H. Yanikomeroglu, "Design of non-orthogonal multiple access enhanced backscatter communication," *IEEE Trans. on Wireless Commun.*, vol. 17, no. 10, pp. 6837–6852, 2018.

[40] S. A. R. Zaidi, M. Hafeez, D. McLernon, and M. Z. Win, "Coverage analysis for backscatter communication empowered cellular internet-of-things," in *Proc., European Signal Processing Conf.* IEEE, 2019, pp. 1–5.

[41] Q. Yang, H.-M. Wang, T.-X. Zheng, Z. Han, and M. H. Lee, "Wireless powered asynchronous backscatter networks with sporadic short packets: Performance analysis and optimization," *IEEE Internet of Things Journal*, vol. 5, no. 2, pp. 984–997, 2018.

[42] H. Stockman, "Communication by means of reflected power," *Proc., of the IRE*, pp. 1196–1204, Oct. 1948.

[43] J. D. Griffin and G. D. Durgin, "Complete link budgets for backscatter radio and RFID systems," *IEEE Trans. Antennas and Propagation Mag.*, vol. 51, no. 2, pp. 11–25, Apr. 2009.

[44] D. Kim, M. A. Ingram, and W. W. S. Jr., "Measurements of small-scale fading and path loss for long range RF tags," *IEEE Trans. Antennas and Propagation*, vol. 51, no. 8, pp. 1740–1749, Aug. 2003.

[45] J. Kimionis, A. Bletsas, and J. N. Sahalos, "Increased range bistatic scatter radio," *IEEE Trans. Commun.*, vol. 62, no. 3, pp. 1091–1104, Mar. 2014.

[46] C. Boyer and S. Roy, "Backscatter communication and RFID: coding, energy and MIMO analysis," *IEEE Trans. Commun.*, vol. 62, no. 3, pp. 770–785, Mar. 2014.

[47] J. D. Griffin and G. D. Durgin, "Gains for RF tags using multiple antennas," *IEEE Trans. Antennas and Propagation*, vol. 56, no. 2, pp. 563–570, Feb. 2008.

[48] ——, "Multipath fading measurement at 5.8 GHz for backscatter tags with multiple antennas," *IEEE Trans. Antennas and Propagation*, vol. 58, no. 11, pp. 3694–3700, Nov. 2010.

[49] G. Vannucci, A. Bletsas, and D. Leigh, "A software-defined radio system for backscatter sensor networks," *IEEE Trans. Wireless Commun.*, vol. 2, no. 6, pp. 2170–2179, Jun. 2008.

[50] J. Hermans, R. Peeters, and B. Preneel, "Proper RFID privacy: model and protocols," *IEEE Trans. Mobile Computing*, vol. 13, no. 12, pp. 2888–2902, Dec. 2014.

[51] W. Saad, X. Zhou, Z. Han, and H. V. Poor, "On the physical layer security of backscatter wireless systems," *IEEE Trans. Wireless Commun.*, vol. 13, no. 6, pp. 3442–3451, Jun. 2014.

[52] A. N. Parks, A. Liu, S. Gollakota, and J. R. Smith, "Turbocharging ambient backscatter communication," *Proc., ACM SIGCOMM*, pp. 1–12, Aug. 2014.

[53] B. Kellogg, A. Parks, S. Gollakota, J. R. Smith, and D. Wetherall, "Wi-Fi backscatter: Internet connectivity for RF-powered devices," *Proc., ACM SIGCOMM*, pp. 1–12, Aug. 2014.

[54] V. Liu, V. Talla, and S. Gollakota, "Enabling instantaneous feedback with full-duplex backscatter," *Proc., ACM MobiCom*, no. 1-12, Sep. 2014.

[55] D. Darsena, G. Gelli, and F. Verde, "Modeling and Performance Analysis of Wireless Networks With Ambient Backscatter Devices," *IEEE Trans. Commun.*, vol. 65, no. 4, Apr. 2017.

[56] K. Han and K. Huang, "Wirelessly powered backscatter communication networks: Modeling, coverage, and capacity," *IEEE Trans. Wireless Commun.*, pp. 2548 – 2561, Mar. 2017.

[57] R. T. Short, "Computation of Rice and Noncentral Chi-Squared probabilities," *Phase-Locked Systems, Technical Report PHS0254*, vol. 16, no. 4, Apr. 2012.

[58] F. Ling and J. Proakis, *Synchronization in Digital Communication Systems*. Cambridge University Press, 2017. [Online]. Available: https://books.google.com/books?id=NNklDwAAQBAJ

[59] D. A. Shnidman, "The calculation of the probability of detection and the Generalized Marcum Q-function," *IEEE Trans. Info. Theory*, vol. 35, no. 2, Mar. 1989.

[60] A. N. Parks, A. Liu, S. Gollakota, and J. R. Smith, "Turbocharging ambient backscatter communication," *ACM SIGCOMM Computer Communication Review*, vol. 44, no. 4, pp. 619–630, 2014.

[61] H. S. Dhillon, H. Huang, and H. Viswanathan, "Wide-area wireless communication challenges for the internet of things," *IEEE Commun. Mag.*, vol. 55, no. 2, pp. 168–174, Feb. 2017.

[62] M. A. El Mossallamy, M. Pan, R. Jäntti, K. G. Seddik, G. Y. Li, and Z. Han, "Noncoherent backscatter communications over ambient OFDM signals," *IEEE Trans. Commun.*, vol. 67, no. 5, pp. 3597 – 3611, May 2019.

[63] Q. Tao, C. Zhong, H. Lin, and Z. Zhang, "Symbol detection of ambient backscatter systems with manchester coding," *IEEE Trans. Wireless Commun.*, vol. 17, no. 6, pp. 4028–4038, 2018.

[64] W. Zhao, G. Wang, S. Atapattu, and B. Ai, "Blind channel estimation in ambient backscatter communication systems with multiple-antenna reader," *Proc., IEEE/CIC ICCC*, pp. 320–324, Aug. 2018.

[65] H. Guo, Q. Zhang, D. Li, and Y.-C. Liang, "Noncoherent multiantenna receivers for cognitive backscatter system with multiple RF sources," *arXiv preprint, arXiv:1808.04316*, 2018.

[66] Q. Zhang, H. Guo, Y.-C. Liang, and X. Yuan, "Constellation learning-based signal detection for ambient backscatter communication systems," *IEEE J. Sel. Areas Commun.*, vol. 37, no. 2, pp. 452–463, 2018.

[67] H. Guo, Q. Zhang, S. Xiao, and Y.-C. Liang, "Exploiting multiple antennas for cognitive ambient backscatter communication," *IEEE Internet of Things Journal*, vol. 6, no. 1, pp. 765–775, 2018.

[68] D. Darsena, G. Gelli, and F. Verde, "Joint channel estimation, interference cancellation, and data detection for ambient backscatter communications," in *2018 IEEE 19th Intl. Workshop on SPAWC*, 2018, pp. 1–5.

[69] R. Duan, E. Menta, H. Yiğitler, and R. Jäntti, "Hybrid beamformer design for high dynamic range ambient backscatter receivers," *arXiv preprint, arXiv:1901.05323*, 2019.

[70] G. Raleigh, S. N. Diggavi, A. F. Naguib, and A. Paulraj, "Characterization of fast fading vector channels for multi-antenna communication systems," in *Proc. of 1994 28th Asilomar Conf. on Signals, Systems and Computers*, vol. 2. IEEE, 1994, pp. 853–857.

[71] A. M. Sayeed, "Deconstructing multiantenna fading channels," *IEEE Trans. Signal Processing*, vol. 50, no. 10, pp. 2563–2579, 2002.

[72] H. S. Dhillon and G. Caire, "Wireless backhaul networks: Capacity bound, scalability analysis and design guidelines," *IEEE Trans. Wireless Commun.*, vol. 14, no. 11, pp. 6043–6056, 2015.

[73] A. Adhikary, J. Nam, J.-Y. Ahn, and G. Caire, "Joint spatial division and multiplexing-the large-scale array regime," *IEEE Trans. Information Theory*, vol. 59, no. 10, pp. 6441–6463, 2013.

[74] A. Adhikary, E. Al Safadi, M. K. Samimi, R. Wang, G. Caire, T. S. Rappaport, and A. F. Molisch, "Joint spatial division and multiplexing for mm-wave channels," *IEEE J. Sel. Areas Commun.*, vol. 32, no. 6, pp. 1239–1255, 2014.

[75] A. Adhikary, H. S. Dhillon, and G. Caire, "Massive-mimo meets hetnet: Interference coordination through spatial blanking," *IEEE J. Sel. Areas Commun.*, vol. 33, no. 6, pp. 1171–1186, 2015.

[76] G. Stüber, *Principles of Mobile Communication*. Springer International Publishing, 2017.

[77] K. E. Baddour and N. C. Beaulieu, "Autoregressive modeling for fading channel simulation," *IEEE Trans. Wireless Commun.*, vol. 4, no. 4, pp. 1650–1662, 2005.

[78] Z. Liu, X. Ma, and G. B. Giannakis, "Space-time coding and Kalman filtering for time-selective fading channels," *IEEE Trans. Commun.*, vol. 50, no. 2, pp. 183–186, 2002.

[79] C. Komninakis, C. Fragouli, A. H. Sayed, and R. D. Wesel, "Multi-input multi-output fading channel tracking and equalization using Kalman estimation," *IEEE Tran. on Signal Processing*, vol. 50, no. 5, pp. 1065–1076, 2002.

[80] S. Ghandour-Haidar, L. Ros, and J.-M. Brossier, "On the use of first-order autoregressive modeling for rayleigh flat fading channel estimation with Kalman filter," *Signal Processing*, vol. 92, no. 2, pp. 601–606, 2012.

[81] H. S. Wang and P.-C. Chang, "On verifying the first-order markovian assumption for a rayleigh fading channel model," *IEEE Trans. Vehicular Technology*, vol. 45, no. 2, pp. 353–357, 1996.

[82] D. Darsena, "Noncoherent detection for ambient backscatter communications over OFDM signals," *IEEE Access*, vol. 7, pp. 159 415–159 425, 2019.

[83] S. Guruacharya, X. Lu, and E. Hossain, "Optimal non-coherent detector for ambient backscatter communication system," *arXiv preprint, arXiv:1911.10105*, 2019.

[84] J. K. Devineni and H. S. Dhillon, "Non-coherent signal detection and bit error rate for an ambient backscatter link under fast fading," *Proc., IEEE Globecom*, Dec. 2019.

[85] D. Tse and P. Viswanath, "Fundamentals of wireless communication," *Cambridge University Press*, 2005.

[86] U. Mengali, *Synchronization techniques for digital receivers*. Springer Science & Business Media, 2013.

[87] K. Pahlavan and A. H. Levesque, *Wireless information networks*. John Wiley & Sons, 2005.

[88] M. ElMossallamy, Z. Han, M. Pan, R. Jantti, K. Seddik, and G. Y. Li, "Noncoherent frequency shift keying for ambient backscatter over OFDM signals," *Proc., IEEE ICC*, May 2019.

[89] W. Zhao, G. Wang, S. Atapattu, R. He, and Y.-C. Liang, "Channel estimation for ambient backscatter communication systems with massive-antenna reader," *IEEE Trans. on Veh. Tech.*, vol. 68, no. 8, pp. 8254–8258, Aug. 2019.

[90] Y. Nakagawa, T. Maeda, A. Uchiyama, and T. Higashino, "Design and evaluation of a frequency shift backscatter tag for context recognition," in *Adjunct Proc., of the 2021 Intl. Conf. on Distributed Computing and Networking*, 2021, pp. 157–162.

[91] J. K. Devineni and H. S. Dhillon, "Multi-antenna non-coherent detection of ambient backscatter under time-selective fading," *Proc., IEEE Globecom*, Dec. 2020.

[92] S. Amuru, H. S. Dhillon, and R. M. Buehrer, "On jamming against wireless networks," *IEEE transactions on wireless communications*, vol. 16, no. 1, pp. 412–428, 2016.

[93] M. Di Renzo and P. Guan, "A mathematical framework to the computation of the error probability of downlink mimo cellular networks by using stochastic geometry," *IEEE Transactions on Communications*, vol. 62, no. 8, pp. 2860–2879, 2014.

[94] H. S. Dhillon and J. G. Andrews, "Downlink rate distribution in heterogeneous cellular networks under generalized cell selection," *IEEE Wireless Commun. Letters*, vol. 3, no. 1, pp. 42–45, 2013.

[95] D. Torrieri, *Principles of spread-spectrum communication systems*. Springer, 2005, vol. 1.

[96] R. M. Buehrer, "Code division multiple access (cdma)," *Synthesis Lectures on Communications*, vol. 1, no. 1, pp. 1–192, 2006.

[97] S. Verdu *et al.*, *Multiuser detection*. Cambridge university press, 1998.

[98] M. Tuchler and A. C. Singer, "Turbo equalization: An overview," *IEEE Trans. on Information Theory*, vol. 57, no. 2, pp. 920–952, 2011.

[99] B. Pitakdumrongkija, H. Suzuki, S. Suyama, and K. Fukawa, "Coded single-sideband qpsk and its turbo detection for mobile communication systems," *IEEE Trans. on vehicular Technology*, vol. 57, no. 1, pp. 311–323, 2008.

[100] Y. Jiang, Z. Zhou, M. Nanri, G.-I. Ohta, and T. Sato, "Inter-signal interference cancellation filter for four-element single sideband modulation," in *2012 IEEE 75th Vehicular Technology Conf. (VTC Spring)*. IEEE, 2012, pp. 1–5.

[101] A. M. Mustafa, Q. N. Nguyen, T. Sato, and G.-I. Ohta, "Four single-sideband m-qam modulation using soft input soft output equalizer over ofdm," in *2018 28th International Telecommunication Networks and Applications Conf. (ITNAC)*. IEEE, 2018, pp. 1–6.

[102] M. Abramowitz and I. A. Stegun, "Handbook of mathematical functions," *Appl. Math. Ser. 55, National Bureau of Standards*, pp. 942–943, Jun. 1964.

[103] W. Zhao, G. Wang, S. Atapattu, C. Tellambura, and H. Guan, "Outage analysis of ambient backscatter communication systems," *IEEE Commun. Letters*, vol. 22, no. 8, pp. 1736–1739, 2018.

[104] R. G. Gallager, "Principles of digital communication," *Cambridge University Press*, Jan. 2008.

[105] A. Papoulis, "Probability random variables and stochastic processes," *McGraw-Hill, 1st ed., p. 201*, 1965.

[106] N. O'Donoughue and J. M. F. Moura, "On the product of independent complex Gaussians," *IEEE Trans. Signal Processing*, vol. 60, no. 3, Mar. 2012.

[107] W. W. Hager, "Updating the inverse of a matrix," *SIAM review*, vol. 31, no. 2, pp. 221–239, 1989.

[108] D. Middleton, *An introduction to statistical communication theory*. McGraw-Hill New York, 1960, vol. 960.